

SLAC-R-540
UC-414

**A Precision Measurement of
the Spin Structure Function $g_1(x, Q^2)$
for the Proton and Deuteron***

G. S. Mitchell

Stanford Linear Accelerator Center
Stanford University
Stanford, CA 94309

SLAC-Report-540

June 1999

Prepared for the Department of Energy
under contracts DE-AC03-76SF00515
and DE-AC02-76ER00881

Printed in the United States of America. Available from the National Technical Information Service, U.S. Department of Commerce, 5285 Port Royal Road, Springfield, VA 22161.

*Ph.D. thesis, University of Wisconsin-Madison.

Table of Contents

Abstract	iv
Acknowledgments	v
List of Figures	x
List of Tables	xiii
1 Introduction	1
2 Theory	5
2.1 The Parton Model	11
2.2 Q^2 Dependence	15
2.3 Sum Rules	19
3 Experiment	22
3.1 Beam	22
3.1.1 Beam Polarimetry	28
3.1.2 Beam Monitoring	32
3.2 Target	34
3.3 Spectrometers	41
3.3.1 Magnets	46

3.3.2	Shower Counters	46
3.3.3	Cerenkov Tanks	50
3.3.4	Hodoscopes	54
3.3.5	Calibration	56
3.4	Data Acquisition	57
4	Analysis	60
4.1	Data Summary Tapes	62
4.2	Run Selection	64
4.3	Event Cuts	64
4.4	Raw Asymmetries	69
4.5	Raw Asymmetries to A_{\parallel}	70
4.5.1	Beam Polarization	71
4.5.2	Target Polarization	78
4.5.3	Dilution Factor	81
4.5.4	Nuclear Corrections	84
4.6	A_{\parallel} Corrections	89
4.6.1	Electroweak Correction	89
4.6.2	Rate Dependence Corrections	90
4.6.3	Pion/Positron Contamination	90
4.6.4	Resolution Corrections	98
4.6.5	Radiative Corrections	98

4.7	A_{\parallel} and A_{\perp} Asymmetries	101
4.8	Systematic Errors	102
5	Results	105
5.1	The Structure Function $g_1(x, Q^2)$	105
5.2	Q^2 dependence	112
5.3	Measured Region Integrals	116
5.4	Extrapolation and Sum Rules	117
5.5	NLO fitting	121
5.5.1	Method	121
5.5.2	Results	124
5.6	Conclusion	129
 Appendices		
A	Tracking Code	131
B	Magnetic Measurements of Møller Magnet B0	134
C	Tables of Asymmetry Results	136
D	Systematic Error Breakdown	143
E	The E155 Collaboration	146
	Bibliography	148

Abstract

A PRECISION MEASUREMENT OF THE SPIN STRUCTURE FUNCTION $g_1(x, Q^2)$ FOR THE PROTON AND DEUTERON

Gregory S. Mitchell

Under the supervision of Prof. Richard Prepost

At the University of Wisconsin-Madison

A precision measurement of the spin structure function $g_1(x, Q^2)$ for both the proton and deuteron was made using deep inelastic scattering of the 48.35 GeV polarized electron beam at the Stanford Linear Accelerator Center. The kinematic range of the measurement was $0.014 < x < 0.9$ and $1 \text{ (GeV/c)}^2 < Q^2 < 40 \text{ (GeV/c)}^2$. Solid $^{15}\text{NH}_3$ and $^6\text{Li}^2\text{H}$ were used as target materials. The beam polarization of 0.81 ± 0.02 was measured using Møller polarimetry. The scattered electron events were accumulated in three magnetic spectrometers at fixed angles of 2.75° , 5.5° , and 10.5° . Data were obtained with the target polarization direction both parallel and transverse to the beam direction. Together with existing world data, the $g_1(x, Q^2)$ results were fit in a well-established next-to-leading order QCD formalism, and are consistent with the Bjorken sum rule.

Acknowledgments

Thanks to my advisor, Prof. Richard Prepost. He gave me a lot of freedom but always kept an eye on me. I am grateful for the opportunity to have worked on E154 and E155 under his guidance. And thanks to the rest of the UW group at SLAC, specifically Henry Band.

Many thanks to the E155 collaboration. In particular, thanks to my fellow thesis students and the inhabitants of Building 207. Terry Toole and Peter Bosted were often around the same odd hours as I was and were great to work with and learn from.

Special thanks to three people from whom I learned a lot in my several years at SLAC: Charlie Young, Lee Sorrell, and Dave Reyna.

On a personal level, thanks to my friends out here in California and at SLAC. Softball, soccer and bridge have provided me with some good excuses for breaks from working on analysis.

Lastly, thanks to my family—my sometime physicist brother, my scientist parents who taught me to think logically—and especially, for her interest, encouragement, and patience, to my wife, Cherie.

List of Figures

2.1	Lowest order Feynman diagram for deep inelastic scattering of a lepton from a nucleon.	7
2.2	The deuteron structure function F_2^d . The solid curve is the 15-parameter functional fit to the data used in this analysis for determining the structure function F_1 . The dashed curves indicate the total error in the fit. The data in each bin are scaled by the factors in parentheses for clarity. The data are from NMC [22], SLAC [32], and BCDMS [33]. The figure is from Ref. [22].	16
3.1	Depiction of polarized deep inelastic scattering. The short arrows indicate polarization of the beam and target.	23
3.2	Energy level diagrams for GaAs (left) and strained GaAs (right). Transitions are shown for left (σ^-) circularly polarized light incident on the crystal. The transitions indicated by solid arrows are driven by photons of energy just greater than the band gap energy.	24
3.3	A schematic of the A-line, showing the twelve dipole bend magnets. The A-line was upgraded for E154 and E155 to allow up to 50 GeV beam into ESA.	26
3.4	Pseudo-random algorithm for determining the beam polarization state.	27

3.5	Møller mask, with central hole for the unscattered beam and two openings for the Møller scattered electrons.	31
3.6	The E155 target assembly, cross-section view.	36
3.7	Energy levels of the proton-electron system in a magnetic field.	38
3.8	The E155 spectrometers.	42
3.9	The E155 spectrometers, side view.	43
3.10	Q^2 vs. x kinematic coverage of the three spectrometers.	44
3.11	The 10 blocks by 20 blocks shower counter arrangement for the 2.75° and 5.5° spectrometers. Each block had a 6.2 cm square face and a length of 75 cm.	49
3.12	FADC waveforms from the 2.75° spectrometer for a single spill in E155 run 1238. Electron events typically had FADC peak signal >30. In this spill there were three obvious coincidences between the tanks and hence three likely electron events.	53
3.13	Schematic of data acquisition.	58
4.1	Effect on the event sample of cuts in the 2.75° and 10.5° spectrometers. The plots are explained in the text.	68

4.2	Single arm Møller results over the history of the parallel data taking. Each point represents the averaged results from all single arm detectors from one day's measurements, with error bars corresponding to the statistical error. The dashed line represents a constant fit to the data of $P_b = 81.3\%$. The $\chi^2/d.o.f.$ of the fit is 23/19.	72
4.3	Møller peaks in the fine detector from run 2588.	73
4.4	The Møller energy scan for parallel running (runs 576-654). The expression on the plot is a fit of the polarization to a cosine dependence on the beam energy. Also included is a term with E^4 to account for synchrotron radiation losses. The result of the fit is a maximum polarization of $P_0=0.84$, with an offset of 50 MeV in the beam energy with respect to the A-line reference magnet flip-coil reading.	76
4.5	E155 target polarization vs. run number, parallel data. The larger values (near $\pm 75\%$) are proton runs, and the smaller values (near $\pm 20\%$) are deuteron runs.	80
4.6	E155 average dilution factor for proton and deuteron targets.	84
4.7	The e^+/e^- ratio in the three spectrometers.	91

4.8	E/p ratios for a pion definition and an electron definition for the 8th x bin in the 2.75° spectrometer. The solid curve is a fit to the shape of the pion E/p distribution normalized to the electron definition distribution in the range [0.2,0.4]. The dotted curve is a fit to the electron distribution by a combination of a double-Gaussian and the solid curve.	93
4.9	The hadron contamination by x bin for both electron and positron running.	95
4.10	Resolution corrections to the parallel asymmetry, by spectrometer.	99
4.11	Feynman diagrams for internal and external processes considered in radiative corrections.	100
4.12	Proton and deuteron A_{\parallel} for E155.	103
4.13	Proton and deuteron A_{\perp} for E155.	104
5.1	Results for g_1^p , g_1^d , g_1^n : E155 vs. other experiments. The data have all been evolved to $Q^2 = 5 \text{ GeV}^2$	107
5.2	Results for xg_1^p , xg_1^d , xg_1^n : E155 vs. other experiments. The data have all been evolved to $Q^2 = 5 \text{ GeV}^2$	108
5.3	g_1^p for E155 and other experiments vs. Q^2 . The dashed curves are the proton fit from Eq. 5.3. The points and curves have been multiplied by the factors in parentheses for clarity.	113
5.4	g_1^p/F_1^p for E155 vs. other experiments. The multiple points in each bin for E155 are for the separate spectrometers. The dashed curves are the proton fit from Eq. 5.3.	114

5.5	g_1^d/F_1^d for E155 vs. other experiments. The multiple points in each bin for E155 are for the separate spectrometers. The dashed curves are the deuteron fit from Eq. 5.3.	115
5.6	Low x E155 results compared to E154 NLO fit.	118
5.7	E155 Results for Γ_1^p and Γ_1^d compared to sum rules. Also shown is the E154 result for Γ_1^n . The data are at the common $Q^2 = 5 \text{ GeV}^2$, and the widths of the bands represent $\pm 1\sigma$ total errors on each value. The Bjorken sum rule is confirmed, while the Ellis-Jaffe sum rule is violated.	120
5.8	The polarized parton distributions corresponding to the fit parameters of Table 5.6.	126
5.9	Distribution of fit results for 800 fits with input data points scattered by statistical uncertainties. The RMS width of each distribution was used to determine the uncertainty on the central value for the given quantity.	129
A.1	Flowchart depicting the logic of the routine <code>trk_drv.f</code>	133
B.1	$\int B dl$ vs. current curve. Measured with the ‘Long long’ flip-coil resting on top of the center of the septum.	135

List of Tables

2.1	Kinematic definitions for deep inelastic scattering.	6
3.1	Larmor frequencies for nuclear species in a 5 T magnetic field.	39
4.1	Numbers of runs used in E155 analysis.	65
4.2	Beam cuts used for final analysis of E155. The spill monitor cuts are in ADC units, the foil array cuts are in mm.	69
4.3	Systematic error contributions to beam polarization for the single arm Møller system.	77
4.4	E155 polarized target insert history [86].	78
4.5	Packing fractions by E155 insert number.	83
4.6	Values for terms in the proton nuclear correction C_1	86
4.7	Values for terms in the deuteron nuclear corrections C_1 and C_2	88
4.8	Constraints on the parameters used in calculating pion contamination. . .	96
4.9	Constant values used for contamination asymmetries.	97
4.10	Approximate asymmetry systematic errors as relative uncertainties. . . .	102
5.1	Coefficients for proton and neutron functional fits to world data on the proton, neutron, and deuteron.	106
5.2	Bin edges for coarse world binning.	109
5.3	E155 proton results for g_1/F_1 and g_1	110

5.4	E155 deuteron results for g_1/F_1 and g_1	111
5.5	Unpolarized parton distributions from Ref. [39], known as GRV98. They are given at the input scale $Q_0^2=0.40$ GeV ²	122
5.6	Coefficients for polarized parton distribution fit to world data on $g_1(x, Q^2)$ for proton, neutron, and deuteron.	125
5.7	Contribution of each experiment to total χ^2 of the fit.	127
B.1	Integrated $B dl$ vs. magnet current, measured with the ‘Long long’ flip-coil.	135
C.1	E155 results for $A_{ }$, 2.75° spectrometer.	137
C.2	E155 results for $A_{ }$, 5.5° spectrometer.	138
C.3	E155 results for $A_{ }$, 10.5° spectrometer.	139
C.4	E155 results for A_{\perp} , 2.75° spectrometer.	140
C.5	E155 results for A_{\perp} , 5.5° spectrometer.	141
C.6	E155 results for A_{\perp} , 10.5° spectrometer.	142
D.1	Proton systematic error contributions. The column headings represent: P_b , beam polarization; P_t , target polarization; f , dilution factor; C_1 and C_2 , nuclear corrections; F_2 and R , unpolarized structure functions; and RC , radiative corrections.	144

D.2 Deuteron systematic error contributions. The column headings represent:

P_b , beam polarization; P_t , target polarization; f , dilution factor; C_1 and

C_2 , nuclear corrections; F_2 and R , unpolarized structure functions; and

RC , radiative corrections. 145

Chapter 1

Introduction

This thesis describes a measurement of the spin structure functions of the nucleons. This experiment was conducted by the E155 Collaboration at the Stanford Linear Accelerator Center (SLAC) in Stanford, California. The data were obtained in February, March, and April of 1997.

Centuries of study and experiment have led to today's picture of matter and its interactions, known as the Standard Model. In the Standard Model, nucleons are built of quarks and gluons that bind the quarks together. The details of this composition have been studied experimentally for several decades. Nucleons are fermions, which have spin, and the origin of the spin of the nucleon has been a subject of study for a number of experiments during the last twenty years. Quarks and gluons carry their own spin, and they also contribute to the spin of the nucleon through their motion within it. How these spins fit together within the Standard Model (or outside of it) is the subject of this research.

Experiment E155 is one of the many experiments in the history of the fixed target program in End Station A (ESA) at SLAC. SLAC was built in the 1960's to provide a high-energy, high-intensity electron beam for study of the internal structure of the nucleon. Electron-nucleon scattering experiments in ESA in the late 1960's [1, 2, 3, 4]

led to the discovery of scaling—the term used to describe a weak dependence of the scattering cross-section on momentum transfer, or energy scale. Scaling, predicted by Bjorken [5, 6], was interpreted as evidence for pointlike objects within the proton. These objects, called partons, are identified today with the quarks of the Standard Model. The 1990 Nobel Prize in physics was awarded for this experimental work.

E155 measured the spin structure of the nucleon using the SLAC polarized electron beam incident on a solid polarized nucleon target. This experiment was similar to recent experiments at SLAC (E142 [7], E143 [8], E154 [9, 10, 11]), and also experimental programs at CERN (EMC [12] and SMC [13, 14]) in Geneva, Switzerland, and DESY (HERMES [15, 16]) in Hamburg, Germany.

Via deep inelastic scattering of SLAC's 48.35 GeV highly polarized electron beam, E155 probed the internal structure of the nucleons. The E155 cryogenic target made use of two materials: ammonia ($^{15}\text{NH}_3$) as a proton target and lithium deuteride ($^6\text{Li}^2\text{H}$, hereafter referred to as ^6LiD) as an isoscalar deuteron target. One way that the internal spin structure of nucleons manifests itself experimentally is in the dependence of cross-sections for deep inelastic electron-nucleon scattering on the relative orientation of the electron and nucleon spins. All spin structure measurements exploit this difference in measuring an asymmetry in the cross-sections. In measuring an asymmetry between polarization states—where the asymmetry is the ratio of the difference of cross-sections to the sum of cross-sections—some common unpolarized factors such as detector acceptance and unpolarized structure functions will cancel out. The systematic uncertainties

in an asymmetry measurement are much more favorable than in the measurement of a small difference between two quantities.

The polarized structure functions were determined from measurement of the asymmetry in inclusive deep inelastic electron-nucleon scattering. This required the use of a polarized electron beam, a polarized nucleon target, and spectrometer systems to detect the scattered electrons. The events were collected to data tape and later analyzed to calculate asymmetries and the resulting spin structure functions.

The data from E155 provide a precise measurement of the spin structure functions $g_1(x, Q^2)$ for the proton and deuteron over a broad kinematic range. The kinematic region covered by the three spectrometers of E155 fills the gap between the previous lower beam energy electron experiments at SLAC and DESY and the higher beam energy muon experiments at CERN. Thus, with the results of E155, there is now a significant world data set on the spin structure functions $g_1(x, Q^2)$. Global fits to this data set in a well-established theoretical framework can be used to extract polarized parton distributions for the quarks and gluons that make up the nucleons. The measured Q^2 dependence of the parton distributions and structure functions can be compared to that predicted by evolution equations. The theory of perturbative quantum chromodynamics (pQCD) is tested to the extent that the parton distributions and evolution equations can consistently describe the spin structure function data.

The theoretical description of the experiment is given in Chapter 2. The electron beam, the target, the spectrometers, and the data acquisition system are described

in Chapter 3. The analysis of the data tapes to produce asymmetries is explained in Chapter 4. Finally, the asymmetries are used to calculate the spin structure functions, which are in turn compared to world data and used in fits to extract information about the spin content of the nucleon. These results are given in Chapter 5.

Chapter 2

Theory

Like any scattering process, the deep inelastic scattering of leptons by nucleons can be described by a differential cross-section. The nucleon contribution to the differential cross-section is given by a hadron tensor, which is written in terms of structure functions that have both symmetric and antisymmetric parts. The symmetric parts are those which are evident in unpolarized or spin-averaged experiments. The antisymmetric parts are only evident in polarized experiments, and are best measured by finding the asymmetry between cross-sections for different polarization states. By measuring the asymmetries A_{\parallel} and A_{\perp} (defined below) the structure functions $g_1(x, Q^2)$ and $g_2(x, Q^2)$ are measured.

The relevant kinematic variables of deep inelastic scattering are defined in Table 2.1. The structure functions are written as functions of the quantities x and Q^2 , which are determined experimentally by knowledge of the beam energy E_0 , and the energy E' and scattering angle θ of the scattered electrons. The Bjorken x variable is a dimensionless quantity. Quantities of mass (m, M), energy (E_0, E'), and momentum (p) or momentum squared (Q^2) will here be written in terms of units of energy, usually GeV, by taking the speed of light $c = 1$.

m	lepton rest mass
M	nucleon rest mass
$p_0 = (E_0, \vec{p}_0)$	four-momentum of incident lepton
$p = (E', \vec{p})$	four-momentum of scattered lepton
$P = (M, \vec{0})$	four-momentum of target nucleon
θ	scattering angle in laboratory frame
$q = p_0 - p$	four momentum transfer
$\nu = E_0 - E'$	energy of the virtual photon
$Q^2 = -q^2 = 4E_0E' \sin^2 \left(\frac{\theta}{2} \right)$	(invariant mass) ² of virtual photon
$x = \frac{Q^2}{2M\nu}$	Bjorken scaling variable
$W^2 = M^2 + Q^2 \left(\frac{1-x}{x} \right)$	missing mass

y	$= \nu/E_0$
z	$= xM/E_0$
ϵ	$= 1/[1 + 2(1 + \nu^2/Q^2) \tan^2(\theta/2)]$
γ^2	$= 4M^2x^2/Q^2$
D'	$= \frac{(1-\epsilon)(2-y)}{y[1+\epsilon R(x, Q^2)]}$
f_k	$= \frac{1}{F_1(x, Q^2)} \frac{1}{\nu} \frac{1-\epsilon}{1+\epsilon R(x, Q^2)}$

Table 2.1: Kinematic definitions for deep inelastic scattering.

Figure 2.1 shows the lowest order Born-level scattering process for lepton-nucleon scattering. The differential cross-section for this process is written as [17, 18]

$$\frac{d^2\sigma}{d\Omega dE'} = \frac{\alpha^2}{Q^4} \frac{E'}{E_0} L^{\mu\nu} W_{\mu\nu} \quad (2.1)$$

and can be interpreted as the probability per unit solid angle that a lepton with incident energy E_0 is scattered with energy between E' and $E' + dE'$. In this expression α is the

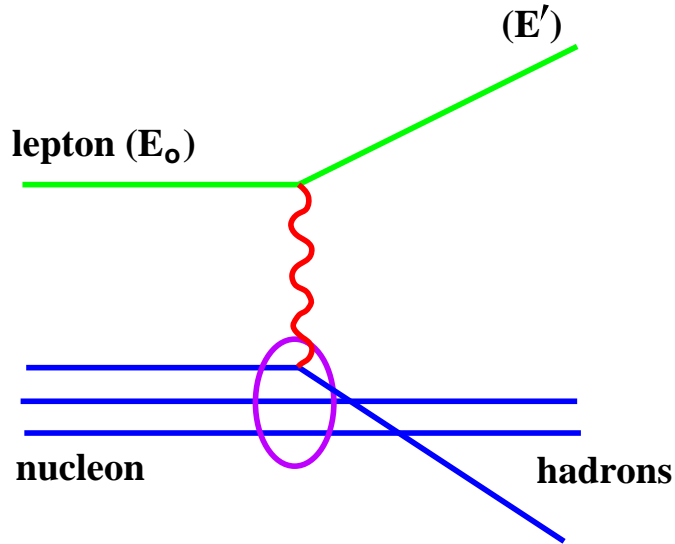


Figure 2.1: Lowest order Feynman diagram for deep inelastic scattering of a lepton from a nucleon.

electromagnetic coupling constant, and $L^{\mu\nu}$ is the simple and well understood factor for the upper lepton-photon vertex. The $W_{\mu\nu}$ factor represents the lower photon-nucleon vertex which is parameterized in terms of unpolarized symmetric structure functions F_1 and F_2 and polarized asymmetric structure functions g_1 and g_2 .

In the case of unpolarized scattering, the cross-section is written in terms of structure functions as

$$\frac{d^2\sigma}{d\Omega dE'} = \frac{4\alpha^2 E'^2 \cos^2(\theta/2)}{Q^4} \left[\frac{2F_1(x, Q^2)}{M} \tan^2(\theta/2) + \frac{F_2(x, Q^2)}{\nu} \right]. \quad (2.2)$$

The structure functions F_1 and F_2 are related by another function, R [19, 20, 21], in

$$F_1(x, Q^2) = F_2(x, Q^2) \frac{1 + \gamma^2}{2x [1 + R(x, Q^2)]}. \quad (2.3)$$

See Table 2.1 for a definition of γ^2 . The structure functions F_1 and F_2 have different values for the nucleons (proton, neutron, or deuteron), but within experimental limits, R is independent of nucleon type. The function R is the ratio of cross-sections for nucleon absorption of longitudinal and transverse virtual photons. In the analysis of this experiment, recent fits to world data on F_2 [22] and R [21] were used and F_1 calculated from those fits.

In the polarized case, the difference between cross-sections for anti-aligned versus aligned electron and nucleon spins is given by

$$\frac{d^2\sigma}{d\Omega dE'}^{\downarrow\uparrow} - \frac{d^2\sigma}{d\Omega dE'}^{\uparrow\uparrow} = \frac{4\alpha^2 E'}{Q^2 E_0 M \nu} \left[(E_0 + E' \cos \theta) g_1(x, Q^2) - 2xM g_2(x, Q^2) \right] \quad (2.4)$$

for the case of longitudinal polarization of the target, and by

$$\frac{d^2\sigma}{d\Omega dE'}^{\downarrow\leftarrow} - \frac{d^2\sigma}{d\Omega dE'}^{\uparrow\leftarrow} = \frac{4\alpha^2 E'}{Q^2 E_0 M \nu} \sin \theta \left[g_1(x, Q^2) + \frac{2E_0}{\nu} g_2(x, Q^2) \right] \quad (2.5)$$

for the case of transverse polarization of the target. The thin arrows (\uparrow) represent the electron helicity direction and the thick arrows ($\uparrow\uparrow$) represent the nucleon helicity direction. The notation $\sigma^{\downarrow\uparrow} = \frac{d^2\sigma}{d\Omega dE'}^{\downarrow\uparrow}$ (and similarly for the other cases) will be used below.

Equations 2.4 and 2.5 introduce the spin structure functions $g_1(x, Q^2)$ and $g_2(x, Q^2)$. Measuring these functions, in particular $g_1(x, Q^2)$, was the primary goal of E155. These functions differ for the various nucleons (proton, neutron, deuteron), but are related by:

$$g_1^d = \frac{1}{2}(g_1^p + g_1^n)(1 - 1.5\omega_D), \quad (2.6)$$

where p , n , d , refer to the nucleons. The deuteron, a bound state of a proton and a neutron, is considered here to be an ‘average’ nucleon. The factor $(1 - 1.5\omega_D)$ corrects for the D-state probability of the deuteron, $\omega_D = 0.05 \pm 0.01$. This probability is treated here as a constant with respect to Bjorken x . The deuteron magnetic moment $\mu_d = 0.857$ is close to the sum of the magnetic moments of the proton and neutron, $\mu_p + \mu_n = 2.793 - 1.913$. Thus the deuteron, a spin-1 entity, is mostly in a ground state where the orbital angular momentum of the proton and neutron is $L=0$, and the proton and neutron spins are aligned. Since the deuteron has a small quadrupole moment, there must be some mixture with another state. Of possible states for a spin-1 particle, the D state ($L=2$) is the only one which when mixed in a small amount with the S state can yield the observed magnetic moment. The factor of 1.5 in Eq. 2.6 arises from considering the Clebsch-Gordan coefficients for the probability in the D-state deuteron that the nucleon spins are aligned with the total deuteron spin [23].

Since in both cases on the left hand side of Eqs. 2.4 and 2.5 the cross-sections are nearly equal, to measure g_1 and g_2 by measuring the cross-sections and taking the differences would require extreme precision. Rather, the spin structure functions are obtained by measuring asymmetries, where common factors divide out.

Measuring cross-section asymmetries A_{\parallel} and A_{\perp} ,

$$A_{\parallel} = \frac{\sigma^{\downarrow\uparrow} - \sigma^{\uparrow\uparrow}}{\sigma^{\downarrow\uparrow} + \sigma^{\uparrow\uparrow}} \quad \text{and} \quad A_{\perp} = \frac{\sigma^{\downarrow\leftarrow} - \sigma^{\uparrow\leftarrow}}{\sigma^{\downarrow\leftarrow} + \sigma^{\uparrow\leftarrow}}, \quad (2.7)$$

yields the polarized structure functions via

$$g_1 = \frac{F_1}{D'} [A_{\parallel} + A_{\perp} \tan(\theta/2)] \quad (2.8)$$

and

$$g_2 = \frac{F_1}{D'} \frac{y}{2 \sin \theta} \left(-A_{\parallel} \sin \theta + A_{\perp} \frac{E_0 + E' \cos \theta}{E'} \right). \quad (2.9)$$

See Table 2.1 for definitions of kinematic variables D' and y . The quantities g_1 , g_2 , F_1 , A_{\parallel} , and A_{\perp} are all functions of x and Q^2 . The kinematic variables are all determined from E_0 and either (x, Q^2) or (E', θ) .

Due to the factor $\tan(\theta/2)$ in Eq. 2.8 which suppresses the contribution of A_{\perp} to g_1 for small θ , measuring A_{\parallel} at small scattering angles yields primarily information about g_1 . Similarly, the A_{\parallel} contribution to g_2 is suppressed by a factor of $\sin \theta$ relative to the contribution from A_{\perp} .

Another way to interpret the asymmetry in the scattering is to consider it in terms not of the incident lepton, but in terms of the virtual photon exchanged in the scattering. To leading order, the spin-1 photon can only couple to a spin-1/2 quark of opposite helicity. This is the source of the experimentally observable parallel asymmetry in electron-nucleon scattering. The cross-sections $\sigma_{1/2}^T$, $\sigma_{3/2}^T$, $\sigma_{1/2}^L$, and $\sigma_{1/2}^{TL}$ (all functions of x, Q^2) for virtual photon-nucleon scattering are related to the helicity amplitudes of the scattering process. The subscript 1/2 or 3/2 refers to the total spin of the photon-nucleon system in the direction of the path of the incident lepton. The superscript T refers to transverse polarization of the photon, L to longitudinal, and

TL to the cross-section arising from the interference of the transverse and longitudinal amplitudes. (The function R discussed above is defined as $R(x, Q^2) = \sigma_{1/2}^L/\sigma^T$, where $\sigma^T = \frac{1}{2} [\sigma_{1/2}^T + \sigma_{3/2}^T]$.)

Defining

$$A_1 = \frac{\sigma_{1/2}^T - \sigma_{3/2}^T}{\sigma_{1/2}^T + \sigma_{3/2}^T} \quad \text{and} \quad A_2 = \frac{\sigma_{1/2}^{TL}}{\frac{1}{2}(\sigma_{1/2}^T + \sigma_{3/2}^T)} \quad (2.10)$$

a series of relations for A_{\parallel} , A_{\perp} , A_1 , A_2 , g_1 , and g_2 can be written:

$$A_1 = \frac{1}{D'} [A_{\parallel}(1+z) - A_{\perp} \frac{z}{\tan(\theta/2)}], \quad (2.11)$$

$$A_2 = \frac{\gamma(2-y)}{2D'} [A_{\perp} \frac{y(1+z)}{(1-y)\sin\theta} + A_{\parallel}], \quad (2.12)$$

$$A_1 = (g_1 - \gamma^2 g_2)/F_1, \quad (2.13)$$

$$A_2 = \gamma(g_1 + g_2)/F_1, \quad (2.14)$$

$$A_{\parallel} = \frac{\sigma^{\downarrow\uparrow} - \sigma^{\uparrow\uparrow}}{\sigma^{\downarrow\uparrow} + \sigma^{\uparrow\uparrow}} = f_k [g_1(x, Q^2)[E_0 + E' \cos(\theta)] - \frac{Q^2}{\nu} g_2(x, Q^2)], \quad (2.15)$$

and

$$A_{\perp} = \frac{\sigma^{\downarrow\leftarrow} - \sigma^{\uparrow\leftarrow}}{\sigma^{\downarrow\leftarrow} + \sigma^{\uparrow\leftarrow}} = f_k E' \sin(\theta) [g_1(x, Q^2) + \frac{2E_0}{\nu} g_2(x, Q^2)], \quad (2.16)$$

with kinematic variables as defined above. For low x , where $\gamma \ll 1$, $A_1 \approx g_1/F_1$. Reviews of varying detail of the notation of polarized deep inelastic scattering can be found in Refs. [24, 8, 12, 18, 25, 26].

2.1 The Parton Model

In the parton model, the distribution of quarks (and gluons) inside the nucleon can be written in terms of probability distributions known as parton distributions, $q_i(x, Q^2)$.

The index i corresponds to quark and antiquark flavors. Each flavor has a charge e_i . These distributions are taken to be for the proton, and those for the neutron are given from the proton ones by isospin symmetry.

The distributions can be thought of as the sum of distributions for positive and negative helicity partons:

$$q_i(x, Q^2) = q_i^\uparrow(x, Q^2) + q_i^\downarrow(x, Q^2) \quad (2.17)$$

with the arrows denoting spin aligned or anti-aligned with the nucleon spin. The differences Δq_i between helicity distributions,

$$\Delta q_i(x, Q^2) = q_i^\uparrow(x, Q^2) - q_i^\downarrow(x, Q^2), \quad (2.18)$$

are the polarized parton distributions. The $q_i = G, u, d, s, \bar{u}, \bar{d}, \bar{s}$ represent the parton distributions for gluons, the three light quarks, and the three light antiquarks, respectively.

In the naive quark-parton model, where gluons and sea quarks and heavy flavors are neglected, F_1 is related to the spin averaged quark distribution functions:

$$F_1(x, Q^2) = \frac{1}{2} \sum_i e_i^2 [q_i^\uparrow(x, Q^2) + q_i^\downarrow(x, Q^2)] \quad (2.19)$$

where explicitly for the proton

$$F_1^p = \frac{1}{2} \left[\frac{4}{9} u + \frac{1}{9} d + \frac{1}{9} s \right]. \quad (2.20)$$

Similarly g_1 is related to the spin distribution functions:

$$g_1(x, Q^2) = \frac{1}{2} \sum_i e_i^2 \Delta q_i, \quad (2.21)$$

$$g_1^p = \frac{1}{2} \left[\frac{4}{9} \Delta u + \frac{1}{9} \Delta d + \frac{1}{9} \Delta s \right]. \quad (2.22)$$

In Eq. 2.20 and Eq. 2.22 the parton distributions and structure functions can be taken to have dependence on (x, Q^2) , or the equations can also be interpreted as the integral of the structure function and the integrals of the parton distributions over $x = [0, 1]$ at fixed Q^2 .

At large x , the struck quark is by definition carrying most of the momentum of the nucleon. If it is assumed that this quark is also carrying most of the spin of the nucleon, then the asymmetry A_1 would tend towards 1 with increasing x . However, the spin structure function g_1 will be small at large x since in the sense of parton distributions there are few quarks at high x and thus the difference between spin states of quarks cannot be large.

In a more refined (and more complicated) interpretation of nucleon structure, gluon and sea quark distributions also contribute to the structure functions. The naive parton model, however, does provide a simple illustration that measuring the unpolarized structure functions is a method of measuring the unpolarized parton distribution functions, and measuring the polarized spin structure functions is a method of determining the polarized parton distribution functions. Knowledge of the parton distribution functions (for quarks, sea quarks, and gluons) is in large part the ultimate goal of understanding the internal structure of the nucleon in the Standard Model.

The polarized parton distributions (integrated over $x = [0, 1]$ at fixed Q^2) can also

be written in terms of an SU(3) flavor basis:

$$\begin{aligned}
 \Delta q_0 &= \Delta u + \Delta d + \Delta s \\
 \Delta q_3 &= \Delta u - \Delta d \\
 \Delta q_8 &= \Delta u + \Delta d - 2\Delta s
 \end{aligned}
 \tag{2.23}$$

where the singlet distribution Δq_0 is often written $\Delta\Sigma$. These quantities are related to the F and D weak decay constants:

$$\begin{aligned}
 \Delta q_3 = F + D &= 1.2670 \pm 0.0035 \\
 \Delta q_8 = 3F - D &= 0.584 \pm 0.032
 \end{aligned}
 \tag{2.24}$$

where $F + D = g_A/g_V$ is determined from neutron beta decay, and $3F - D$ is determined from the ratio of the axial-vector and vector form factors in other baryon semileptonic beta decays. In the assumption that the SU(3) octet of spin-1/2 baryons including the proton and neutron undergoes beta decay via currents that also transform as an SU(3) octet, then the semileptonic beta decays can be described by just two constants F (symmetric) and D (antisymmetric) [18, 27, 28, 29]. The constants describe the coupling between two SU(3) octet representations (symmetric and antisymmetric, arising from the tensor product of the two octet representations for the initial and final state baryons) to form a third octet (that of the decay currents). The values given above were determined from Ref. [30] in Ref. [31].

2.2 Q^2 Dependence

In the naive parton model, the parton distributions and structure functions are simply functions of the Bjorken x variable, and not of Q^2 . This is known as scaling, since the quantities are independent of the energy scale of the interaction. However, QCD predicts that scaling, while approximately true, is violated. The violation is predicted to vary on a logarithmic scale in Q^2 .

With increasing Q^2 , the quarks in the nucleon are more likely to radiate gluons. These gluons can convert to quark-antiquark pairs. The virtual photon in deep inelastic scattering interacts with a quark in the nucleon, and if the quark has radiated a gluon it has a reduced momentum. Recalling that x is interpreted as the momentum fraction of the nucleon carried by the struck quark, this has the effect of moving the quark distribution to lower x . The partons at high x radiate gluons and move to low x , while new partons are formed at low x as products of this radiation. Therefore, with increasing Q^2 it is expected that the structure functions will decrease at high x and increase at low x . This was first seen in the unpolarized structure functions, as shown for F_2^d in Fig. 2.2 [22].

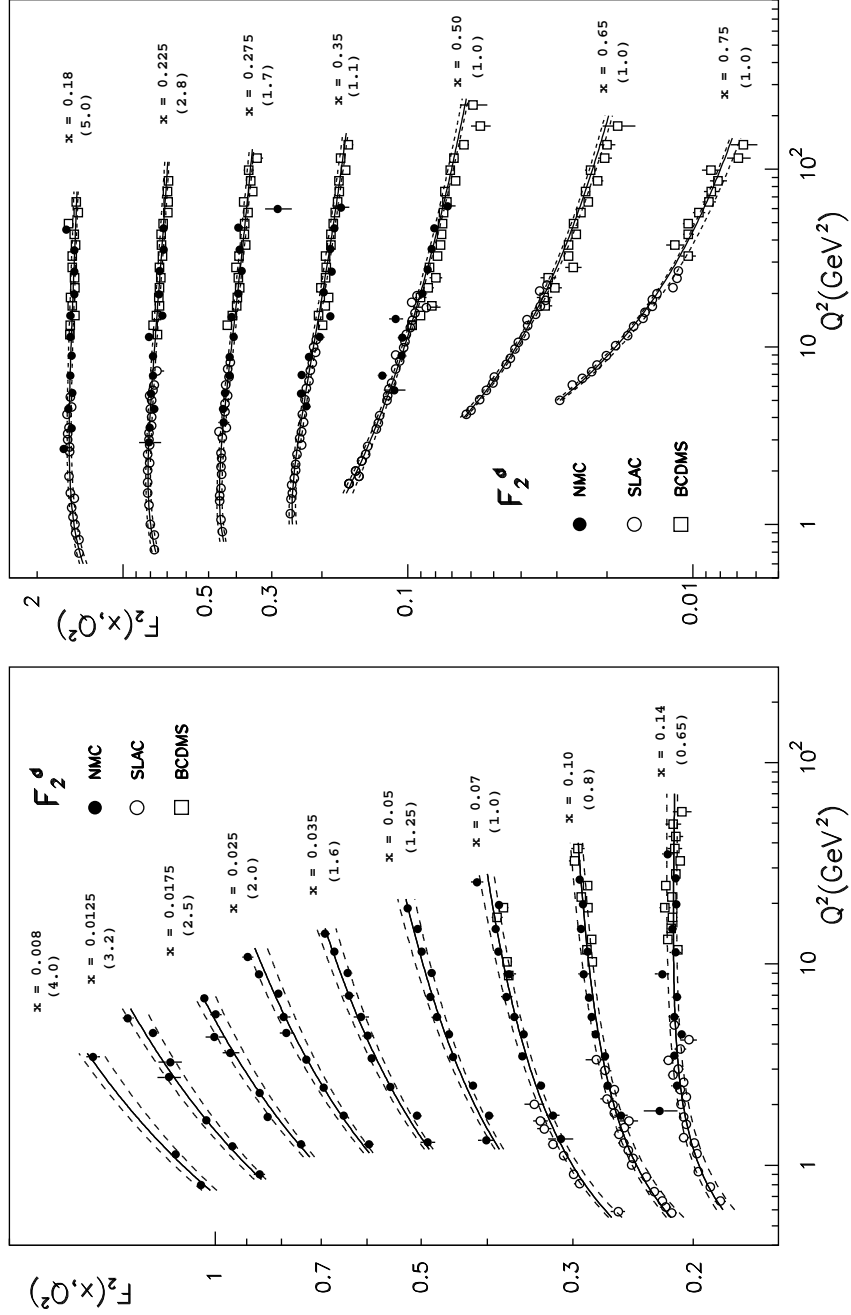


Figure 2.2: The deuteron structure function F_2^d . The solid curve is the 15-parameter functional fit to the data used in this analysis for determining the structure function F_1 . The dashed curves indicate the total error in the fit. The data in each bin are scaled by the factors in parentheses for clarity. The data are from NMC [22], SLAC [32], and BCDMS [33]. The figure is from Ref. [22].

The Q^2 dependence of the polarized parton distributions is given by the DGLAP equations¹ [34, 35, 36]

$$\frac{d\Delta q_i(x, Q^2)}{d \ln Q^2} = \frac{\alpha_S(Q^2)}{2\pi} [\Delta q_i \otimes \Delta P_{qq} + \Delta G \otimes \Delta P_{qG}] \quad (2.25)$$

and

$$\frac{d\Delta G(x, Q^2)}{d \ln Q^2} = \frac{\alpha_S(Q^2)}{2\pi} [\sum_i \Delta q_i \otimes \Delta P_{Gq} + \Delta G \otimes \Delta P_{GG}] \quad (2.26)$$

where Δq_i are the polarized quark and antiquark distributions and ΔG is the polarized gluon distribution, both with (x, Q^2) dependence. The strong coupling constant $\alpha_S(Q^2)$ describes interactions with gluons at energy scale Q^2 . The sum in the gluon equation is over quark and antiquark flavors. The convolution denoted by \otimes is

$$(f \otimes g)(x) = \int_x^1 \frac{dy}{y} f(y) g\left(\frac{x}{y}\right). \quad (2.27)$$

The splitting functions (denoted by ΔP for the polarized case and P for the unpolarized case) are calculated as a series in the strong coupling constant α_s and have been determined for the polarized case to next-to-leading order [37, 38]. In the unpolarized case, these functions are interpreted as the probability for finding a parton of the first index type (with some fraction of the parent parton's momentum) within a parton of the second index type. For example, $P_{qq}(x/y)$ gives the probability of a quark with momentum y emitting a gluon and thereby becoming a quark with momentum x . The splitting functions for the polarized parton distributions are similar to the unpolarized

¹The equations are so-called after five authors who derived them: Dokshitzer, Gribov, Lipatov, Altarelli, and Parisi.

ones but instead provide information about the evolution of the differences of the parton helicity states.

The evolution equations are used to determine the polarized parton distributions at a Q^2 larger than some initial input scale Q_0^2 . In Chapter 5 this input scale will be chosen to be $Q_0^2 = 0.40 \text{ GeV}^2$ to be consistent with an analysis of unpolarized parton distributions [39]. The evolution equations do not have exact analytic solutions, but they can be solved numerically.

Another source of Q^2 dependence is higher twist² contributions. These contributions to the scattering arise from processes which include more than the minimal number of fields, for example when the struck quark radiates a gluon which couples to one of the other quarks in the nucleon. These effects are believed to be small [41], since the Q^2 dependence of existing data is well described by DGLAP evolution.

As the Q^2 dependence of g_1 and F_1 is given by similar DGLAP equations ($\Delta P_{qq} = P_{qq}$ in leading order), their evolution with Q^2 is expected to be similar. By fitting the world data on g_1 using next-to-leading order (NLO) DGLAP equations, polarized distribution functions for quarks and gluons can be extracted. Even though the gluon distribution is not directly measured in deep inelastic scattering, it enters in the evolution equations for the Q^2 dependence of the structure functions, and thus it can be extracted from knowledge of that dependence. Such a NLO fit to E155 and world data is described in

²The term ‘twist’ arises from the notation of operator product expansion [40] and gives the relative contribution of a given term to deep inelastic scattering. Twist is defined as the difference between the dimension and the spin of an operator. The smallest possible twist in QCD is $t=2$.

Chapter 5.

2.3 Sum Rules

The quantities $\Delta\Sigma$ and ΔG give the spin contribution to the proton of quarks (which are spin-1/2 fermions) and gluons (spin-1 bosons) respectively. Also of interest, but currently not directly measurable, is the orbital angular momentum contribution from the quarks and gluons, written as L . The total spin of the nucleon, 1/2, can be written as the sum of these three parts:

$$S = \frac{1}{2} = \frac{1}{2}\Delta\Sigma + \Delta G + L. \quad (2.28)$$

In the naive quark-parton model $\Delta\Sigma=1$. Early experimental results from EMC [12] included a $\Delta\Sigma$ that was consistent with zero and that the strange quark sea was strongly negatively polarized. This was the origin of the so-called ‘proton spin crisis’ which was responsible for the significant amount of worldwide spin structure function experimental activity in the 1990’s.

Another motivation for much of the experimental work on spin structure functions has been a prediction for the difference between the integral of the proton and neutron spin structure functions. The Bjorken Sum Rule [42] was derived by J. D. Bjorken in 1966 from current algebra and isospin symmetry. In the limit $Q^2 = \infty$,

$$\int_0^1 [g_1^p(x) - g_1^n(x)] dx = \frac{1}{6} \frac{g_A}{g_V}, \quad (2.29)$$

where the ratio g_A/g_V , given in Eq. 2.24, is the ratio of nucleon axial-vector and vector weak couplings determined accurately from neutron β decay.

The QCD corrections for finite Q^2 have been derived to order three for $n_f = 3$ for the non-singlet case [43]

$$C_{ns} = \left[1 - \frac{\alpha_s(Q^2)}{\pi} - 3.5833 \left(\frac{\alpha_s(Q^2)}{\pi} \right)^2 - 20.2153 \left(\frac{\alpha_s(Q^2)}{\pi} \right)^3 \right] \quad (2.30)$$

such that the Bjorken sum rule becomes $\int_0^1 [g_1^p(x) - g_1^n(x)] dx = \frac{1}{6} \frac{g_A}{g_V} C_{ns}$.

Taking $\alpha_s(M_z^2) = 0.119 \pm 0.002$ [30], which yields $\alpha_s(5 \text{ GeV}^2) = 0.29 \pm 0.02$, gives:

$$\Gamma_1^p - \Gamma_1^n = \int_0^1 (g_1^p(x, 5 \text{ GeV}^2) - g_1^n(x, 5 \text{ GeV}^2)) dx = 0.182 \pm 0.005, \quad (2.31)$$

where Γ_1 is used to represent the integral over $[0,1]$ at a constant Q^2 .

The Bjorken sum rule is a robust theoretical prediction relying only on isospin symmetry. A test of the Bjorken sum rule is a test of QCD, and the sum rule is itself more fundamental than QCD. The sum rule relates the internal spin structure of the nucleons measured at high energy to the the lower-energy weak decay parameters.

Another well-known sum rule is the Ellis-Jaffe sum rule [44]. The Ellis-Jaffe sum rule also requires QCD corrections, both the above C_{ns} and a singlet correction C_s [45]:

$$C_s = \left[1 - \frac{\alpha_s(Q^2)}{\pi} - 1.0959 \left(\frac{\alpha_s(Q^2)}{\pi} \right)^2 \right]. \quad (2.32)$$

The Ellis-Jaffe sum rule is derived by expressing the spin structure integrals in the framework of the operator product expansion (OPE). OPE is used in QCD to parameterize nonperturbative quantities in terms of matrix elements. In leading twist, the integrals of the spin structure functions g_1 can be written as:

$$\Gamma_1^p(Q^2) = \left(\frac{1}{12} a_3 + \frac{1}{36} a_8 \right) C_{ns} + \frac{1}{9} a_0 C_s \quad (2.33)$$

$$\Gamma_1^n(Q^2) = \left(-\frac{1}{12}a_3 + \frac{1}{36}a_8\right) C_{ns} + \frac{1}{9}a_0C_s \quad (2.34)$$

$$\Gamma_1^d(Q^2) = \left(1 - \frac{3}{2}\omega_D\right) \left[\frac{1}{36}a_8C_{ns} + \frac{1}{9}a_0C_s\right] \quad (2.35)$$

with the matrix elements denoted by a_0 (singlet), and a_3 and a_8 (nonsinglet).

In the naive parton model, these matrix elements a are identical to the Δq_0 , Δq_3 , and Δq_8 of Eq. 2.24. The matrix elements then take the values $a_3 = F + D$ and $a_8 = 3F - D$. The matrix element a_0 is dependent on the choice of factorization scheme, but in the common $\overline{\text{MS}}$ scheme, $a_0 = \Delta\Sigma$. (Other schemes include a contribution of ΔG in addition to $\Delta\Sigma$.) The Ellis-Jaffe assumption of $\Delta s = \Delta G = 0$ results in $a_0 = a_8 = 3F - D$, yielding predictions for $\Delta\Sigma = a_0$, Γ_1^p , Γ_1^n , and Γ_1^d . According to present world data, the Ellis-Jaffe predictions for $\Gamma_1^p = 0.163 \pm 0.004$, $\Gamma_1^n = -0.019 \pm 0.004$, $\Gamma_1^d = 0.067 \pm 0.004$, and $\Delta\Sigma = 0.58 \pm 0.03$ are violated.

Alternately, a measurement of $g_1(x, Q^2)$ for the proton and/or deuteron, together with knowledge of F and D and the corrections C_{ns} and C_s , will yield $\Delta\Sigma$, the quark spin contribution to the nucleon.

Chapter 3

Experiment

In the months of February, March, and April 1997, the experiment E155 was performed in End Station A (ESA) at SLAC. Approximately 180 million deep inelastic scattering electron events were recorded to data tapes. During data-taking, the experimenters controlled and monitored the target and spectrometers from a building next to ESA, known as the counting house. The experiment was controlled remotely for reasons of radiation safety.

The experimental process of polarized deep inelastic scattering is depicted schematically in Fig. 3.1. The E155 parallel experimental asymmetry was of order 1×10^{-2} .

3.1 Beam

SLAC has the unique ability to provide an intense, high-energy, high-polarization electron beam. The beam is produced by shining circularly polarized laser light on a strained GaAs cathode [46, 47]. The cathode emits longitudinally polarized electrons, which are then accelerated in the two-mile linear accelerator (linac) to an energy of up to approximately 50 GeV.

Energy level diagrams of GaAs and strained GaAs are shown in Fig. 3.2. The shown transitions from the valence band and the spin-orbit split-off band to the conduction

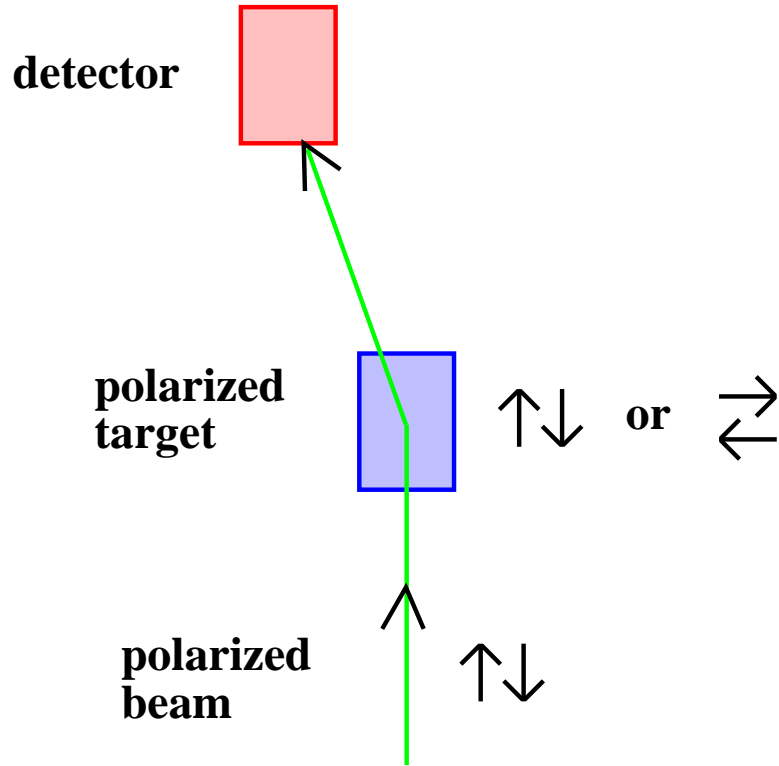


Figure 3.1: Depiction of polarized deep inelastic scattering. The short arrows indicate polarization of the beam and target.

band are for left (σ^-) circularly polarized light incident on the crystal. From the Clebsch-Gordan angular momentum addition coefficients for $3/2 \otimes 1$, the $m_j = +3/2 \rightarrow m_j = +1/2$ transition probability is three times the $m_j = +1/2 \rightarrow m_j = -1/2$ transition probability, so for a GaAs cathode crystal the maximum theoretical polarization is $(N_+ - N_-)/(N_+ + N_-) = (3 - 1)/(3 + 1) = +0.5$. The strained GaAs, which is GaAs grown on a $\text{GaAs}_{1-x}\text{P}_x$ sublayer, is subjected to a compressive strain by the 1% lattice spacing mismatch of the two layers and does not have the degeneracy in the $P_{3/2}$ level that is present in bulk GaAs. Due to the strain-induced $P_{3/2}$ band splitting (0.05 eV),

it is possible to produce polarizations $>50\%$ by illuminating the cathode with photons of energy greater than the band gap energy (1.43 eV) but less than the band gap energy plus the band splitting.

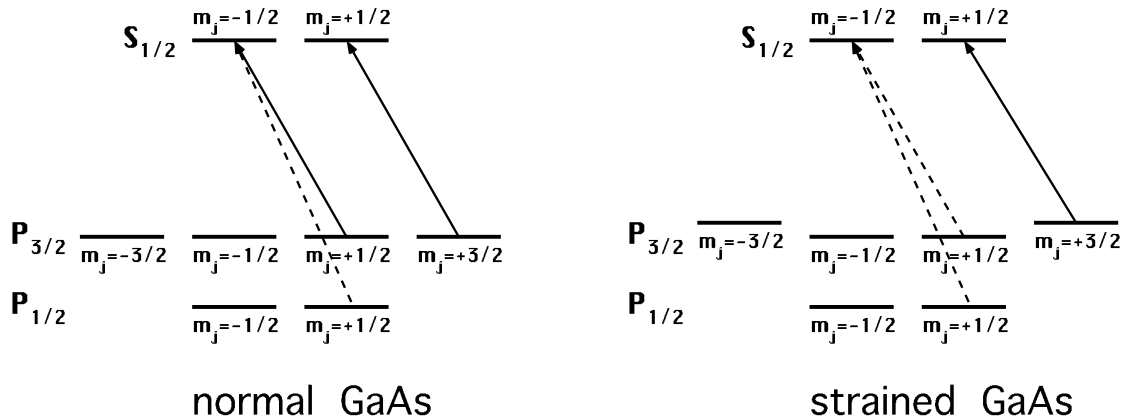


Figure 3.2: Energy level diagrams for GaAs (left) and strained GaAs (right). Transitions are shown for left (σ^-) circularly polarized light incident on the crystal. The transitions indicated by solid arrows are driven by photons of energy just greater than the band gap energy.

After the incident photons produce conduction band electrons in the GaAs, the electrons diffuse to the surface of the material. To induce the electrons in the conduction band to leave the cathode material, the GaAs is doped with a p-type material (Zn) and has a layer of Cs and an oxide applied to its surface. This produces a negative electron affinity surface, where the vacuum level is below the bottom of the lowest conduction band in the bulk crystal [47]. To maintain an acceptable quantum efficiency (QE), the SLAC cathodes often require cesiation. However, the cathode was not recesiated during E155 since the QE remained sufficiently high throughout the experiment. The QE fell

monotonically from 0.14% to 0.06% over the course of the experiment. The electron beam polarization is inversely related to the cathode QE [47], but over the QE range of E155 no dependence was observed.

As the electron beam reaches the end of the two-mile linac, it can be directed in the beam switchyard to the A-line, a series of twelve dipole magnets which steer the beam 24.50° to its left. A depiction of the A-line is given in Fig. 3.3. The A-line is the path the electron beam takes from the accelerator to ESA, where the E155 target and spectrometers were located. The energy of the beam into ESA was defined by the bend strength of the magnets and the momentum-defining slits SL-10, which were set for an energy spread of 0.80%. The A-line was upgraded in 1994 and 1995 to transport electrons of energies up to 50 GeV. Through the A-line bend at 50 GeV, an electron will lose ~ 400 MeV due to synchrotron radiation, a significant enough amount to merit consideration in the beamline design [48, 49]. Maintaining the longitudinal electron polarization through transport in the A-line bend required selecting a beam energy corresponding to a half-integral number of spin precessions. E155 ran at beam energies corresponding to precession of 15π for parallel target polarization data taking and of 12π for perpendicular mode.

The beam was provided to ESA in pulses, at a rate of 120 Hz. Each pulse was of duration ~ 400 ns. The current of the beam was typically $3.0 \times 10^9 e^-/\text{spill}$ for proton target running and $3.3 \times 10^9 e^-/\text{spill}$ for deuteron target running. For perpendicular target polarization the beam current was typically limited to $1.5 \times 10^9 e^-/\text{spill}$ by higher

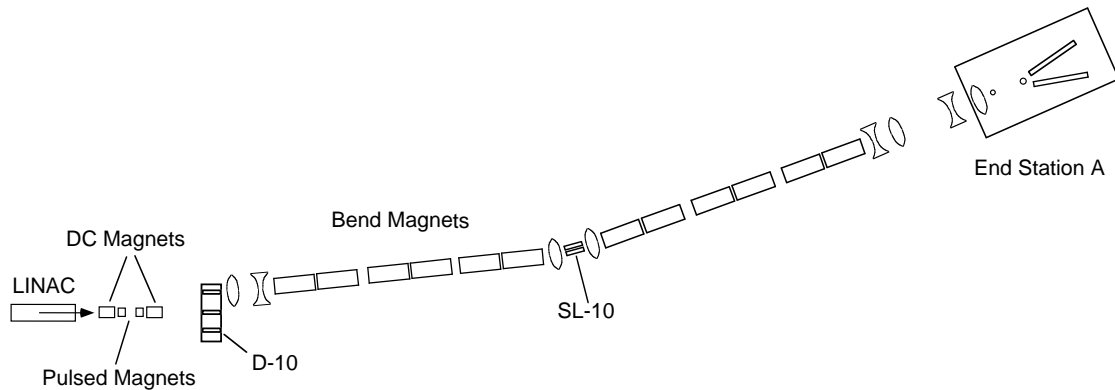


Figure 3.3: A schematic of the A-line, showing the twelve dipole bend magnets. The A-line was upgraded for E154 and E155 to allow up to 50 GeV beam into ESA.

backgrounds and data acquisition limitations.

The helicity of the beam was pseudo-randomly flipped from pulse to pulse, allowing the physics asymmetry measurement to be less sensitive to systematic errors. In principle the experiment could have been conducted with less frequent changes in beam/target polarization states, but then drifts in overall detector efficiency, acceptance and beam conditions would possibly have appeared as false asymmetries in the data. The polarization of a particular pulse was controlled by a Pockels cell, which by application of high voltage allowed only one circular polarization direction of laser light to pass on to the cathode. The pseudo-random selection of polarization state was given by the algorithm depicted in Fig. 3.4. The algorithm works as follows, once a 32-bit seed is chosen. The 32nd bit determines the polarization state. The 19th and 32nd bits are combined with an exclusive-or to determine a new bit, which is placed into the zeroth bit location. The bits are then shifted one location to the right, providing a new 32nd

bit and the polarization state for the next beam pulse, and the process is repeated.

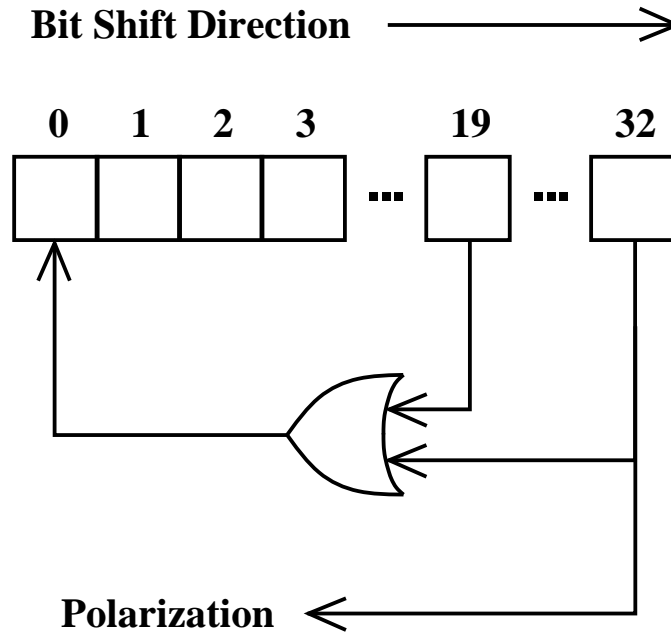


Figure 3.4: Pseudo-random algorithm for determining the beam polarization state.

The helicity state of each beam pulse was recorded as part of the beam data for the spill. Several sets of polarization bits [50] provided this information. They are known as: PMON; Pockels Cell High Voltage, or Scaler; MACH (Multi-Access Communication Highway) line; and Klystron Veto Module, or Veto. The PMON controller module is a CAMAC module at the polarized source which uses the algorithm of Fig. 3.4 to select the helicity state for the next spill, and it communicates this to the high voltage amplifier of the Pockels cell. The High Voltage polarization bits originated at the monitor output of the amplifier, and were used to gate ESA scalers. The MACH line and Veto bits were simply alternate paths for the PMON control signals to travel to

ESA. The timing of the Veto bits caused difficulties for E142 [51], but these problems are now well understood and not present for later ESA experiments. The helicity state of a beam pulse was given by an agreement between all four sets of polarization bits. The state could also be compared to the output of the pseudo-random algorithm once the states of 33 consecutive spills are known.

The beam was rastered over the target area in order to minimize the radiation damage to the material and beam heating effects, which both weaken the polarization. The beam was rastered on a grid of points spaced by 0.3 mm, over a circular pattern of diameter 24 mm.

3.1.1 Beam Polarimetry

The beam polarization was measured by using Møller polarimetry. There is an inherent asymmetry in electron-electron scattering [52] for parallel vs. antiparallel spin combinations of the electrons. The Møller polarimeters used in E155 measured the asymmetry in cross-sections for scattering of positive helicity and negative helicity electrons off the polarized electrons in a thin ferromagnetic foil.

The asymmetry for parallel and antiparallel helicity combinations (identified by the zz subscript) is given by [53]:

$$A_{zz} = -\frac{(7 + \cos^2 \theta_{\text{CM}}) \sin^2 \theta_{\text{CM}}}{(3 + \cos^2 \theta_{\text{CM}})^2}. \quad (3.1)$$

The cross-section is larger for the antiparallel spin configuration than for the parallel. At $\theta_{\text{CM}} = 90^\circ$, where the kinetic energies of the scattered and recoil electrons are equal,

the ratio is 8:1, for an asymmetry of magnitude 7/9.

Experimentally, this asymmetry is lessened by the target foil and beam polarizations:

$$A_{\text{experiment}} = \frac{\sigma^{\uparrow\uparrow} - \sigma^{\uparrow\downarrow}}{\sigma^{\uparrow\uparrow} + \sigma^{\uparrow\downarrow}} = P_z^B P_z^T A_{zz}(\theta_{\text{CM}}). \quad (3.2)$$

Thus, the beam polarization P_z^B can be measured by finding an experimental asymmetry $A_{\text{experiment}}$, if the target foil polarization P_z^T and theoretical asymmetry A_{zz} are known.

The E155 Møller system consisted of several components: the polarized foils, a tungsten mask, the magnet B0, and, following several meters of a He-filled box, detectors for the scattered electrons.

The 3-cm-wide polarized foils were made of a ferromagnetic alloy, called permendur, of 49% Fe, 49% Co, and 2% V. There were several foils, ranging in thickness from 40 μm to 154 μm . Most of the foils were used in previous experiments in ESA. Their polarizations have been measured repeatedly and have been stable over time. The foils were mounted in a remotely controlled mover that could position any one of them in the beam for a polarization measurement, or position an opening for the beam for normal (polarized nucleon target, non-Møller) data taking.

A pair of Helmholtz coils provided a ± 100 G field in the target foil chamber, and the unpaired target foil electrons in incomplete shells in the Fe and Co aligned their spins with this external magnetic field. The target foil electron polarization is related

to the bulk magnetization M of the foil by:

$$P_T = \frac{M}{n_e \mu_B} \times \left(\frac{g' - 1}{g'} \right) \times \left(\frac{g_e}{g_e - 1} \right) \quad (3.3)$$

where n_e is the electron number density per unit volume, and $\mu_B = 9.273 \times 10^{-21}$ G cm³ is the Bohr magneton. The free electron g factor $g_e = 2.002319$ relates the angular momentum of an electron to its magnetic moment. The magnetomechanical ratio g' accounts for the contribution from the orbital motion of the electrons to the bulk magnetization. A value of $g' = 1.916 \pm 0.01$ is used, based on an experimental measurement [54] for an alloy of 50% Fe and 50% Co. The error is increased to correspond to uncertainties in earlier measurements and the possibility of a small effect due to the vanadium.

Pickup coils placed around the foils and connected to a precise integrating voltmeter (Schlumberger SI 7061) were used prior to E155 to measure the bulk magnetization of each target foil. The field provided by the Helmholtz coil pair was swept from -100 G to +100 G and the integrated induced voltage in the coil was recorded by the voltmeter. Faraday's law relates the integral of the voltage to the field in the foil. By subtracting the integrated voltage induced in the coil with the foil removed from that with the foil present, the foil magnetization contribution and thus M itself is determined [55].

Located 10 m downstream of the foils was a tungsten mask. The mask had a central hole for the unscattered beam, and two vertical wedge-shaped holes for scattered electrons. The mask, which was 20 radiation lengths thick, selected electrons scattered at lab angles between 3.59 mrad and 8.96 mrad. A head-on view of the mask is shown

in Fig. 3.5.

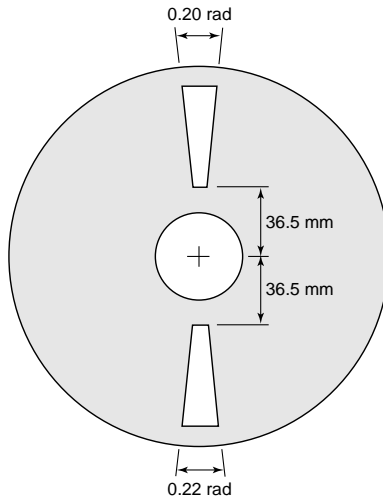


Figure 3.5: Møller mask, with central hole for the unscattered beam and two openings for the Møller scattered electrons.

The vertically scattered electrons selected by the mask were then bent in the horizontal plane by the magnet B0 [56], which was located just downstream of the mask. Magnetic measurements of B0 are discussed in Appendix B. In the middle of the volume of the magnet there was a large iron septum to provide magnetic shielding for the unscattered electron beam. The scattered electrons were deflected by the ~ 1 T field ($\int B dl \approx 3.5 T \cdot m$) to the detector hut, which was located 28.9 m from the foils. The scattering angle and the momentum of each scattered electron were related by kinematics (larger scattering angle = smaller momentum). Therefore, the combination of the mask selecting scattering in the vertical direction and the magnet bending in the horizontal direction produced a Møller stripe of scattered electrons at the Møller detector hut.

In E155 there were two detector systems used for the Møller beam polarization measurements. One system, the double arm, looked for both scattered electrons (one from the beam and the other from the foil) in coincidence. The other system, the single arm, only detected one of the electrons. The single arm was able to detect many more events, but did not have the power of coincidences to cut down on backgrounds. The two systems performed similarly in terms of measurement precision, though the single arm had slightly smaller systematic errors.

For detectors, the double arm used lead glass blocks arranged along the Møller stripes. The blocks were used in pairs as coincidence detectors to detect both Møller electrons. The single arm used 4 cm x 6 cm silicon pad detectors. Each pad was segmented with several channels to provide resolution for locating the Møller stripe. The segmentation of the detector pads also allowed the contribution of background events to be determined by fitting the lineshape of the channels outside of the Møller peak. There were two sizes of channel widths used in the single arm detectors: in the movable fine detector there were 48 channels of width 2.2 mm, and in each of the four fixed coarse detectors there were 12 channels of width 8.7 mm.

3.1.2 Beam Monitoring

To monitor the beam position and quality there were several different systems. While tuning and steering the beam prior to data taking, fluorescent roller screens (coated with ZnS) were placed in the path of the beam. The screens glowed where hit by the beam, and the beam could be steered so the spot on each screen was centered with

respect to a set of projected cross-hairs. Television cameras transmitted pictures of the screens from ESA to upstairs in the counting house.

The beam position during data taking was measured using a foil array which consisted of two sets of 24 foils. One set was vertical and the other set was horizontal, each with applied high voltage relative to a collector anode plane located slightly behind the foils. If the beam passed through a foil, it induced the secondary emission of electrons from the foil. These secondary electrons were gathered by the collector plane, producing a signal current that was read out onto an analog-to-digital converter (ADC). By the location of the peak signal in each of the two sets of foils, the location of the beam could be determined to ± 1 mm.

The amount of charge in each beam spill was measured by two independent toroid monitors. Located upstream of the polarized target, the toroids each consisted of an iron ring with several coil windings around it. As the beam passed through the rings it induced a current in the coil windings. This current was read out through an amplified RC circuit and an integrating charge sensitive ADC. The toroids were calibrated several times per day by using a computer-controlled DAC to charge a 22 nF capacitor which was then able to pass a known amount of charge through the iron rings. The accuracy of the toroids is better than 0.5% [19], which was sufficient for making an asymmetry measurement and negligible compared to the statistical errors and other systematic errors of E155.

For a qualitative measure of beam conditions and stability, two medium-sized plastic

scintillator detectors were placed in ESA. Known as the good spill and bad spill monitors, these scintillators, each about 25 cm x 25 cm, were connected to a short bit of tapered light guide and a phototube, and wrapped in aluminum foil, black paper, and tape. The bad spill monitor was located in the alcove where the beam entered ESA, and if the beam was poorly tuned with many off-energy particles, scattering off a nearby collimator would generate many secondary particles which would hit the detector. The good spill counter was located underneath the polarized target, 2 m below the beam-line, and would see a signal if the beam was hitting the target (or a larger signal if it was hitting part of the surrounding apparatus). The spill counters had their integrated signals both recorded in the data acquisition and shown on an oscilloscope screen which was viewed by a television camera in the counting house. The phototubes were typically run with voltages of -1100 V to -1300 V (good spill) and -800 V to -1100 V (bad spill).

A combination of information from the roller screens, foil array, and spill monitors was used to tune, steer, and watch the quality of the beam.

3.2 Target

To study the spin structure of nucleons by deep inelastic scattering, the most essential item is, of course, a supply of polarized nucleons. In E155 the target material was polarized by placing it in a low-temperature, high magnetic field environment to produce a splitting of energy levels, then driving the transition to the desired polarization state by the application of microwaves. The polarized nucleons and their surrounding

container, vacuum system, cryogenic system, microwave supply, and NMR polarization measurement system were known collectively as the target.

E155 used a target setup that was almost identical to the target used successfully in E143 [57, 58]. A cross-section of the 1-m-diameter target assembly is shown in Fig. 3.6. The available target materials were ammonia ($^{15}\text{NH}_3$), which was used for a proton target, and lithium deuteride (^6LiD), which was used for a deuteron target [59]. In both cases the material was in solid granular form, at extremely low temperature (1 K). The refrigerator provided cooling to maintain the low temperature and offset both the 1 W of microwave power that was directed onto the material and the small amount of heating provided by the beam. The target material was contained in a cell 3 cm long and 2.5 cm in diameter. In each target insert there were two sites (designated upper and lower) for the polarized material, as well as a solid target (C for the proton inserts and Be for the deuteron inserts) for dilution factor determination.

In order to produce a polarized nucleon target, the technique of Dynamic Nuclear Polarization (DNP) was employed. In DNP, microwaves transfer the spins of electrons to the target nuclei of interest. This is done in a strong magnetic field which provides a splitting between energy levels for the various spin states. To polarize nucleons via DNP it is necessary to introduce paramagnetic centers into the target material. This can be done chemically in the case of some materials (such as the butanol or deuterated butanol used by SMC) but is done by irradiation for ammonia and lithium deuteride.

Prior to the experiment, the target material was irradiated at a relatively warm

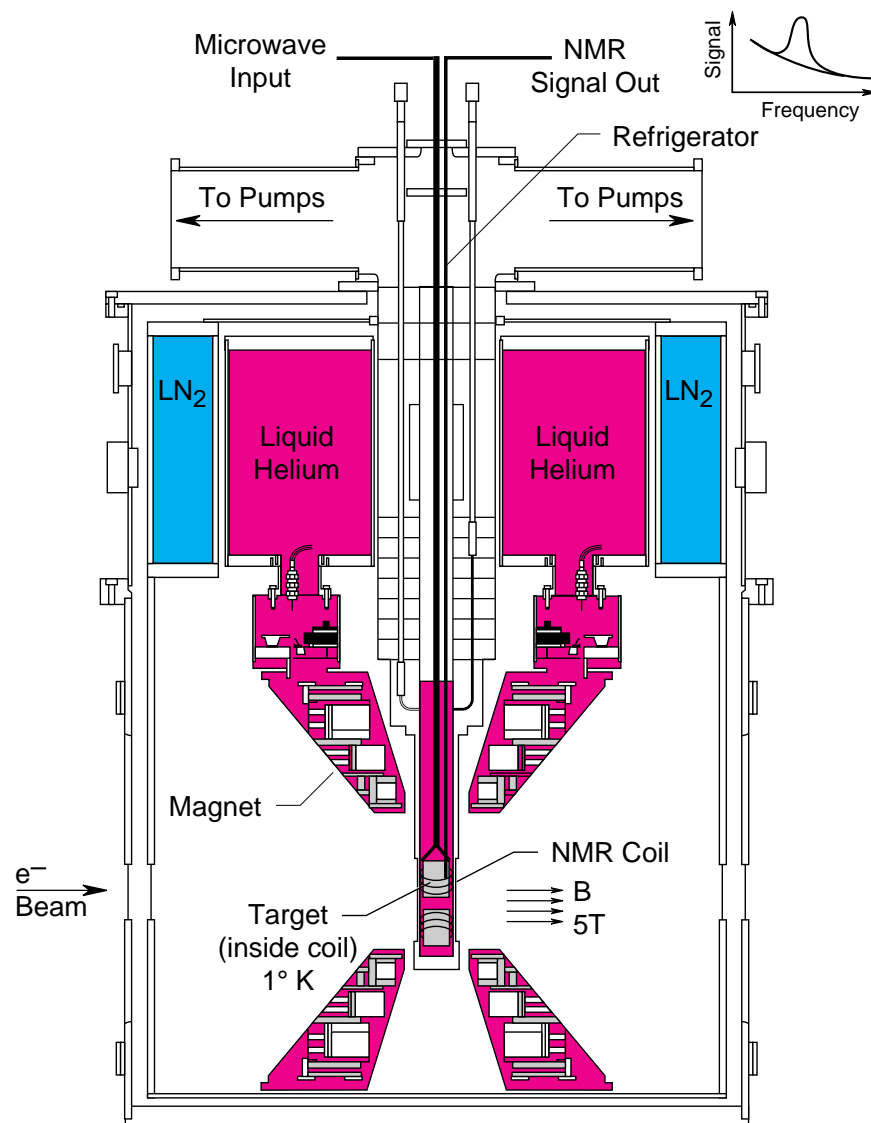


Figure 3.6: The E155 target assembly, cross-section view.

temperature (80-90 K for the ammonia and 180 K for the lithium deuteride) in a low energy electron beam at Stanford's 30 MeV SUNSHINE facility. In this irradiation electrons occasionally displaced a proton or deuteron, creating an ion in the lattice of the crystal. These ions served as the paramagnetic centers where the polarization of the material was initiated.

At low temperature (1 K), obtained by evaporation of liquid ^4He , and in a large magnetic field (5 T), there was a sufficient splitting between the polarization states of the nucleon-paramagnetic center system that directing microwaves of the appropriate frequency onto the target material caused it to be preferentially in one of the polarization states (parallel or antiparallel to the magnetic field direction). For the proton, a spin-1/2 particle, the system looked like Fig. 3.7 [60]. The $W2$ and $W3$ transitions are forbidden by dipole selection rules, and are only weakly coupled by the electron spin–nucleon spin interaction. As a result they are suppressed by a factor of 10^{-3} compared to transitions $W1$ and $W4$. The $W4$ transition, a nucleon spin-flip, occurs at a slower rate than the $W1$ transition, which is a spin-flip of the electron, since the nucleon magnetic moment is smaller and the coupling of the nucleon spin to the lattice is weaker than that of the electron paramagnetic center. Thus the dominant decay mode was the $W1$ transition.

The protons were polarized by applying microwaves of frequency ~ 140 GHz, tuned to drive transition $W3$ (for positive enhancement, target polarization $+\frac{1}{2}$) or $W2$ (for negative enhancement, target polarization $-\frac{1}{2}$). The frequency for the negative enhancement was higher than the frequency for positive enhancement by ~ 350 MHz.

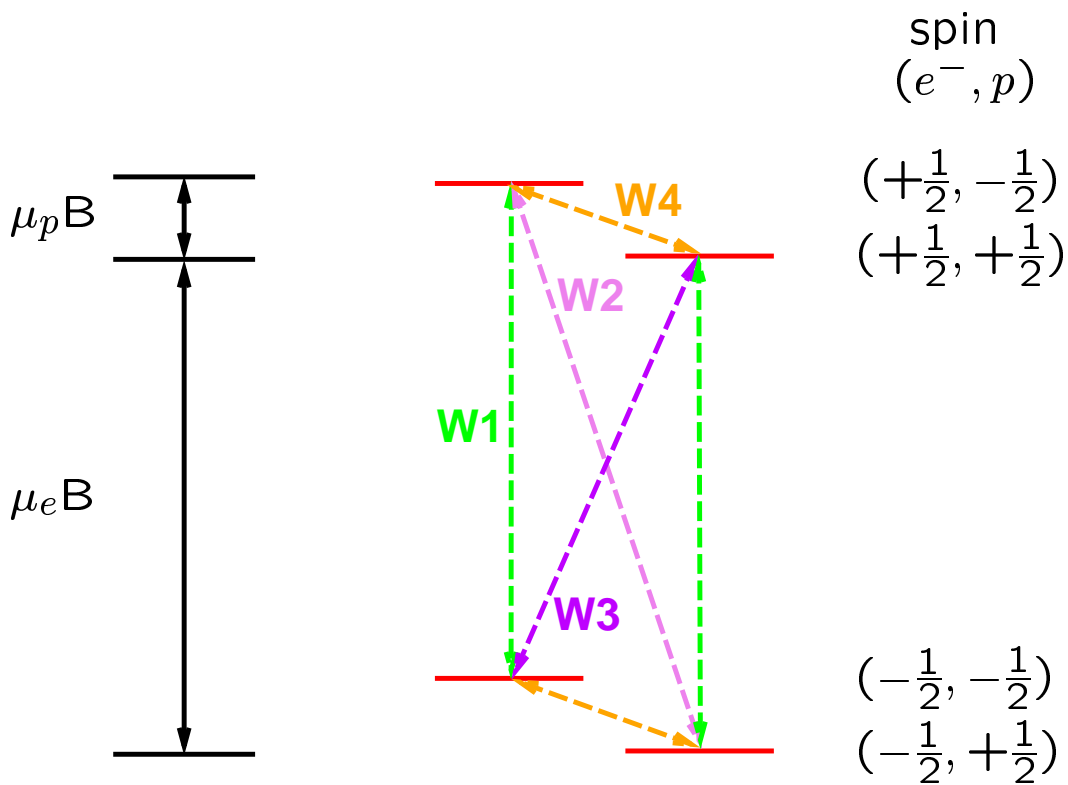


Figure 3.7: Energy levels of the proton-electron system in a magnetic field.

For the deuteron target, the case was similar. The deuteron is a spin-1 particle, so there were six energy levels rather than the four in Fig. 3.7. However, using microwaves to select a normally suppressed transition between states will similarly provide a large polarization. Deuteron polarization is given by the difference between populations of +1 and -1 states divided by the sum of +1, 0, and -1 states. The spin-0 deuteron state acts only as a dilution to the polarization.

The above description of the method for polarization by DNP is only valid for nucleons near paramagnetic centers. There were few paramagnetic centers compared to the overall number of polarizable nucleons. As those nuclei near the centers made the

$W1$ transition to the lower stable states, they transferred their polarization to nearby nuclei via spin-spin interactions, gradually polarizing the nuclei all through the material, a process known as spin diffusion.

The nucleon polarization also decayed through spin-spin coupling with nearby paramagnetic centers, so the presence of too many centers the allowed the polarization to relax to a lower value. (At the maximum polarization value for a given sample, the rate of relaxation is equal to the rate of spinup from the microwaves.) As the target material sat in the beam, new centers were produced. Initially this led to increased polarization as the DNP was able to work more efficiently, but as the number of centers built, their effects of nuclear spin relaxation overwhelmed the DNP and the polarization fell.

The polarization was measured using an NMR circuit which included Liverpool Q-meters [61]. A small coil was embedded in the beads of the material that were actually hit by the beam. The frequency of a signal in the NMR system was swept through the Larmor frequency of the desired nuclear species (listed in Table 3.1) in a 5 T magnetic field. This would cause a small number of the appropriate nucleon

Material	Frequency (MHz)
proton	213.0
^{15}N	21.6
deuteron	32.7
^6Li	31.4
^7Li	82.8

Table 3.1: Larmor frequencies for nuclear species in a 5 T magnetic field.

spins to flip, absorbing (or emitting) energy, thereby affecting the inductance of the NMR coil. The phase shift of the applied RF signal in the LRC circuit (inductance from NMR coil and target material, RC from the Q-meter) provided a relative measure of the polarization of the material within the coil. The area under the phase shift vs. frequency curve for these measurements was proportional to the number of spin flips that occurred. An absolute polarization value was obtained by taking the ratio of the area under one of these curves to the area under the curve for a thermal equilibrium (TE) measurement. TE measurements were made with the polarizing microwaves turned off, and the target was allowed to come to its equilibrium of spin states. This small polarization is calculable and depends only on the temperature, magnetic field, and magnetic moment of the material. For E155 the TE polarizations were typically 0.35% for the proton target and 0.06% for the deuteron. This polarization divided by the area under the corresponding phase shift vs. frequency curve was used as a calibration constant for the measurements with the microwaves on.

Approximately once every two days for the ammonia material and once every six days for the lithium deuteride, an anneal was performed. An anneal consisted of warming the target material up to its pre-irradiation temperature, approximately 85 K for the proton and 185 K for the deuteron. The anneals were attempts to recover some of the loss in polarizability due to radiation damage to the crystal lattice structure and the production of too many extra paramagnetic centers. Following an anneal a TE measurement was usually taken. The decay lifetime of the polarization for a given sample

of material decreased with each successive anneal. The proton target material tended to recover well after anneals, but the lithium deuteride exhibited a drastic reduction in lifetime after annealing. However, this was compensated for by its long lifetime before requiring annealing. During E155 data taking there were only two anneals of the lithium deuteride material.

A target technical run (with no electron beam) was conducted in the month following the primary experiment data taking. During this time TE measurements were taken, and various aspects of the target system and polarization measurements were studied. This included determining the ^{15}N polarization vs. the proton polarization for the $^{15}\text{NH}_3$ material. These values were later used in making a correction to the online proton polarization data.

3.3 Spectrometers

The scattered electrons were detected in three independent magnetic spectrometers. As shown in Fig. 3.8 and Fig. 3.9, the spectrometers were fixed at angles of 2.75° , 5.5° , and 10.5° from the beamline. The spectrometers were designed to detect the high-energy scattered electrons amid a background of many other particles. Some of the backgrounds were low energy particles that caused isolated hits sprinkled throughout the detectors, but high energy hadrons were the primary background that led to falsely reconstructed scattered electrons. Most of these hadrons were pions.

Each spectrometer consisted of a set of magnets followed by three detector systems:

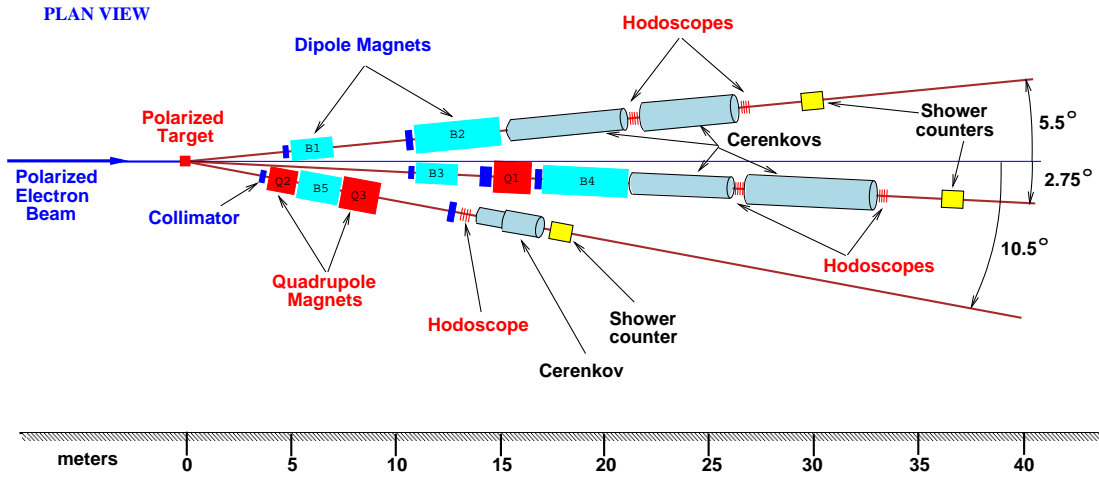


Figure 3.8: The E155 spectrometers.

a lead glass shower counter for energy measurement and particle identification, Cerenkov tanks for particle identification, and plastic scintillator hodoscopes for particle tracking and momentum measurement. The spectrometers were located downstream of the polarized target, and the detectors housed in large shielding huts made of meter-thick concrete blocks. The openings of the spectrometer acceptance were defined with lead blocks and tungsten collimators. The spectrometers were designed to have different areas of kinematic coverage, as shown in Fig. 3.10. The 2.75° and 5.5° spectrometers accepted particles with momentum greater than 9 GeV, and the 10.5° spectrometer accepted particles with momentum greater than 6 GeV.

Once the particles traversed the magnetic fields of the spectrometers, they travelled in straight paths through the detector area in the huts. The tracking software [62] searched for detector hits that were along straight trajectories and that were coincident

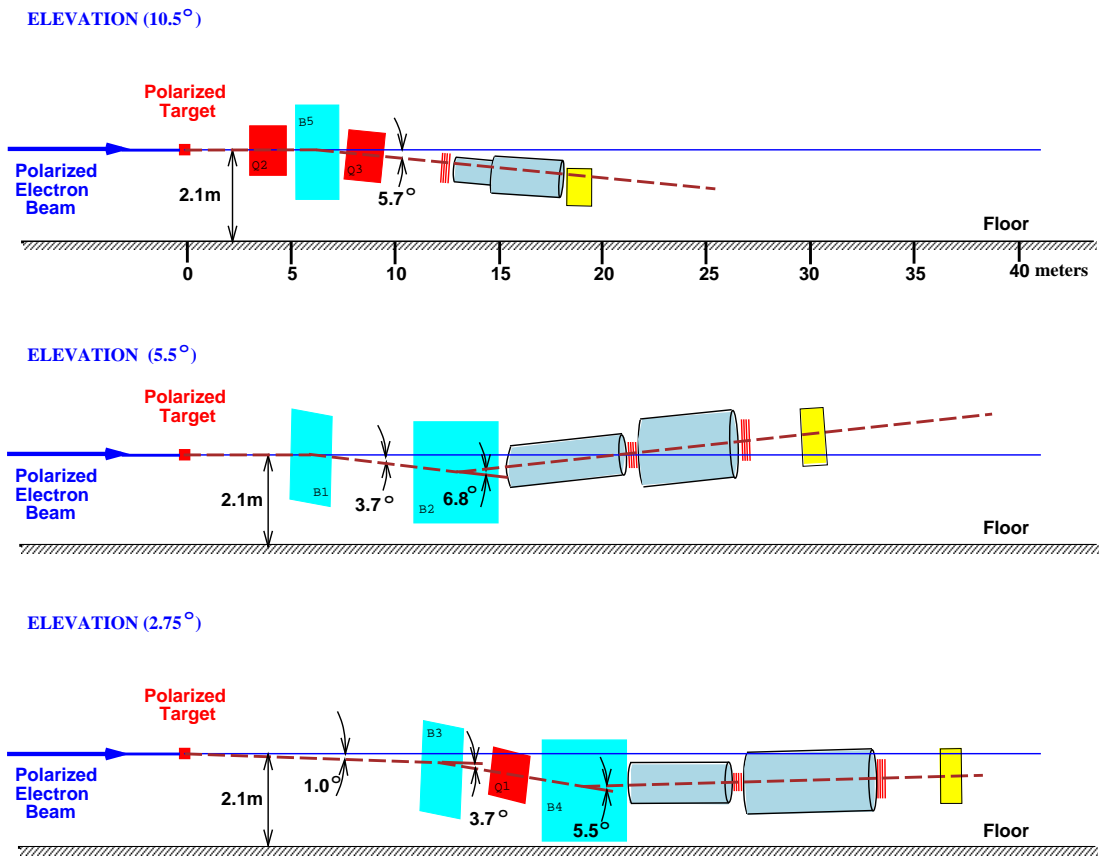


Figure 3.9: The E155 spectrometers, side view.

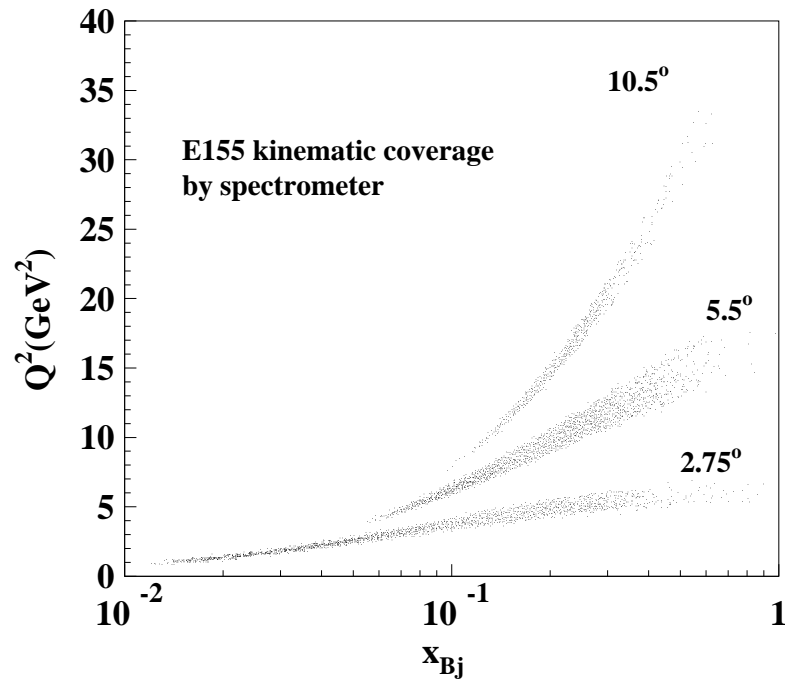


Figure 3.10: Q^2 vs. x kinematic coverage of the three spectrometers.

in time (corrected for time of flight of the particles). Both the space and time resolutions of the detector systems were utilized in the tracking.

A right-handed coordinate system was used in the tracking software in defining the location of the detector elements. Each spectrometer had its own system, based on the definition of its z axis. In the 2.75° and 5.5° spectrometers, a central trajectory was chosen at the central spectrometer angle away from the beamline, and inclined at a slight angle in order to pass approximately through the centers of the detectors. These central trajectories were taken to be the z axes in the respective spectrometers. In the 10.5° spectrometer, the z axis was taken to be a line parallel to the floor at 10.5° from the beamline. The y axis in each spectrometer was taken to be in the plane of a

vertical line and the z axis. The x axis in each spectrometer was therefore taken to be a horizontal axis, directed approximately to the left if looking downstream the beamline.

A model of the optics of the spectrometers and geometry of the detectors was used to generate look-up tables for use in the tracking reconstruction code. A Monte Carlo computer code generated events at the target, which were then propagated into the spectrometers according to the optics model. This resulted in a large sample of simulated events with known initial momentum and scattering angle, and four corresponding track parameters at the shower counter z location: x location, y location, x slope, and y slope. Thus when the tracking code was used on actual data and returned the track location and slope, the look-up tables (indexed on the track parameters at the shower counter) could be used to determine the corresponding momentum of the track.

Tracks found by the software were given one of four exclusive classes based on which detector systems were involved in reconstructing the track. Class 1 tracks were the primary electron candidates, since they had hits in all detector systems (shower cluster, Cerenkov pulse in at least one tank, and hodoscopes). Class 2 tracks were the primary hadron (pion) candidates below Cerenkov threshold, since they consisted of just a shower cluster and hodoscope hits. Class 3 and 4 tracks were not enabled in the main analysis code for E155 and were used only for background studies. Class 3 tracks contained just Cerenkov and hodoscope information, and Class 4 tracks had just hodoscope hits. A flowchart and brief description of the tracking code as it pertained to E155 are given in Appendix A.

The following subsections describe: the spectrometer magnets; the shower counters; the Cerenkov tanks; the hodoscopes; and spectrometer calibration.

3.3.1 Magnets

The 2.75° and 5.5° spectrometers each had two dipole magnets oriented so that their fields were horizontal, which created a vertical bend plane along the central axis of the spectrometer. The 2.75° spectrometer also had a quadrupole magnet to defocus the scattered electrons in the horizontal plane, spatially spreading out the events over a larger area for the shower counter. The two small angle spectrometers used a reverse-bend design, with the dipoles bending in opposite directions. This had the benefit of avoiding a clear line of sight and providing a two-bounce path into the spectrometers for background photons from the target. In the 10.5° spectrometer [63] there was only one dipole magnet, but two quadrupole magnets. The two quadrupoles were oriented with the first focusing and the second defocusing in the horizontal plane. All of the magnets were run at currents between 1500 A and 2900 A.

3.3.2 Shower Counters

Each spectrometer had an electromagnetic calorimeter [64, 65], also known as a shower counter. The shower counters consisted of lead glass blocks instrumented with phototubes. Lead glass was used because it is a dense material, yet it has high transmittance of visible light.

Charged particles entering lead glass interact with the dense material and deposit

some of their energy. High energy electrons, the particles of interest, interacted electromagnetically in the blocks and produced showers of photons and electrons. Electrons incident on lead glass are induced to produce bremsstrahlung, or ‘braking,’ radiation, and the photons from this radiation convert to electron-positron pairs, which in turn radiate and pair produce. This process occurs until the energies of the electrons fall below the critical energy where ionization and excitation losses become equal to the bremsstrahlung losses. For lead glass this critical energy is of order 10 MeV. The point at which the ionization losses start to dominate and the shower contains its peak number of particles (about 5 radiation lengths) is known as the shower maximum. All of the high-energy electrons and positrons in a shower produce Cerenkov radiation, which, for the E155 shower counters, was observed by the phototube at the downstream end of the lead glass block. Through this process, the high energy electrons entering the shower counter deposited all of their energy in a detectable narrow electromagnetic shower.

The total charge of each phototube signal was proportional to the number of photons it detected, and thus also proportional to the energy of the original incident electron. Each phototube signal was sent to an ADC and one or more TDC’s (time-to-digital converters). The TDC’s were operated in leading and trailing edge mode, allowing estimation of the size of multiple pulses in the same block in the same spill. The blocks were combined into clusters, typically each a 3 x 3 grid of blocks. For each cluster in the 2.75° and 5.5° spectrometers, several quantities were fed into a neural network algorithm [66] which differentiated between electron-like and hadron-like showers.

Hadronic particles, such as pions, also undergo ionization and excitation losses in travelling through a material such as lead glass. Since the probability for bremsstrahlung radiation is inversely proportional to the square of the mass of the particle, heavier (than electrons) hadronic particles deposit only a tiny amount of their energy in electromagnetic showers. Hadrons instead deposit energy in the form of hadronic showers, which occur when a hadron undergoes an inelastic collision with a nucleus, producing secondary hadrons, which themselves undergo inelastic nuclear collisions. The length scale of this interaction is much larger than that for electromagnetic showers, so hadronic showers started later in the shower counter and were much broader. Also, much of the deposited energy was lost in the form of nuclear excitation or nuclear breakup, neither of which produces observable signals for phototubes. So compared to electrons, the background hadron particles deposited less of their energy in the calorimeter and only a fraction of that energy was seen in the phototubes.

The shower counter was used for particle identification: for a relativistic electron, its energy and momentum were equal, and so a shower counter event with an E/p ratio of unity is likely an electron. The energy E of an event was determined by adding together the energies reported by each block of the shower cluster, and the momentum p was returned by the tracking software. A shower counter event with an E/p ratio of much less than unity was most likely a pion which didn't visibly deposit much of its energy.

The 2.75° and 5.5° shower counters were made of blocks 6.2 cm x 6.2 cm x 75 cm arranged in an array 10 blocks wide by 20 blocks tall, as shown in Fig. 3.11. The blocks

were oriented in each spectrometer with their long axis in the z direction. The lead glass has a radiation length of 3.17 cm, making them 24 radiation lengths long. The index of refraction of the lead glass is $n=1.62$. The blocks were originally used in the calorimeter in the ASP detector [67], a detector from an earlier experiment at SLAC.

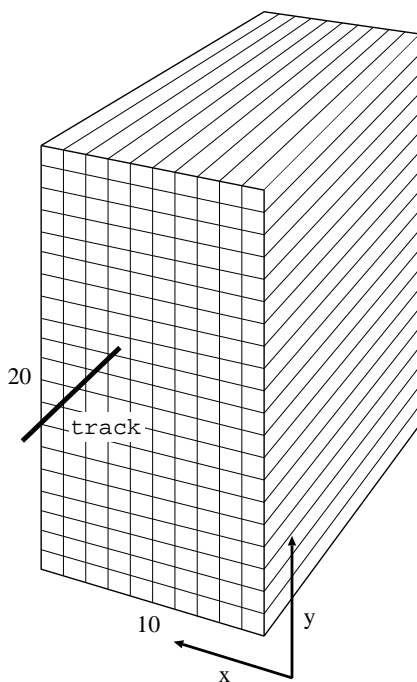


Figure 3.11: The 10 blocks by 20 blocks shower counter arrangement for the 2.75° and 5.5° spectrometers. Each block had a 6.2 cm square face and a length of 75 cm.

The blocks were wrapped with aluminum foil and two layers of black tape. The phototubes, Amperex XP2212PC, were attached at the downstream end of each block with optical epoxy. The 5 cm tubes covered about 40% of the area of the square end of the block. The shower counters in the small angle spectrometers were enclosed in boxes of 0.8 mm aluminum and angled a few degrees horizontally and vertically in order to

avoid the possibility of a particle travelling entirely in the small gaps between blocks.

The 10.5° shower counter [63, 68] was of slightly different construction from the small angle spectrometer ones. It had two components, the pre-radiator (PR) and a total absorber (TA) section.

The PR was built of 10 blocks of the ASP type, with their long axis in the x direction. Each block had a phototube on each end, and from the relative signal sizes the location of a hit along the length of the block could be deduced. In practice, however, the PR did not perform particularly well [68]. This was essentially due to large levels of background, which led to high voltage settings that were too low and discriminator threshold settings that were too high.

Since the PR was not very thick, only two radiation lengths, electrons in the spectrometer passed through it without depositing much of their energy. The TA was an array of 6 blocks in x and 5 blocks in y. Of the 30 blocks, 27 were from the ESA 8 GeV spectrometer, and the other three were from the experiment NE4 [69]. The TA functioned essentially as did the shower counters in the other spectrometers, though due to the larger blocks in many cases an electron shower was contained entirely in a single block.

3.3.3 Cerenkov Tanks

As the particles in each spectrometer traversed the Cerenkov tanks, those travelling above threshold produced Cerenkov radiation, which was reflected by large mirrors onto phototubes in the tanks but outside the acceptance region of the spectrometer.

The thresholds were set to eliminate pions and other more massive hadrons.

All high energy particles traversing a volume of material lose energy to the material. Some of the energy is lost to exciting the material's atoms and molecules, which in turn can re-emit the energy as radiation. For a slow-moving particle, this re-radiation of its lost energy by the medium it is traversing is not coherent and not visible at large distances. But for particles travelling faster than the phase velocity of light in the medium, there is an angle at which this re-emission is coherent and thus is detectable at large distances. This phenomenon is known as Cerenkov radiation [70].

The key principle for the use of threshold Cerenkov detectors is that an electron and a pion of equivalent momentum have different velocities because of their different masses. Therefore the velocity threshold for Cerenkov radiation to be produced corresponds to different momenta for distinct types of particles. This made it possible to set each tank's threshold so that the lowest momentum particles in the spectrometer acceptance (10 GeV in the small angle spectrometers, 6 GeV in the 10.5°) were above threshold if electrons, and were below threshold if pions.

The E155 Cerenkov tanks were filled with a low pressure mixture of 90% N_2 and 10% CH_4 , where the percentages are by partial pressure. The primary gas, N_2 , is a standard choice for Cerenkov applications. The addition of the CH_4 was intended to reduce the component of scintillation light relative to the Cerenkov light [71].

The total pressure of the mixture in a given tank was chosen to produce an index of refraction such that any electron in the spectrometer was above Cerenkov threshold

(~ 50 MeV), while pions were below threshold if they had energy less than 19 GeV for the 2.75° , 16 GeV for the 5.5° , and 16 GeV or 13 GeV (before/after run 2103) for the 10.5° spectrometer. The kaon thresholds in all the tanks were ~ 50 GeV, and the proton thresholds over 100 GeV. The corresponding tank pressures were 1.33 psi in the 2.75° tanks, 1.92 psi in the 5.5° tanks, and first 1.91 psi and then 2.87 psi in the 10.5° tank.

While the 2.75° and 5.5° Cerenkov tanks performed well in experiment E154, they had significant levels of background counts [72]. Prior to E155 the tanks had several cm of lead shielding installed around the sides of the phototube mounts to reduce the number of particles directly striking the tube's photocathode. Each tank in the 2.75° and 5.5° spectrometers had two anodized aluminum baffles installed to cut down on the amount of non-acceptance tank volume visible to the phototube [73, 74]. Also, E154 ran with the tanks using only nitrogen gas and possibly suffered from background due to scintillation light. The 10.5° Cerenkov tank, newly built for E155, also made use of lead shielding and anodized aluminum baffles.

The Cerenkov signals were each split into four CAMAC TDC's and a VME flash ADC (FADC). The TDC's were set at different thresholds, which allowed a measure of the size of the phototube signal for an event based on which TDC levels were fired. The TDC's were a backup for the preferred but less reliable FADC's. The FADC's provided a digitized signal of the phototube output sampled at 1 ns intervals. Output from the 2.75° FADC's for a representative spill is shown in Fig. 3.12.

A software peak-finding algorithm was then used to locate events in the waveform

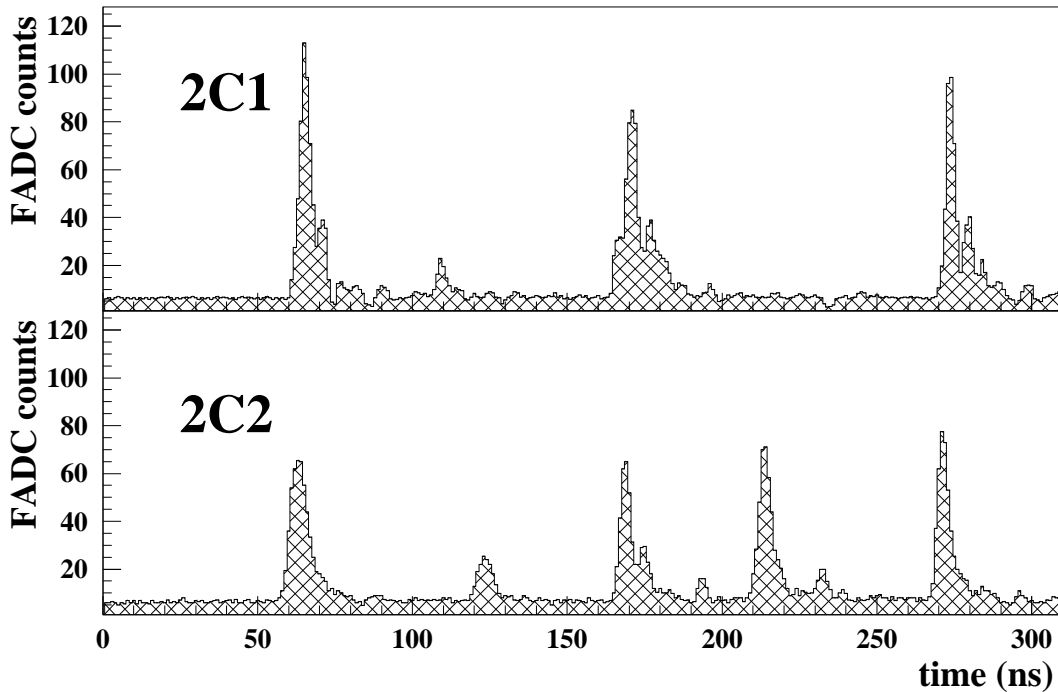


Figure 3.12: FADC waveforms from the 2.75° spectrometer for a single spill in E155 run 1238. Electron events typically had FADC peak signal >30 . In this spill there were three obvious coincidences between the tanks and hence three likely electron events.

and determine their height and integrated size. Unfortunately the FADC's would often shift their timing relative to the data acquisition start, frequently by 4.1 ns. For runs where this was a particular problem a second set of data summary tapes was produced (dst1b and dst1c). A software algorithm was used to identify shifted pulses (with respect to the TDC times) and make a correction to allow the pulses to be matched successfully to track events.

The Cerenkov tanks were all $\sim 95\%$ efficient for electrons.

3.3.4 Hodoscopes

The hodoscope system was used for tracking, to determine accurately the path of a particle in the spectrometer, and thus determine its momentum. The hodoscopes were also used to calibrate the shower counters, since for electron events the track momentum should equal the shower cluster energy.

Each spectrometer had several planes of hodoscopes,¹ where each plane consisted of a number of fingers. A single finger was a long thin piece of plastic scintillator wrapped in aluminum foil (for light reflection) and black electrical tape (for isolation from outside light). Each finger was instrumented with a phototube to detect the scintillation light produced by the passage of an energetic particle. The phototube signals were sent to discriminators and then to TDC's, which were operated in leading-edge only mode. The primary cause of inefficiency in the hodoscope system and tracking was the dead time of the TDC's, the inability to read out the latter of two hits that occurred within a few ns of each other.

The orientation of the fingers in a given plane determined its use in the tracking algorithm: planes of vertical fingers, called x-planes, provided a horizontal coordinate; planes of horizontal fingers, called y-planes, provided a vertical coordinate; and planes of angled fingers (at $\pm 15^\circ$ in the 2.75° spectrometer and $\pm 45^\circ$ in the 5.5° spectrometer), called u-planes and v-planes, provided components of both x and y coordinate infor-

¹According to Webster's Dictionary, a hodoscope is 'an instrument for tracing the paths of ionizing particles by means of ion counters in close array.' The word has its etymology from the Greek 'hodos' meaning road or path.

mation. The combination of time-coincident hits in the x, y, u, and v planes allowed the unambiguous location of multiple track points at each group of hodoscope planes. The small angle spectrometers had two sets of hodoscope planes each, in groups of 6 and 4 for a total of 10 planes in the 2.75° spectrometer, and groups of 4 and 4 for a total of 8 planes in the 5.5° spectrometer. This allowed the tracking reconstruction software to require a track to have three points, one from each set of hodoscope planes and one from the shower counter. The points had to be consistent in space and in time, meaning along a straight line and appearing in the data acquisition in coincidence when accounting for time of flight—taken to be the z-coordinate of the detector divided by the speed of light. Since the spectrometers accepted only particles with momenta greater than a few GeV, and detector time resolution was of order 1 ns, it was sufficient for the reconstruction software to assume the particles were travelling at the speed of light.

The 10.5° spectrometer had comparatively few hodoscope fingers, all of which were in y-planes. The electron rate in this spectrometer was approximately 0.01/spill, so hodoscopes were not necessary for separating multiple electron events. The tracking in the 10.5° spectrometer was in principle much less complicated, since it had only to look for time coincidences and to calculate the slope in y from the hit in the shower counter to the hit in the hodoscopes.

The 10.5° hodoscope was newly built for E155. The 2.75° planes 2H1U, 2H2V were built for E154, and had small finger widths, providing good spatial resolution. Also built

for E154 were 2.75° planes 2H3X, 2H4Y, 2H7X, and 2H8Y, which were split-fingered planes. The fingers in these planes each covered half of the acceptance (rather than having their length extend completely across as in the other planes) in order to cut down on the event rate in a given element. The other planes in the 2.75° spectrometer and all of the planes in the 5.5° spectrometer were used in E154 as well as E143 and E142. There were a total of 538 fingers in the 2.75° spectrometer, 233 in the 5.5° , and 32 in the 10.5° .

3.3.5 Calibration

Each detector system was surveyed to ascertain its location to better than 1 mm. The spectrometer magnets were field mapped [75, 76, 77] prior to the experiment. Using the survey data and magnetic measurements, an optics model of the spectrometers was constructed. This model, which was used to calculate the look-up tables for determining the angle and momentum of spectrometer tracks, was tested against several types of experimental information. First, the acceptance and event rate were functions of momentum and scattering angle. The momentum and angle spectrum of scattered electron events was verified for both normal running conditions and for a series of runs at different beam energies. The energy scan runs were particularly useful since the cross-section dropped rapidly at the high-energy endpoint. Second, special runs were taken with tungsten masks, called sieve slits, placed in the aperture of the spectrometers. The sieve slits had precisely machined holes spaced a few cm apart in a grid pattern. These holes allowed scattered electrons with only specific scattering angles to enter the

spectrometers. The tracking and optics model were tested in their ability to reconstruct the holes in their known locations. Lastly, a test run was conducted in November and December of 1997. For this run, denoted at SLAC as T418 [78, 79], two large dipole magnets were placed in ESA in the location of the polarized target. These magnets and the ESA chicane magnets were used to direct a scavenger 120 Hz electron beam of one electron per pulse directly into the 2.75° and 10.5° spectrometers. By varying the momentum setting of the A-line, electrons of a well-known energy were directed into the spectrometers. The reconstruction software was not burdened with sorting electron events from large numbers of background hits, providing a clean test of the tracking and the shower counter energy calibration. The 2.75° and 5.5° spectrometers had momentum resolution of 2-4%, and angular resolution of 0.5 mrad at low momentum. The 10.5° spectrometer momentum resolution was approximately $\Delta p/p \approx 0.008 p$, where the momentum p is in GeV.

3.4 Data Acquisition

The signals from the many TDC's, ADC's, and discriminators (CAMAC modules) and FADC's (VME modules) were read into a VME-based system [80]. CAMAC and VME are international standards for electronics modules and interfacing to electronics with a computer. The hardware data acquisition system (DAQ) was the interface between the detector electronics and the software DAQ that packed the data for storage on 1 GB data tapes. A schematic of the hardware DAQ is shown in Fig. 3.13. The system

was designed to handle data rates of 10 kB per interrupt, or ~ 1 MB/s. E155 was not a triggered experiment, meaning that all detector information was written out for every beam spill.

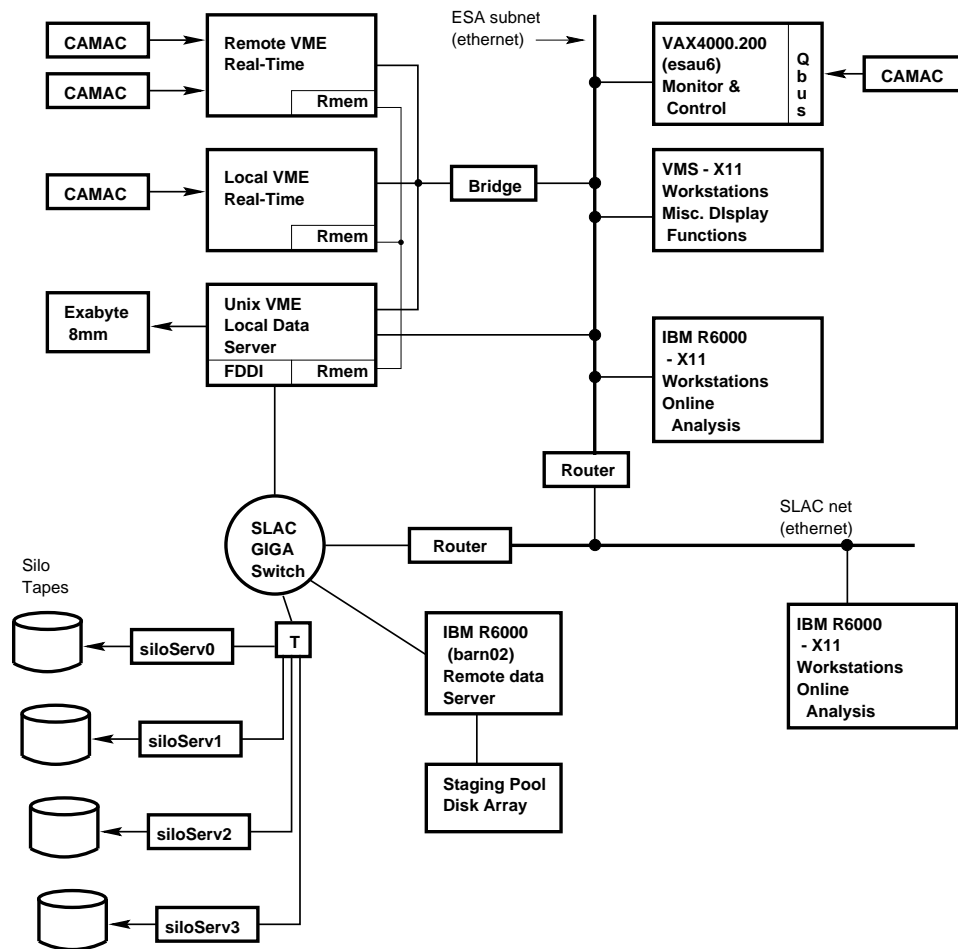


Figure 3.13: Schematic of data acquisition.

In addition to the mostly automated DAQ, there were interactive programs that controlled and monitored the many hardware subsystems: the high voltage to the various detectors, the low voltage in the CAMAC crates, and the power supplies to the

spectrometer magnets. Also, several computer workstations in the counting house monitored the spectrometer data and detector operations.

The experiment wrote raw data to approximately 2000 1 GB data tapes in the robotic silo system at SLAC. The data were first written to a staging pool of disk space in the counting house and then sent over the SLAC computer network to the silo tapes. The data were recorded as approximately 4000 separate runs, of several different types. These types included, along with normal raw data: calibration runs using LED light to send known signals to the detectors; calibration runs for the beam charge toroid monitors; Møller data runs; and pedestal runs, which were short runs with the beam suppressed, taken to determine the level of background electronics noise in each detector channel. Data runs typically took 30 minutes, and ended automatically when enough data were recorded to fill one tape.

Chapter 4

Analysis

In the processing of the raw data tapes, electron events were found using tracking, requiring Cerenkov hits and a cluster with energy close to the momentum of the track. The primary goal of analysis of the data on tape was to determine the asymmetry between the cross-sections for combinations of target and beam polarization: antiparallel and parallel for the parallel target field orientation, and negative and positive beam helicity for the perpendicular target field orientation. The raw asymmetry in the data was found from the rate of electrons detected vs. incident beam charge Q . The beam charge was given by the toroids in ESA. The cross-sections were proportional to the rate N/Q , where N is the number of electrons detected. The constants of proportionality divide out in taking the asymmetry, so the raw asymmetries were found by simple counting:

$$A_{\parallel raw} = \frac{(N/Q)^{\downarrow\uparrow} - (N/Q)^{\uparrow\uparrow}}{(N/Q)^{\downarrow\uparrow} + (N/Q)^{\uparrow\uparrow}} \quad \text{and} \quad A_{\perp raw} = \frac{(N/Q)^{\downarrow\Leftarrow} - (N/Q)^{\uparrow\Leftarrow}}{(N/Q)^{\downarrow\Leftarrow} + (N/Q)^{\uparrow\Leftarrow}}, \quad (4.1)$$

where as previously the arrows indicate helicity of beam (\downarrow and \uparrow) and target (\uparrow and \Leftarrow for parallel and perpendicular configurations, respectively). For the parallel configuration data, the target field was run approximately half the time pointing east and half the time pointing west, where east and west refer to compass direction in ESA and are parallel and antiparallel to the beam direction, respectively. Also, the target was polarized in both positive and negative enhancement modes. The four combinations

of field direction and enhancement mode were counted with the appropriate beam polarization states as overall parallel or antiparallel ($N^{\uparrow\uparrow}$ or $N^{\downarrow\uparrow}$). For the perpendicular target configuration, the target was always polarized in the positive enhancement and the target field was always oriented north (bending the trajectory of the east-travelling electron beam down at the target). For parallel running, the spectrometers accumulated events in the same helicity states, but in perpendicular running there was a relative sign for the 2.75° and 10.5° compared to the 5.5° since they were on opposite sides of the beamline.

The accumulation of events and incident charge was done in kinematic bins in Bjorken x for each spectrometer. For accumulating asymmetries, E155 used one standard set of bins, dividing the region $[0.01,0.90]$ into 38 bins, evenly spaced logarithmically. This set of finely spaced bins was also later combined into a set of coarser bins (11 bins over the same range, known as ‘world binning’) for publication of results. SMC and E154 published their data in similar sets of coarse bins in x , while E143 used the set of fine bins. HERMES has used an entirely different set of bins for their proton data. Each of these spin structure measurements can be thought of as a set of independent experiments performed at slightly different kinematics, where each bin is a separate result. The results in a particular bin affect those of adjacent bins through the calculation of fits for radiative corrections, and are of course related due to finite detector resolution and by overall scale factors such as target and beam polarizations.

Several electron definitions were studied in order to determine optimum levels for

cuts and also to learn about detector efficiencies and contaminations. In any beam spill some number of high energy electrons actually traversed the spectrometers. This number is not necessarily the same as the number of electrons that were reconstructed from the data. Any event definition is characterized by two numbers: its efficiency and its purity. Efficiency is the fraction of the true events that were found. The overall efficiency for E155 was somewhat larger than 80%, with each detector system having an individual efficiency of greater than 90%. Purity is the fraction of events found in the data which were true events. Typically the purity of electron definitions was 95% or greater. Due to differing event and background rates, efficiency and purity both depended on kinematics.

4.1 Data Summary Tapes

The several thousand raw data tapes were processed using a group analysis code and a batch computing system of thirty machines to make data summary tapes, known as DST's. The group analysis code for analyzing raw data was some 20,000 lines of Fortran 90 code, and it took on the order of one day to process a single raw tape to reconstruct all of the electron events. To study the properties of the electron event sample—the efficiency and purity of the cuts—would have required repeating this process for each effect to be studied, an impracticable study due to limitations of computer time.

However, the slowest parts of the analysis were in the reconstruction of the raw data in each detector subset into data more likely to be part of an electron event. The data in

each run was processed spill by spill, as each spill was a separate record on the data tape. In the shower counter, the raw TDC and ADC hits were processed to produce clusters—groups of adjacent blocks which were hit at similar times and whose energy was then added together to produce the energy of the event. In each Cerenkov counter, the raw FADC spectrum was searched for pulses, and the peak height and area underneath each pulse were found. The raw hodoscope TDC hits were grouped together with shower clusters and Cerenkov hits consistent in time and consistent spatially (hodoscopes and shower cluster) with a straight line trajectory through the spectrometer. The grouping of hodoscope hits with a shower cluster, and possibly a Cerenkov event or two, created a track. The processes of clustering and tracking dominated the computer time needed by the analysis software, so the intermediate step of DST's was taken, where the DST's had the raw data distilled into clusters, Cerenkov hits, and tracks. Also stored on DST were enough relevant beam data to enable the spill to be cut on beam quality and location and to know the spill's incident beam charge.

DST's for E155 runs were approximately 1/2 to 1/3rd the size of the raw data. More important than the size of the data set was the processing time. Analyzing one run from DST took approximately 20 minutes, compared to the twenty hours it took to analyze a run from its raw tape.

4.2 Run Selection

Only runs with stable beam conditions and valid target polarization measurements were used for the asymmetry analysis. It was possible for the spectrometers to be set individually in negative polarity or positive polarity, detecting primarily electrons or positrons, respectively. In practice this was done infrequently due to the fringe fields of the spectrometer magnets affecting the operation of the detector phototubes, in particular in the 10.5° spectrometer. Also, there were several occasions where a spectrometer magnet or detector subsystem was not working properly, but the other spectrometers were in fine order. For these runs, analysis was performed for only the working spectrometers' data.

One run was typically twenty to thirty minutes of real time, consisting of 150,000 to 200,000 spills. The typical electron event rate in the spectrometers was 0.5/spill for the 2.75° , 0.2/spill for the 5.5° , and 0.01/spill for the 10.5° . The number of runs analyzed in each spectrometer is given in Table 4.1. The numbers of runs in each row of the table (for each target material) were mostly overlapping sets.

4.3 Event Cuts

The electron definition used in the 2.75° and 5.5° spectrometers was a simple one:

- Class 1 track
- 2 Cerenkov hits, $\sqrt{C1_{pkV} * C2_{pkV}} > 40$
- $0.8 < E/p < 1.2$.

		<u>Proton</u>			<u>Deuteron</u>		
		2.75°	5.5°	10.5°	2.75°	5.5°	10.5°
parallel	e ⁻	497	542	527	471	470	551
	e ⁺	59	38	51	110	142	59
perpendicular	e ⁻	79	82	83	196	209	204
	e ⁺	5	5	5	8	8	8

Table 4.1: Numbers of runs used in E155 analysis.

The basis for an event was a track. A Class 1 track was a combination of shower counter cluster and hodoscope hits and at least one Cerenkov hit. For the electron definition used here, both tanks were required to have a signal, and a cut on the product of the peak signal voltages of the hits in the two tanks was used to maximize efficiency. The shower counter energy was required to be within 20% of the track momentum, since an electron would be expected to deposit all of its energy in the shower counter, while a pion would not. Edge clusters were not used since the energy calibration of edge blocks was less accurate than those in the interior of the calorimeters. Though it was used to study cuts, the shower counter neural network [66] was not part of the electron definition for E155.

The definition used in the 10.5° spectrometer was more complicated, due to less redundancy in the detector systems. The small angle spectrometer definitions were track-based, while the 10.5° definition was a hybrid of track-based cuts and cluster-

based cuts, discussed in detail in Refs. [81, 82]. In summary, the 10.5° definition was as follows:

- Cerenkov hit, $C_{pkV} > C_{low}$
- $E > 5$ GeV
- if a track exists for the event: $E/p > 0.75$
- if no track exists: $E/E_{min} > 0.9$ and $C_{pkV} > C_{high}$ and no ADC saturation
- $E'=E$ for calculating Bjorken x (unless saturated ADC's, in which case $E'=p$)
- $E' > 7$ GeV.

In the above definition: C_{pkV} is the Cerenkov peak voltage from the FADC; (C_{low} , C_{high}) are cuts on minimum peak voltage of (30, 40) for runs prior to 2103 and (45, 60) for runs after 2103; E is the TA cluster energy; p is the track momentum; and E_{min} is a quantity determined by spectrometer optics as the minimum energy in the acceptance for a given row of the shower counter [63]. The hybrid definition was implemented since the hodoscope and tracking were too inefficient to allow a tracking only definition. A stricter cut on the Cerenkov pulse height was assigned (C_{high} vs. C_{low}) for the cluster-based part of the definition.

Cuts on Q^2 and W^2 ($Q^2 > 1$ GeV² and $W^2 > 4$ GeV²) were later used when rebinning the data to ensure that the events were deep inelastic scattering events and not quasi-elastic scatters or scatters in the resonance region.

Examples of the effects of cuts on the raw data are shown in Fig. 4.1 for the 2.75° and 10.5° spectrometers. The 5.5° spectrometer was similar to the 2.75° in terms of detector performance. In Fig. 4.1 the plots in the top half of the figure are for the 2.75° spectrometer, the plots in the bottom half for the 10.5° . The left plots show peak

integrated voltage spectra for all Cerenkov hits in one of the spectrometer tanks, with plots below of the spectra for events in coincidence with a good electron, as defined by the other detectors in the spectrometer (large other Cerenkov hit, E/p or E/E_{\min} cut). The 10.5° plot with the electron cuts still has a large background peak, due to less redundancy in the detector systems. In the 2.75° spectrometer, that peak is removed by requiring a coincidence with the other Cerenkov tank.

The right plots show E/p spectra for all tracks, with plots below of the effect of cuts on that spectrum. With successive cuts, the electron peak at $E/p=1$ gradually appears out of the background of hadron tracks. This is especially evident in the 10.5° spectrometer, where the electron event rate was $\sim 0.01/\text{spill}$, compared to several recorded hadron events per spill. Since the cut on E/p was efficient at removing the hadron events in coincidence with Cerenkov events, the neural network was not used in this analysis.

Cuts were also used on the beam location and quality in deciding whether a spill was a candidate for analysis. Studies were performed by comparing results from different portions of the raster pattern and with using tight cuts on the circular raster pattern. No significant effects were seen, so loose beam cuts were used, as given in Table 4.2. Spills were required to have all four sets of polarization bits in agreement for the beam helicity. Approximately ten runs were not used because of polarization bit disagreements. The Veto polarization bits, which were unreliable for experiment E142, performed well in E155.

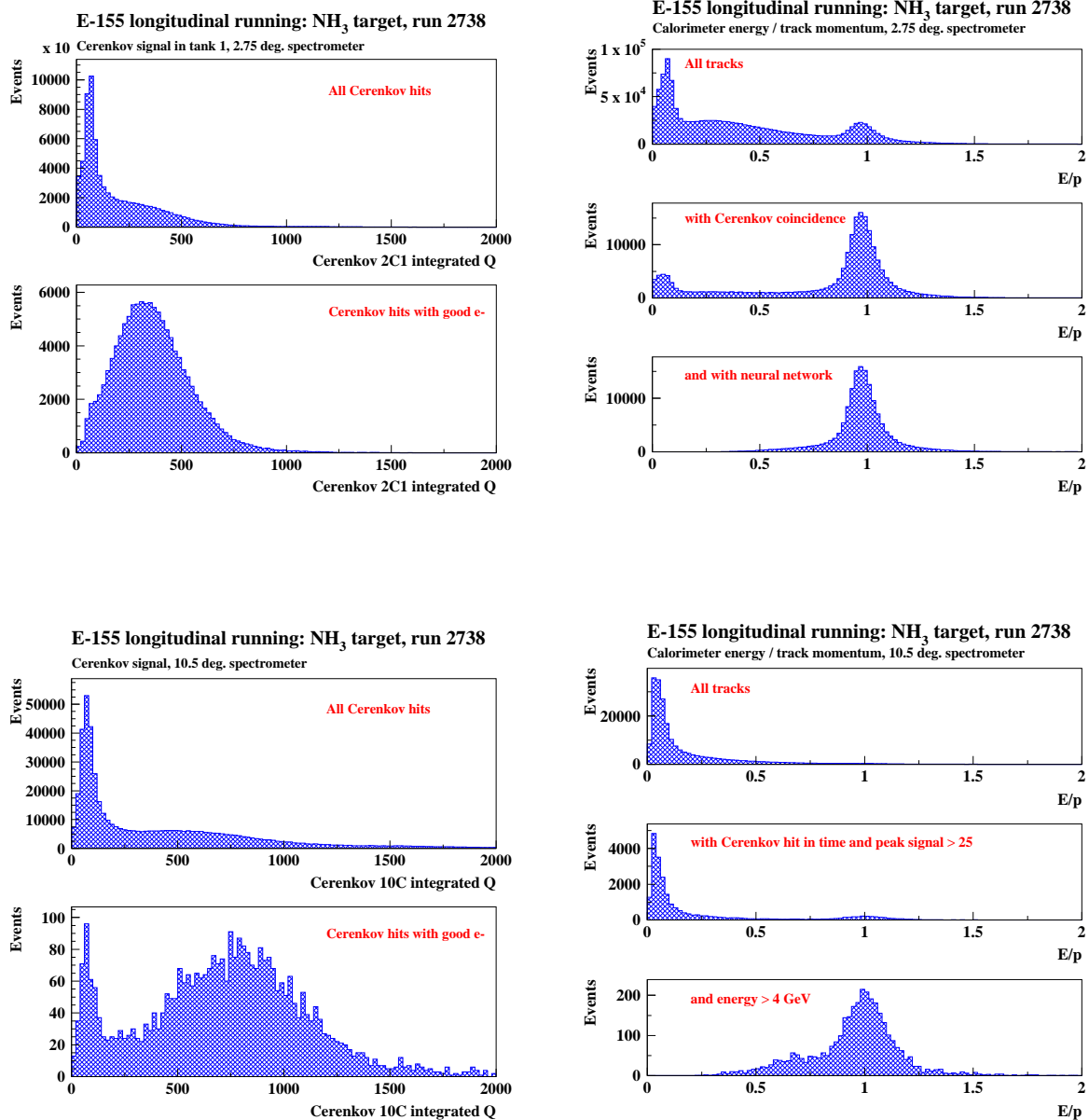


Figure 4.1: Effect on the event sample of cuts in the 2.75° and 10.5° spectrometers. The plots are explained in the text.

quantity	acceptable range
good spill	0–2000
bad spill	0–2000
foil array:	
x	-20.0 – 15.0
x width	0.2 – 5.0
y	-20.0 – 15.0
y width	0.1 – 15.0

Table 4.2: Beam cuts used for final analysis of E155. The spill monitor cuts are in ADC units, the foil array cuts are in mm.

4.4 Raw Asymmetries

Asymmetries were formed first on a run-by-run basis, by taking the ratio of the difference and sum of counts (normalized by incident charge) in the two polarization states. The asymmetries were calculated for each x bin in each spectrometer. Each bin and spectrometer had a statistical error associated with the counting of events. For one helicity state, the counting error is given by $\sigma_N = \sqrt{N}$ for the number of events, and by $\sigma_{(N/Q)} = \sqrt{N}/Q$ for the rate, as the error in the beam charge is neglected. In exact form, the error on the raw asymmetry (Eq. 4.1) is given by

$$\sigma_{A_{raw}} = \frac{2}{Q_L Q_R} \frac{\sqrt{N_L N_R (N_L + N_R)}}{(N_L/Q_L + N_R/Q_R)^2} \quad (4.2)$$

or approximately by

$$\sigma_{A_{raw}} = \frac{\sqrt{(N_L/Q_L^2) + (N_R/Q_R^2)}}{(N_L/Q_L) + (N_R/Q_R)} \quad (4.3)$$

in the limit of small asymmetry ($Q_L \approx Q_R$ and $2\sqrt{N_L N_R} \approx N_L + N_R$). Here the L and R notation is used to represent the two helicity states that were combined to create the asymmetry.

After using the raw asymmetries to calculate A_{\parallel} (or A_{\perp}) for each run, the runs were combined, bin by bin for each spectrometer, adding together the results weighted by the statistical error on A_{\parallel} (or A_{\perp}). This combination occurred after the correction for rate dependence, which was dependent on beam current, and after the correction for the electroweak effect, which was independent of target polarization direction. Other corrections were made to the data after the runs were combined.

4.5 Raw Asymmetries to A_{\parallel}

There were four adjustments necessary to convert the raw experimental asymmetries to the physics asymmetries A_{\parallel} and A_{\perp} . They are: beam polarization (P_b), target polarization (P_t), dilution factor (f), and nuclear corrections (C_1 and C_2). The equation relating A_{\parallel} (and, identically, A_{\perp}) to the experimental asymmetry A_{raw} via these factors is

$$A_{\parallel} = \frac{A_{raw}}{P_b P_t f C_1} + C_2 A_{other} \quad (4.4)$$

where for the parallel running with deuteron target, $A_{other} = A_{\parallel}^{proton}$, and for the parallel running with proton target, $A_{other} = A_{\parallel}^{deuteron}$. For the proton data, C_2 was taken to be zero, as explained below. The factors in the denominator of the first term account for the less than 100% polarization of the beam and target and for the composition of

the target and its surrounding apparatus. The factors P_b , P_t , f , and C_1 and C_2 are described in more detail in the following sections.

4.5.1 Beam Polarization

As described in Section 3.1.1, the beam polarization was measured with two Møller polarimeters. The polarimeters used the same target foils and bending magnet, but had different detector systems. The single arm polarimeter used silicon pads to detect individual scattered Møller electrons. The double arm polarimeter used a pair of lead glass detector sets to detect in coincidence the two Møller scattered electrons from a single event.

The single arm result was $P_b = 0.813 \pm 0.02$. The double arm result was $P_b = 0.805 \pm 0.03$. The errors given are systematic, since the statistical error was typically 0.01 per measurement, and each result was the combination of many measurements made throughout the experiment. The beam polarization used for the analysis is 0.810, the weighted average of the two results. The error is taken to be 0.02, since the errors are largely correlated. No statistically significant variations in the beam polarization were seen over the course of the experiment, so P_b was taken as a constant in the asymmetry analysis. The results of the single arm measurements, taken approximately every three days during the experiment, are shown in Fig. 4.2.

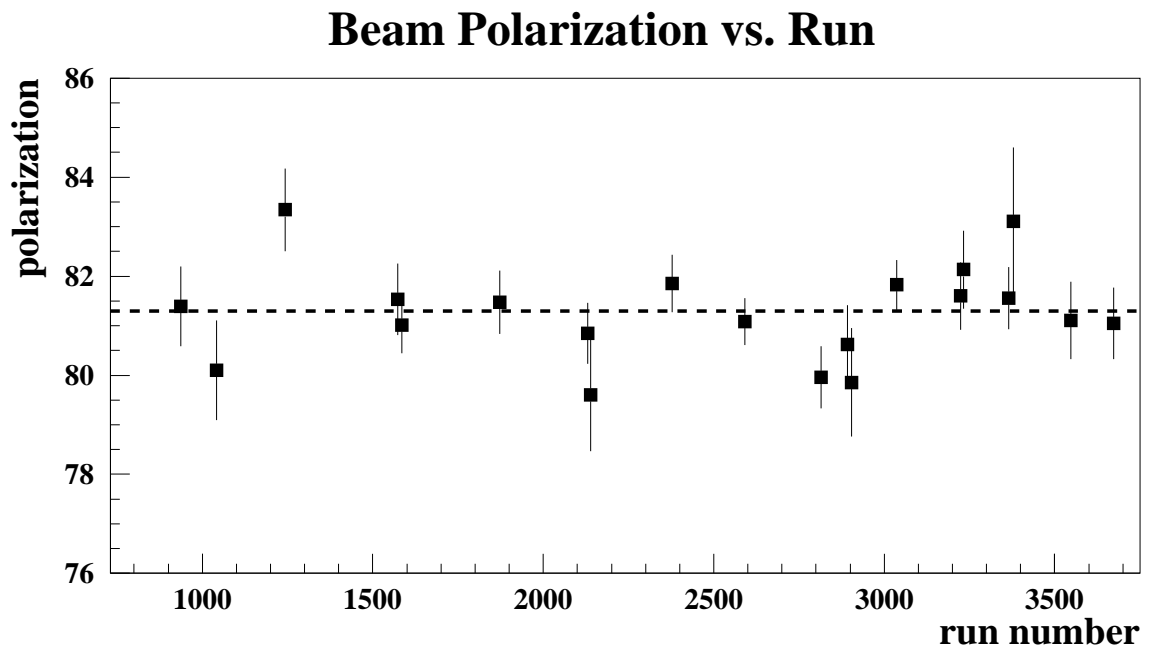


Figure 4.2: Single arm Møller results over the history of the parallel data taking. Each point represents the averaged results from all single arm detectors from one day's measurements, with error bars corresponding to the statistical error. The dashed line represents a constant fit to the data of $P_b = 81.3\%$. The $\chi^2/d.o.f.$ of the fit is 23/19.

Single arm Detectors

In the single arm detectors, each detector saw most of its events in a few channels. This sideways view of the Møller stripe as seen by the segmented detector is referred to as the Møller peak. Møller peaks for run 2588 in the 48-channel fine detector are shown in Fig. 4.3. The notation R-L and R+L refers to the difference and sum of the two beam helicity states. Here the R state had a larger cross-section, so that corresponded to the antiparallel beam-target helicity combination. The overall sign of the beam polarization was determined by knowing the direction of the Helmholtz coil field that polarized the foils.

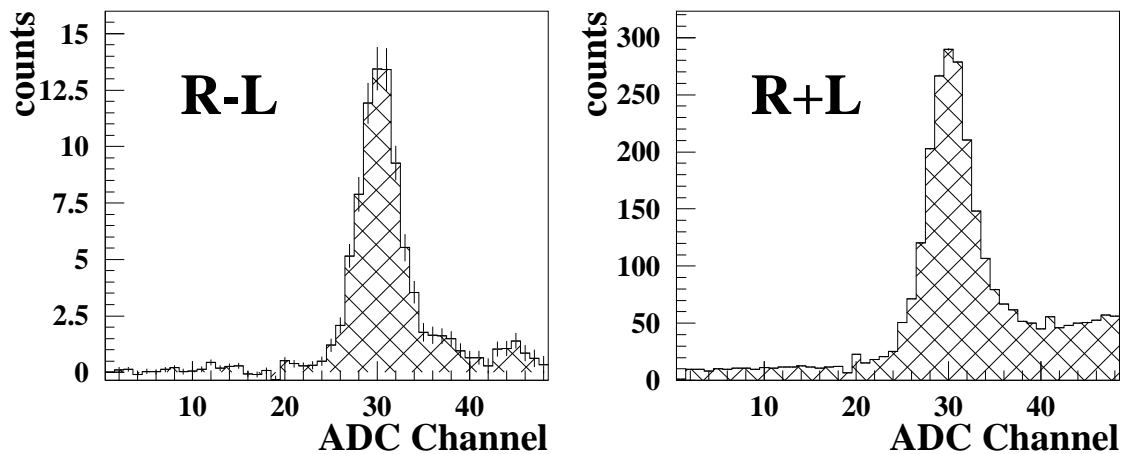


Figure 4.3: Møller peaks in the fine detector from run 2588.

The beam polarization was determined by comparing the experimental asymmetry with the analyzing power, defined as the expected asymmetry for 100% polarized beam. (See Eq. 3.2.) Recalling Eq. 3.1, the asymmetry in Møller scattering, $A_{zz}(\theta_{CM})$, is 7/9

at $\theta_{\text{CM}} = 90^\circ$. The target foils are polarized ~ 0.08 , so the analyzing power is of order $(7/9) \times (0.08) = 0.062$. The asymmetry for this run was, from the peak heights in Fig. 4.3, $\sim 15/300 = 0.05$. Thus the beam polarization for this run was approximately $0.05/0.062 = 0.80$.

However, the polarization determination was more involved than simply taking the height of the R-L and R+L peaks. The analysis of the single arm data used the R-L peak across the channels in each detector to generate a trial line shape for fitting the R+L peak. The R-L line shape was allowed to have a flat background, while the R+L line shape was fit including a cubic background (as a function of detector element location, which was essentially the ADC channel number). The analyzing power was calculated from a Monte Carlo model code, which included: the field strength of B0, Levchuk corrections [83], multiple scattering, bremsstrahlung, detector resolution, and the gaps between the two silicon pads making up each detector. The Levchuk corrections accounted for the smearing of the peaks due to the atomic motion of the target foil electrons. The R-L line shape is produced by scattering involving only the polarized M-shell electrons in the Fe and Co in the foil, while the R+L line shape is produced by scattering involving electrons from all of the shells in the materials in the foil. The correction is necessary since M-shell electrons have a different average orbital energy from the average of all the foil electrons, and so the R-L and R+L peaks are smeared differently.

The asymmetry for a particular Møller run was then determined by taking the

ratio of the R-L line shape function integrated over the Møller peak and the similarly integrated R+L line shape. The polarization result for a particular run was determined from the asymmetry and the calculated analyzing power.

For the parallel data, taken at $E_0 = 48.35$ GeV, the polarization bits (for example, `bcal_pmon_polar` in the `beam155.inc` include file in the analysis code) corresponded to helicity as: 1=positive e^- helicity in ESA, 2=negative e^- helicity in ESA. At 48.35 GeV the electron spins precessed 15π as they followed the 24.5° bend in the A-line. For the perpendicular data, taken at $E_0 = 38.77$ GeV, the electron spins precessed 12π , so the helicity flags in the analysis code refer to opposite polarization states with respect to the parallel data.

As discussed in Section 3.1, because of the A-line bend the beam polarization in ESA is a function of beam energy. Neglecting losses to synchrotron radiation, there is a cosine dependence from the spin precession. Thus measuring the polarization as a function of energy was a way to determine the beam energy accurately. For both the parallel and perpendicular running an energy scan was performed with the single arm system. The data and a fit from the parallel running scan are shown in Fig. 4.4.

The fit to the energy scan for parallel running resulted in a correction of +50 MeV to the A-line reference magnet flip-coil readings. The average flip-coil reading for the parallel running was 48.30 GeV (with fluctuations ± 0.02 GeV), so the beam energy in the parallel data analysis was taken as a constant 48.35 GeV. For perpendicular running, the flip-coil readings averaged 38.79 GeV. The energy scan for the lower beam

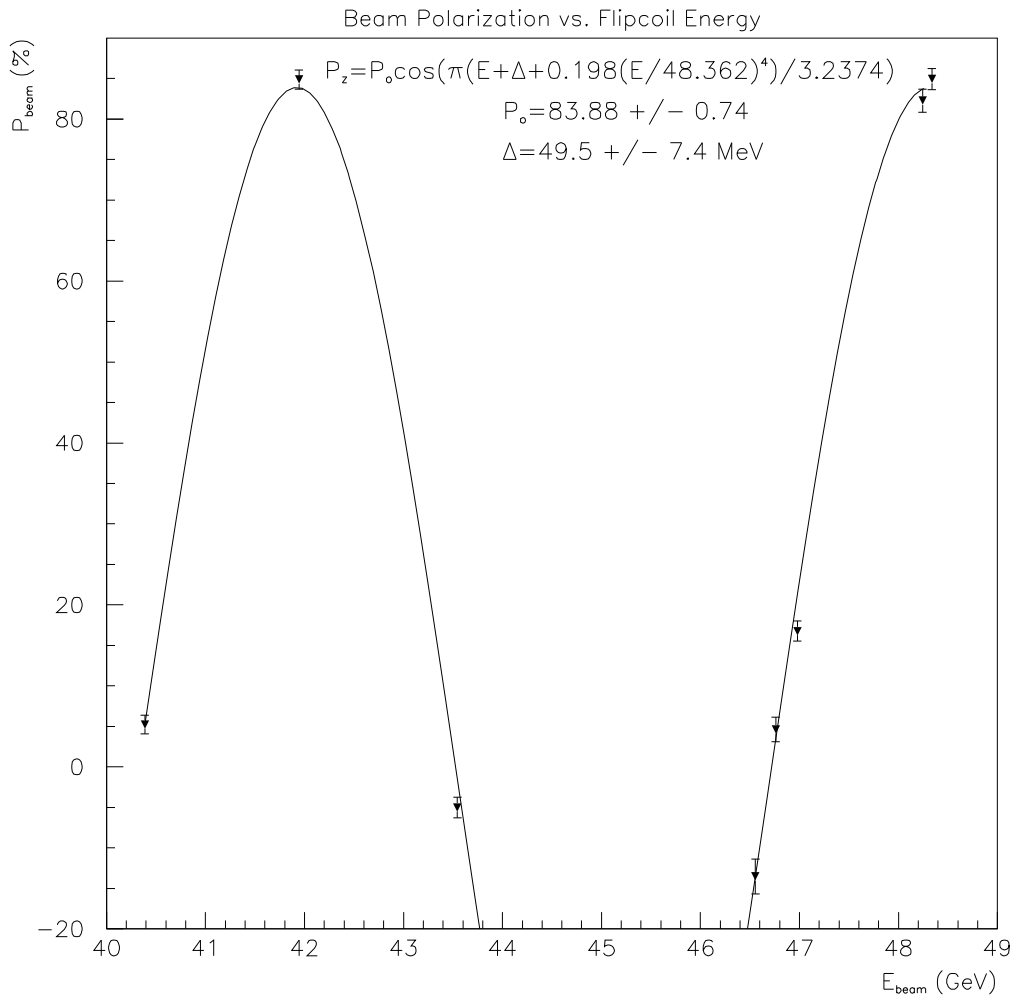


Figure 4.4: The Møller energy scan for parallel running (runs 576-654). The expression on the plot is a fit of the polarization to a cosine dependence on the beam energy. Also included is a term with E^4 to account for synchrotron radiation losses. The result of the fit is a maximum polarization of $P_0=0.84$, with an offset of 50 MeV in the beam energy with respect to the A-line reference magnet flip-coil reading.

energy resulted in a correction of -21 MeV. The beam energy in the perpendicular data analysis was taken as a constant 38.77 GeV.

The systematic errors for the single arm Møller system are given in Table 4.3.

foil polarizations	
common	1.2%
foil to foil	1.2%
analyzing power	1.0%
Monte Carlo stat. & syst.	
$\int B \cdot dl$	
sensitivity to background shape	1.2%
sensitivity to integration range	0.4%
analysis technique	0.9%
total	2.5%

Table 4.3: Systematic error contributions to beam polarization for the single arm Møller system.

Double arm detectors

The double arm Møller detectors consisted of two sets of seven lead glass blocks, one set above the beamline and the other below. The blocks were arranged to be on the two Møller stripes, which came from the two wedge-shaped holes in the mask. The middle block of each set was placed to be at $\theta_{CM}=90^\circ$. The blocks furthest from the beamline were at $\theta_{CM}=70^\circ$, while those closest to the beamline were at $\theta_{CM}=110^\circ$. Thirteen pairs of blocks were used as essentially separate detectors. Each pair consisted of one block from the top set and one from the bottom set, and most blocks were used in more than one pair. The predicted asymmetry in each pair varied according to their θ_{CM} (according to Eq. 3.1, which is symmetric about 90°).

The double arm analysis accounted for dead time (typically 1-8%) and crosstalk between the detectors [84]. The double arm detectors were sensitive to the overall rate and a rate dependence correction was included [85]. There was no detailed study of double arm polarimeter systematic errors. Though it was averaged with the single arm result to produce a final beam polarization measurement, the double arm result is regarded as a cross-check.

4.5.2 Target Polarization

A brief synopsis of the inserts and target materials used in E155 is given in Table 4.4. The notation Al for NMR coil material actually refers to a copper-plated aluminum wire.

	Insert	Cell	Material	NMR Coil	Runs	Dates
parallel	1	UPPER	LiD	Al	2-1874	2/7-3/17
		LOWER	LiD	Al		
	2	UPPER	NH ₃	Al	1876-1986	3/17-3/19
		LOWER	NH ₃	Al		
	3	UPPER	NH ₃	Al	1987-2574	3/19-3/28
		LOWER	NH ₃	CuNi		
	4	UPPER	NH ₃	CuNi	2575-2853	3/28-4/2
		LOWER	NH ₃	CuNi		
	5	UPPER	LiD	Al	2859-3404	4/2-4/11
		LOWER	LiD	CuNi		
	6	UPPER	NH ₃	CuNi	3405-3701	4/11-4/16
		LOWER	NH ₃	CuNi		
perpendicular	10	UPPER	LiD	Al	3787-4388	4/23-4/30
		LOWER	NH ₃	CuNi		

Table 4.4: E155 polarized target insert history [86].

There were many problems with the proton target polarization [87]. The proton NMR signals were inverted, and several online polarization readings were greater than 100%. These problems arose from at least two factors.

First, since E143 was microwave power limited in polarization, the E155 target cell was metal (copper-coated aluminum), for microwave power containment. Ammonia has a high dielectric constant, and thus between the NMR coil and cell walls, the cell itself acted as a capacitor. Later simulations have shown that a capacitance in the target cell, on order of that already in the Q-meter, was sufficient to violate the NMR condition of constant current and produce inverted signals. A correction [88] was applied to the online NMR polarization measurements based on E143 and E155 target technical run data for ^{15}N vs. proton polarization and an assumption of EST as a high-end anchor to the correction. The ^{15}N polarization measurements were not affected by the additional capacitance since the Larmor frequency of ^{15}N in the 5 T field was an order of magnitude smaller than that of the proton.

Second, the proton target data taken with the Al NMR coil (10% of the proton data set) were discarded due to small, distorted NMR signals and a large nonlinearity in its raw physics asymmetry vs. polarization. The NMR signals were five times smaller than for the CuNi coil proton data. This was possibly due to the copper plating on the aluminum wire providing additional capacitive effect. In principle the coil material itself should not have affected the polarization measurements.

The deuteron target polarization is used essentially as measured online. The data

from the lower cell of insert 5 were not used for the 2.75° and 5.5° spectrometers due to an insufficient number of good quality TE measurements. The insert 5 lower cell data were a large fraction (30%) of the events recorded on the 10.5° spectrometer, and they were included for that spectrometer with a polarization correction factor of 0.5 [89] based on normalizing the physics asymmetry of the (unused) insert 5 lower cell data in the other two spectrometers. This correction factor was multiplicative and applied to the measured online polarizations.

The target polarization vs. run number is shown in Fig. 4.5. Proton anneal cycles were much shorter than those for the deuteron, as evidenced by the shorter segments of its polarization history curves.

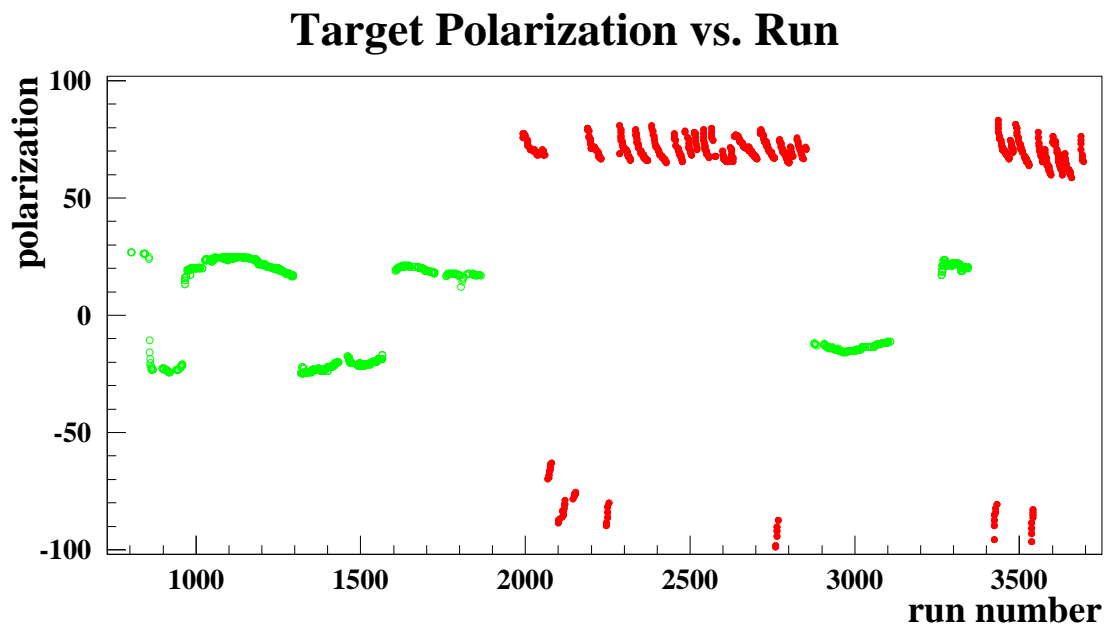


Figure 4.5: E155 target polarization vs. run number, parallel data. The larger values (near $\pm 75\%$) are proton runs, and the smaller values (near $\pm 20\%$) are deuteron runs.

4.5.3 Dilution Factor

The polarized target assembly by necessity placed unpolarized materials in the path of the electron beam. These materials—aluminum windows; NMR coils of copper, nickel, or aluminum; liquid helium; gaseous helium; and air—were a small but significant amount of material compared to the amount of the target material itself. In addition to protons and deuterons, the target material contained many other nucleons: the fifteen nucleons in the nitrogen nucleus in the ammonia, and the six nucleons in the lithium nucleus in the lithium deuteride. The fraction of scattered electron events in the spectrometers that originated from scattering off the nucleons of interest was called the dilution factor.

The dilution factor for the proton target was defined as the ratio of the number of polarizable protons (hydrogens in the ammonia) to the total number of nucleons. (Or, more precisely, it was defined as the ratio of the cross-sections.) In the deuteron target, it was the ratio of free polarizable deuteron nucleons to the total number of nucleons. The deuteron dilution factor did not include a numerator contribution from the effective deuteron in the lithium, as that was accounted for by the C_1 factor as described below. The deuteron dilution factor did include a $3.3\% \pm 1.5\%$ correction for oxygen contamination of the LiD material [90]. Including this correction made the deuteron f smaller and the asymmetry correspondingly larger.

One important component of the dilution factor calculation was determining the packing fraction for each cell of each insert. This was the fraction of volume in the cell

occupied by the target material. Both the ammonia and lithium deuteride were in the form of small granules, and the packing fractions were all in the range 0.52–0.61. These numbers were determined experimentally by comparing the spin-averaged deep inelastic scattering rates for the polarized material with the scattering rates for a similar solid target. For the ammonia a reference target of solid carbon was used, and for the lithium deuteride a target of beryllium was used. The solid targets and their thicknesses were chosen to match closely the density and radiation lengths of the polarized target materials. The ratio of the solid target and polarized target scattering rates was compared to the theoretical ratio of rates for these materials. The packing fractions were calculated from ratios of these ratios. The packing fractions were measured as functions of Bjorken x for each spectrometer, and with the appropriate radiative corrections to the ratios of rates, were observed to be constant. Since each packing fraction was a simple number (representing a ratio of volumes), and not a function of anything, this was an important cross-check. The packing fractions by E155 insert number are given in Table 4.5.

The average dilution factors vs. x for the 2.75° spectrometer are shown in Fig. 4.6. The 5.5° and 10.5° spectrometers had average dilution factors approximately 2% and 6% higher, respectively. This arose from the spectrometers having different acceptance for events originating in the upstream and downstream windows of the target assembly—the 2.75° spectrometer, by its smaller angle, saw more events from these windows and had a smaller dilution factor.

The systematic error on the proton dilution factor was 2.5%. For the deuteron

Insert	Cell	Target Material	Packing Fraction
1	UPPER	LiD	0.526 ± 0.013
	LOWER	LiD	0.575 ± 0.013
2	UPPER	NH ₃	(not used)
	LOWER	NH ₃	0.584 ± 0.031
3	UPPER	NH ₃	0.570 ± 0.019
	LOWER	NH ₃	0.555 ± 0.015
4	UPPER	NH ₃	0.540 ± 0.033
	LOWER	NH ₃	0.586 ± 0.021
5	UPPER	LiD	0.534 ± 0.017
	LOWER	LiD	0.554 ± 0.014
6	UPPER	NH ₃	0.594 ± 0.017
	LOWER	NH ₃	0.610 ± 0.021
10	UPPER	LiD	0.522 ± 0.026
	LOWER	NH ₃	0.583 ± 0.040

Table 4.5: Packing fractions by E155 insert number.

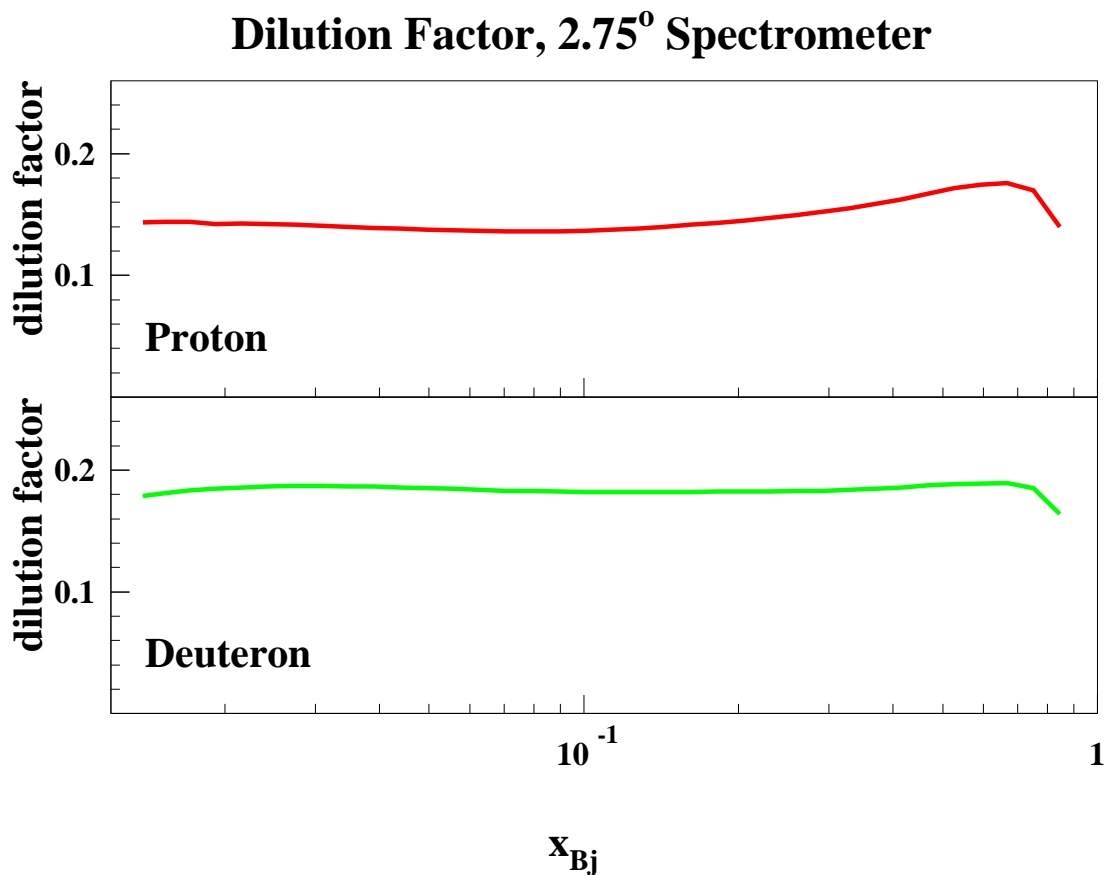


Figure 4.6: E155 average dilution factor for proton and deuteron targets.

dilution factor systematic error, this value was added in quadrature to the 1.5% error from the oxygen contamination correction, yielding a total error of 2.9%.

4.5.4 Nuclear Corrections

Aside from the polarized protons and deuterons, there were many materials in the target that provided scattering centers for the electron beam. The dilution factor accounted for the fraction of events originating in these materials. However, some of the other nucleons in the target material itself were polarized, and these contributed not only counts, but

also to the observed asymmetry. The corrections to the experimental asymmetry due to other polarized materials are termed nuclear corrections, and denoted by C_1 and C_2 .

Proton

There were two primary nuclear species in the proton target: ^{15}N and ^1H . The ^{14}N fraction of the nitrogen was 2% and had no significant effect on the measured asymmetries. The choice of ^{15}N as the preferred isotope is that corrections for its polarization are easily interpreted in terms of a proton contribution of opposite sign. Also, since the ^{14}N NMR response is comparatively broad, the polarization of ^{15}N is more easily measured. Measurements of the ^{15}N polarization vs. the proton polarization for the $^{15}\text{NH}_3$ material were made during the target technical runs of E143 and E155.

Recalling Eq. 4.4,

$$A_{\text{unsubtracted}} = \frac{A_{\text{raw}}}{fP_bP_tC_1} + C_2A_{\text{deuteron}}, \quad (4.5)$$

the approximation of no ^{14}N in the target yields $C_2 \equiv 0$. A_{raw} refers to the raw asymmetry of events per incident charge, as written in Eq. 4.1. $A_{\text{unsubtracted}}$ refers to the corrected raw asymmetry that, once backgrounds are removed and radiative corrections applied, will become A_{\parallel} or A_{\perp} .

The factor C_1 is calculated by:

$$C_1 = 1.0 + (1 - \eta_N) \frac{P_{15}}{P_p} \beta_{15} g_{15} \left(\frac{1}{3} \right). \quad (4.6)$$

Values used for the terms in Eq. 4.6 are given in Table 4.6. The EMC effect correction is detailed in Ref. [91]. A derivation of Eq. 4.6 is given in Ref. [92].

$\eta_N = 0.02$	fraction of N that was ^{14}N instead of ^{15}N
P_{15}	^{15}N polarization, see Eq. 4.7
P_p	corrected proton polarization, see Section 4.5.2
$\beta_{15} = -1/3$	Clebsch-Gordan coefficient for N wave function
$g_{15} \approx 1$	^{15}N EMC effect
$1/3$	factor for ratio of N to H in ammonia

Table 4.6: Values for terms in the proton nuclear correction C_1 .

For the ^{15}N (in $^{15}\text{NH}_3$) polarization as a function of the proton polarization, a fit by E143 [8] was used:

$$P_{15} = -(0.13561 \times P_p - 0.18286 \times P_p^2 + 0.33482 \times P_p^3). \quad (4.7)$$

The fit was based on data from the target technical run which followed the E143 experiment. For a typical proton polarization of $P_p=0.80$, this relation yields $P_{15}=0.16$. The average value of C_1 for the proton was 1.024. Taking a systematic error of 20% on the second term in Eq. 4.6 gives a systematic error on C_1 of 0.5%.

Deuteron

In the deuteron target there were two isotopes each of lithium and deuterium. The desired target species was ^6LiD , but some fraction of the lithium was ^7Li , and some fraction of the hydrogen was ^1H . The advantage of ^6Li over ^7Li is that, to the extent it can be treated as an alpha particle and a deuteron, then half of the nucleons in ^6LiD are in deuterons. Derivations of the following corrections for the deuteron target are

given in [92, 93, 94].

Again recalling Eq. 4.4, here for the deuteron,

$$A_{unsubtracted} = \frac{A_{raw}}{f P_b P_t C_1} + C_2 A_{proton} , \quad (4.8)$$

for the deuteron target the corrections C_1 and C_2 were calculated by:

$$C_1 = (1 - \eta_p) + (1 - \eta_L) \frac{P_6}{P_d} \beta_6 g_6 \frac{1}{\gamma_d} \quad (4.9)$$

and

$$C_2 = \left(\frac{-1}{C_1} \right) \left[\eta_p \frac{P_p}{P_d} + \eta_L \frac{P_7}{P_d} \beta_7 g_7 \left(\frac{F_2^p}{2F_2^d} \right) \right] . \quad (4.10)$$

Values used for the terms in Eqs. 4.9 and 4.10 are given in Table 4.7. The polarizations of ${}^6\text{Li}$ and ${}^7\text{Li}$ vs. the deuteron polarization were measured in the target technical run and found to be consistent with EST predictions [59].

The two terms in Eq. 4.9 represent contributions from the deuteron and the deuteron-in-lithium respectively. There is a contribution of almost 1 from the free deuteron, and of less than 1 for the deuteron in the lithium (since it isn't a free deuteron and is some fraction of the time in other states). To first order $C_1 = 1.86$. The combination fC_1 can be viewed as an effective dilution factor, and for the lithium deuteride $fC_1 \approx 0.34$. The systematic error on the C_1 factor is 2.7%.

To first order C_2 is small since the η 's are small. The two terms in Eq. 4.10 are for the residual protons (that were supposed to be deuterons) and for the ${}^7\text{Li}$. The overall effect of the correction $C_2 A_{proton}$ is of order 5%. The relative systematic error on this second term of Eq. 4.8 is 12.6%.

$\eta_p = 0.025$	fraction of H that was ^1H instead of D
$\eta_L = 0.046$	fraction of Li that was ^7Li instead of ^6Li
P_d	measured deuteron polarization
$P_p = 0.04$	proton polarization (an estimated limit)
$P_6 \approx P_d$	^6Li polarization, actually used EST estimate
$P_7 \approx 3 \times P_d$	^7Li polarization, actually used EST estimate
$\beta_6 = 0.866$	model calculation of effective neutron polarization (as fraction of ^6Li polarization) in $^6\text{Li} = \alpha + p + n$
$g_6 \approx 1$	^6Li EMC effect
$\beta_7 = \frac{2}{3} = 0.667$	Clebsch-Gordan coefficient for extreme shell model effective polarization of the proton in ^7Li as a fraction of the ^7Li polarization
$g_7 \approx 1$	^7Li EMC effect
$F_2^p/(2F_2^d)$	used to get $\frac{\sigma_p}{\sigma_d} = \frac{\sigma_p}{\sigma_p + \sigma_n}$
$\gamma_d = 0.925 = 1 - 1.5\omega_D$ $\omega_D = 0.05 \pm 0.01$	free deuteron D-state correction

Table 4.7: Values for terms in the deuteron nuclear corrections C_1 and C_2 .

4.6 A_{\parallel} Corrections

Once A_{\parallel} (and A_{\perp}) were calculated from asymmetries in count rate with adjustments for target polarization, beam polarization, dilution factor, and nuclear effects, further corrections were applied. These included small corrections for: electroweak effects; rate dependence; pion/positron contamination; and detector resolution. Finally, radiative corrections were applied, yielding results for the Born-level physics asymmetries.

4.6.1 Electroweak Correction

A small correction [95] was made for the electroweak asymmetry [96]. This is an asymmetry in the deep inelastic scattering of left and right-handed electrons in the process $e_{R,L}N \rightarrow eX$, which arises due to the interference of the electromagnetic scattering amplitude with that for the weak interaction.

This effect does not depend on the target polarization, so it can be minimized experimentally by taking data with the target polarized each direction half of the time. Consider two polarization configurations: target polarization parallel to positive helicity beam; and target polarization parallel to negative helicity beam. They have oppositely directed beam polarizations, and hence opposite electroweak asymmetries. However, their deep inelastic spin structure asymmetries have the same sign. When combined to create the DIS spin structure asymmetry, the two configurations' electroweak asymmetries will cancel.

Compared to the asymmetries uncorrected for the electroweak effect, the corrected

E155 asymmetries were $\sim 1\%$ larger in the proton and $\sim 5\%$ larger in the deuteron.

4.6.2 Rate Dependence Corrections

A small correction was made to the 2.75° and 5.5° spectrometer data for rate dependence. The rate dependence was studied and calculated using a method identical to that used in E154 [97, 98]. The method, known as ‘pulse fiction,’ used the experimental raw data to simulate higher-rate data taking. By adding together the raw data hits from successive spills and taking into account detector dead time, the electron reconstruction efficiency at twice the rate (as compared to the actual data) was determined. Extrapolating from this simulated high rate to the experimental rate provided an estimation for the event losses at the experimental rate, as compared to a system with no rate dependence.

These rate dependence corrections were $\sim 1\%$ and the corrected asymmetries were larger than the uncorrected.

4.6.3 Pion/Positron Contamination

The spectrometers were designed to detect high-energy electrons scattered from the polarized target. However, much radiation and many particles are produced in the process of deep inelastic scattering. Some combination of the decay of neutral pions and pair production by real photons produced electron-positron pairs, and the electrons were detected in the spectrometers just like deep-inelastic scattered beam electrons. This pair-symmetric background [99], known as the positron contamination, was measured

by reversing the polarity of the spectrometer magnets and recording the rate of positrons in the detectors. In E155 there was only a small asymmetry in the production of the positron-electron pairs.

The measured ratio of positrons to electrons by x bin is shown in Fig. 4.7. There was a significant rate of pair-symmetric background in the lowest few bins of each spectrometer which, if not corrected for, would have diluted the asymmetry.

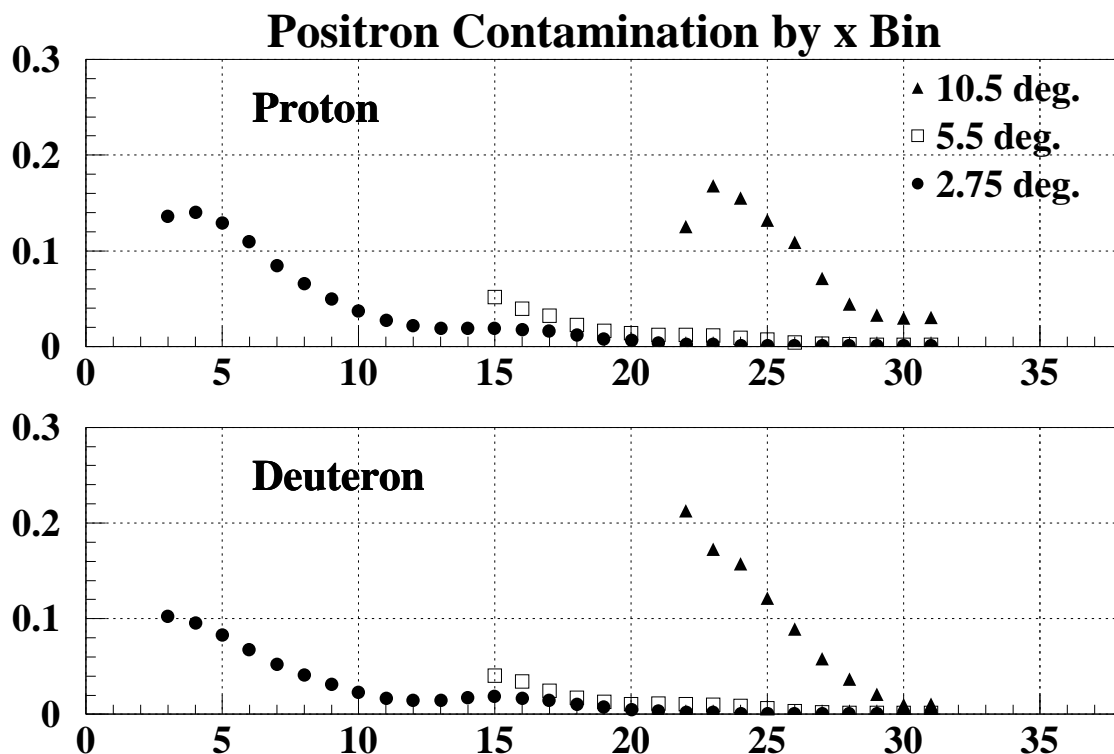


Figure 4.7: The e^+/e^- ratio in the three spectrometers.

The other main component of background was hadron events. These were primarily pions that were produced as part of the fragmentation of the target nucleons struck by the electron beam. Protons and kaons were produced at a rate a factor of ~ 10

smaller than the pion rate [100], hence the hadron contamination of the electron event sample is referred to as pion contamination. The pion contamination of the electron events was an x -dependent quantity, since pions were much more likely to be produced with low momentum. The thresholds of the Cerenkov tanks were selected to be at the momentum where the π^-/e^- ratio was 1. Below these momenta the tanks provided a needed rejection against large pion rates, but setting the threshold higher would have resulted in reduced electron efficiency. Above the Cerenkov threshold the only rejection for hadrons was the E/p ratio. Some small fraction of charged pion events deposited enough energy in the shower counter to pass the E/p cuts that were used. The description immediately following is of an analysis procedure used for the 2.75° and 5.5° spectrometers. The 10.5° spectrometer will be discussed at the end of this section.

The fraction of pion events contaminating the electron event sample was estimated by fitting the E/p spectrum of a pion definition (Class 2 track) and then fitting the E/p spectrum of an electron definition (Class 1 track, Cerenkov signals $\sqrt{C1_{pkV} * C2_{pkV}} > 40$) to a double-Gaussian plus an appropriately normalized component of the fit pion spectrum shape [101]. This is shown in Fig. 4.8 for one representative x bin ($p \approx 14$ GeV) in the 2.75° spectrometer.

The functional form used to fit the pion E/p distribution for the range [0.2,1.8] was, for $y_\pi(x) = (E/p)_{\text{pion}}(x)$:

$$y_\pi(x) = a_1 e^{a_2 x^3 + a_3 x^2 + a_4 x + a_5} . \quad (4.11)$$

This determined the constants a_2 , a_3 , a_4 , and a_5 . Then, with these constants fixed, a new

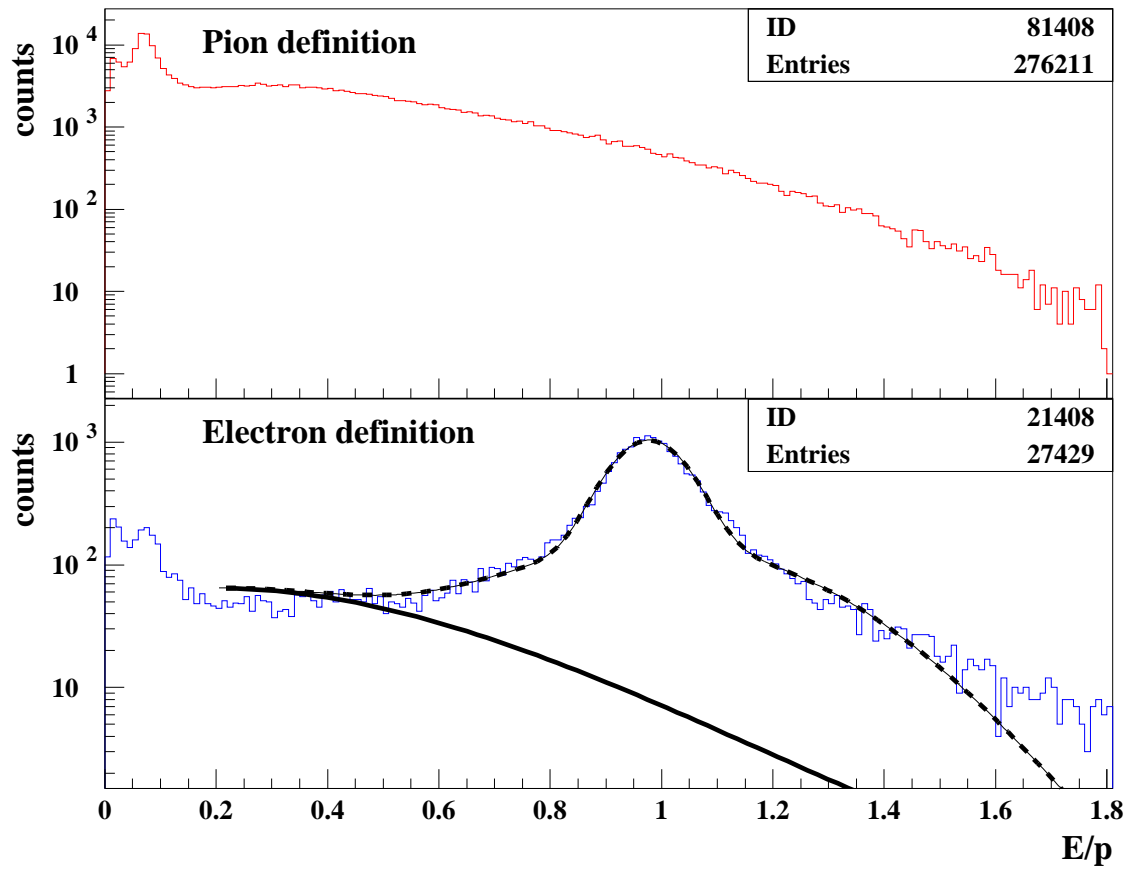


Figure 4.8: E/p ratios for a pion definition and an electron definition for the 8th x bin in the 2.75° spectrometer. The solid curve is a fit to the shape of the pion E/p distribution normalized to the electron definition distribution in the range $[0.2, 0.4]$. The dotted curve is a fit to the electron distribution by a combination of a double-Gaussian and the solid curve.

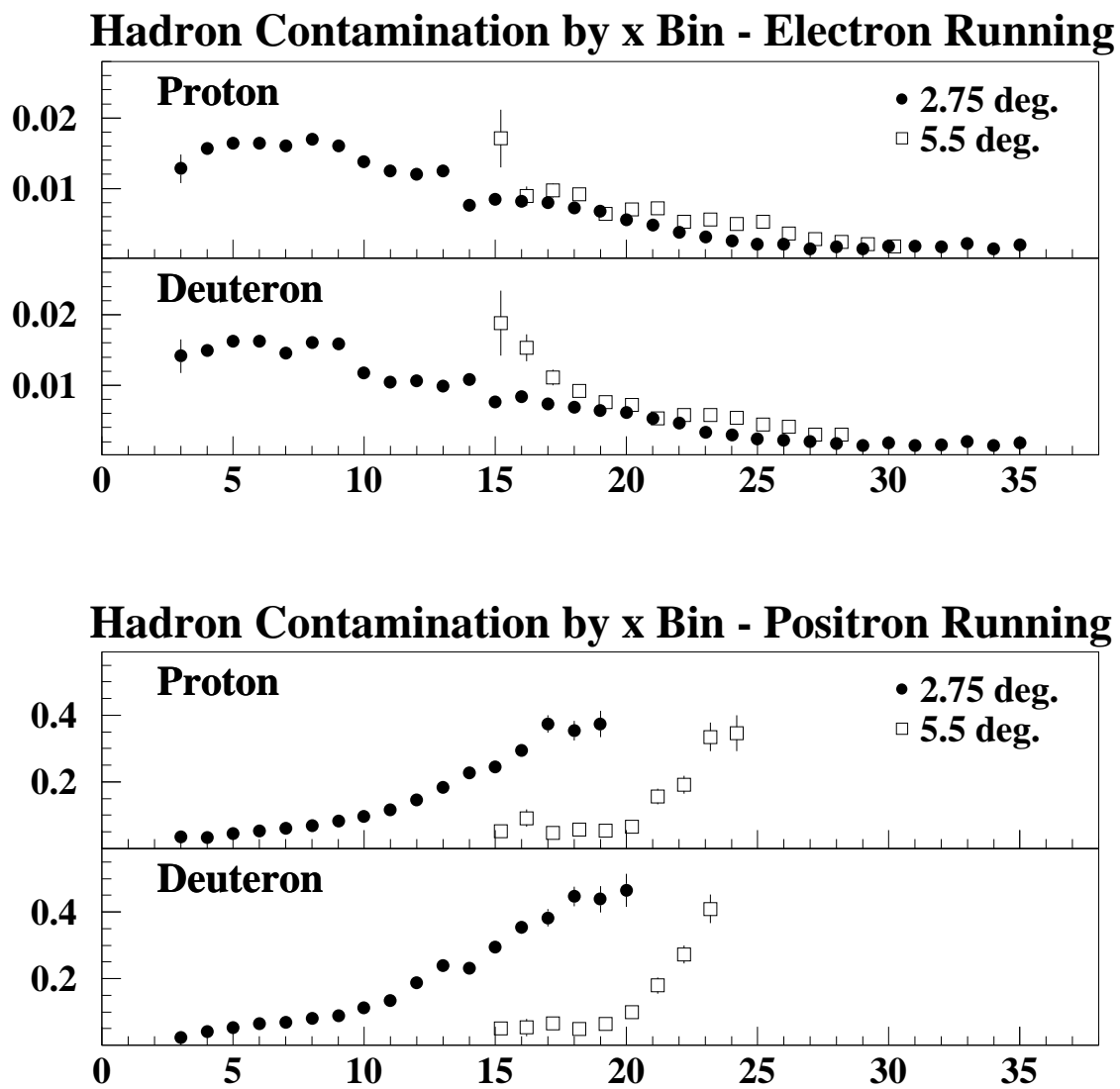
a_1 was found by normalizing the function $y_\pi(x)$ to the E/p distribution for the electron definition over the range [0.2,0.4]. This background function was then used in addition to a double-Gaussian to fit to the electron E/p distribution, $y_{e^-}(x) = (\text{E/p})_{\text{electron}}(x)$, for the range [0.2,1.8]:

$$y_{e^-}(x) = y_\pi(x) + a_{10}e^{-\frac{1}{2}\left(\frac{x-a_{11}}{a_{12}}\right)^2} + a_{13}e^{-\frac{1}{2}\left(\frac{x-a_{14}}{a_{15}}\right)^2}. \quad (4.12)$$

The coefficients a_6 , a_7 , a_8 , and a_9 were reserved for other functional forms.

With increasing x , the pion E/p distributions acquired a small shoulder and eventually a small peak at E/p=1 due to the falling pion rate and higher level of electron contamination of the pion definition. Also, at 19 GeV (x bin 13, at $x=0.044$) and higher in the 2.75° spectrometer, and at 16 GeV (x bin 21, at $x=0.11$) and higher in the 5.5° spectrometer, the pions (but not the kaons and protons) were above Cerenkov threshold. Constraints on the pion E/p shape were used to preserve a pion-like distribution in spite of these effects. Constraints were also used on the two Gaussian components of the electron contribution. All of the constraints used are summarized in Table 4.8.

The fitting procedure was carried out for the four combinations possible for electron/positron data and proton/deuteron target. For each combination a sample of ten runs was selected and the E/p spectra from those runs for the electron and pion definitions were added together by x bin to form the E/p distributions used in the fits. The pion contamination in a particular x bin was determined by calculating the ratio of integrals of the $y_\pi(x)$ function to the $y_{e^-}(x)$ function over the E/p region [0.8,1.2]. The results for the four combinations are shown in Fig. 4.9. There is a slight shoulder

Figure 4.9: The hadron contamination by x bin for both electron and positron running.

parameter	min	max
a_2	1.50	1.90
a_3	-6.00	-5.70
a_4	1.60	2.10
a_5	5.50	6.50
a_{11}	0.90	1.10
a_{12}	0.02	0.09
a_{14}	0.90	1.10
a_{15}	0.10	0.50

Table 4.8: Constraints on the parameters used in calculating pion contamination.

visible in the curve for each spectrometer at the Cerenkov threshold. The pion contamination in the electron runs was less than 2% for all x bins. The pion contamination in the positron runs grows with x since the positron rate falls rapidly with increasing momentum.

Once the positron and pion contaminations were calculated, they were used to adjust the measured asymmetry and obtain the desired, uncontaminated asymmetry A_{e^-} [102]:

$$A_{e^-} = \frac{1}{\alpha_{e^-}} [A_{e^- \text{-measured}} - \frac{\alpha_{e^+}}{1 - \alpha_{\pi^+}} (A_{e^+ \text{-measured}} - \alpha_{\pi^+} A_{\pi^+}) - (\alpha_{\pi^-} A_{\pi^-})]. \quad (4.13)$$

This is based on the relations

$$A_{e^- \text{-measured}} = \alpha_{e^-} A_{e^-} + \alpha_{e^+} A_{e^+} + \alpha_{\pi^-} A_{\pi^-} \quad (4.14)$$

and

$$A_{e^+ \text{-measured}} = (1 - \alpha_{\pi^+}) A_{e^+} + \alpha_{\pi^+} A_{\pi^+}. \quad (4.15)$$

The asymmetries A_{e^-} and A_{e^+} are the true asymmetries for deep inelastic scattering electrons and for electrons produced in pair-symmetric processes. The subscript ‘mea-

sured' indicates an asymmetry measured in the experiment, which was contaminated by hadrons (and the pair-symmetric background for electron runs). The pion asymmetries and positron asymmetry were small and taken to be constant, as given in Table 4.9. These constants were calculated from fits to the asymmetries in the lowest x bins, where the contaminations were most significant.

		Proton	Deuteron
A_{π^-}	2.75°	0.0058	-0.0003
	5.5°	0.0113	0.0035
A_{π^+}	2.75°	0.0106	-0.0007
	5.5°	0.0346	0.0076
A_{e^+}	2.75°	0.0250	-0.0260
	5.5°	-0.1000	-0.1300

Table 4.9: Constant values used for contamination asymmetries.

The α coefficients are used to represent the relative rates per incident beam charge. For an electron run, $\alpha_{e^-} + \alpha_{e^+} + \alpha_{\pi^-} = 1$, which is to say that the number of observed events was the total of the number of true deep inelastic scattering events, the number of pair-symmetric process electron events (the 'positrons'), and the number of hadron background events (the 'pions'). For a positron run, $(1 - \alpha_{\pi^+}) + \alpha_{\pi^+} = 1$ represents the number of positrons (term in parentheses) and the number of positive hadrons that constituted the entire event sample. The α_{e^+} factor was only used in describing electron run rates. These α factors are directly related to the contaminations shown in Figs. 4.7

and 4.9. Equations 4.14 and 4.15 symbolically represent that the measured asymmetries arise from each of these components and their respective asymmetries.

For the 10.5° spectrometer, and for all three spectrometers in perpendicular data taking mode, the contamination asymmetries were all taken to be zero. The coefficients α_{π^-} and α_{π^+} were also taken to be zero. This reduced Eq. 4.13 to a dilution of the deep inelastic events by pair-symmetric backgrounds only. The 10.5° spectrometer did not have enough redundancy to make a useful pion definition, so the contamination of hadrons in the electron data was approximated by using the uncorrected (for hadron contamination) positron data as a combined correction for both pair-symmetric backgrounds and hadrons.

4.6.4 Resolution Corrections

Using the optics model of the spectrometers, and a parameterized fit to world spin structure function data as a model for the asymmetry, the effects of detector momentum and angle resolution were estimated [103]. A multiplicative correction, shown in Fig. 4.10 was applied to the measured asymmetry. The correction shown was applied to the proton target data, and a similar correction (differing slightly due to model asymmetry values) was applied to the deuteron data.

4.6.5 Radiative Corrections

The spin structure functions g_1 and g_2 parameterize the spin-dependent part of the lowest-order, single-photon exchange Born-level process shown in Fig. 2.1. The exper-

Resolution Corrections: True Asymmetry/Measured

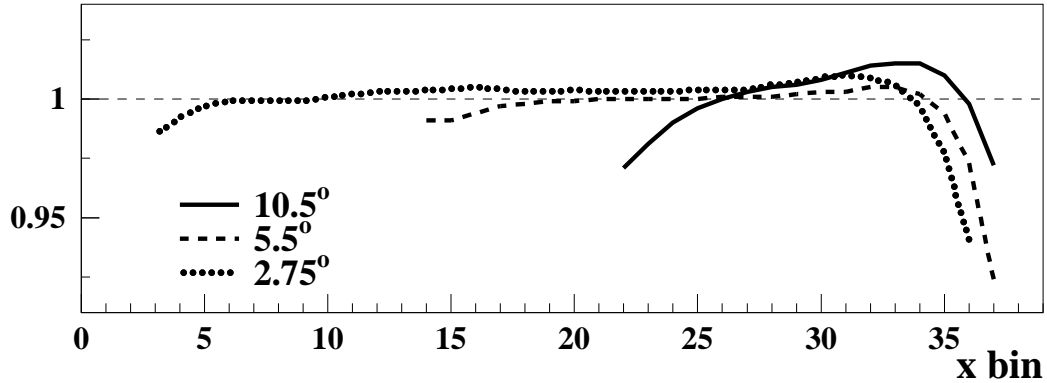


Figure 4.10: Resolution corrections to the parallel asymmetry, by spectrometer.

imental cross-sections and asymmetries, however, contain contributions from higher-order processes, such as those shown in Fig. 4.11.

These processes, accounted for by radiative corrections, are broken into two classes: internal and external. Internal are those which occur within the field of the scattering nucleus. Internal processes, calculated to order α^3 , include bremsstrahlung, vertex corrections, vacuum polarization, and also quasi-elastic and elastic scattering contributions. External corrections [104, 105] correct for losses due to bremsstrahlung both before and after the scattering process. The polarized corrections were calculated using computer code (RCSLACPOL, developed at SLAC) based on Ref. [106].

The first-order Born approximation makes the assumption of single photon exchange in the interaction. Two-photon exchange, though of the same order as (b.) and (d.) in Fig. 4.11 (and which would contribute as an interference term at the α^3 level), is not fully included in the radiative corrections. Multiple photon exchange is included in the

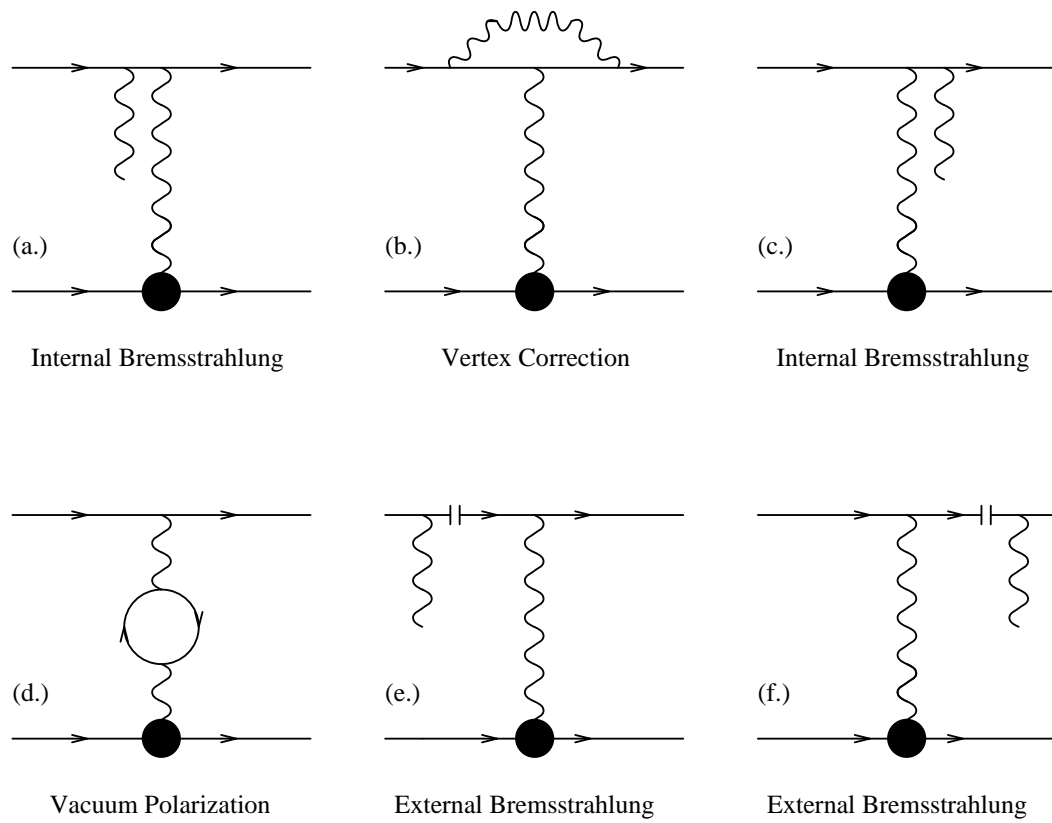


Figure 4.11: Feynman diagrams for internal and external processes considered in radiative corrections.

limit that all but one of the photons are soft, and it must be included to cancel infrared divergences arising from other diagrams. The full two-photon exchange calculation is difficult since it requires accounting for all of the intermediate hadron and electron states between the two photon vertices.

The radiative corrections [107] were large at the lowest x of each spectrometer, up to 30% in the lowest few bins for the proton, and smaller for the deuteron. At low x the corrections made the proton parallel asymmetry values more positive. For both targets they were broken into two parts, a radiative dilution factor (f_{RC}) and an additive correction (A_{RC}). The radiative dilution factor, the unpolarized radiative corrections, accounts for the fraction of the events in each bin that was radiated down from Born-level processes in higher x bins. The additive correction, the polarized radiative corrections, adjusts the asymmetry in each bin for the effect of the events from higher x on that bin's asymmetry. Thus the f_{RC} changes the effective number of events in a bin, and the A_{RC} changes the effective asymmetry, with these changes made to reflect the Born-level process rather than the radiated processes observed in the experiment.

4.7 A_{\parallel} and A_{\perp} Asymmetries

The asymmetries A_{\parallel} for proton and deuteron targets are shown by spectrometer in Fig. 4.12. Similarly, asymmetries A_{\perp} for proton and deuteron targets are shown by spectrometer in Fig. 4.13. The data are presented in the fine binning, defined as 38 bins spaced equally (in $\ln x$) over $[0.01, 0.90]$. In the parallel data, for all three spectrometers,

both targets exhibited a significant positive asymmetry. The perpendicular data is largely consistent with zero.

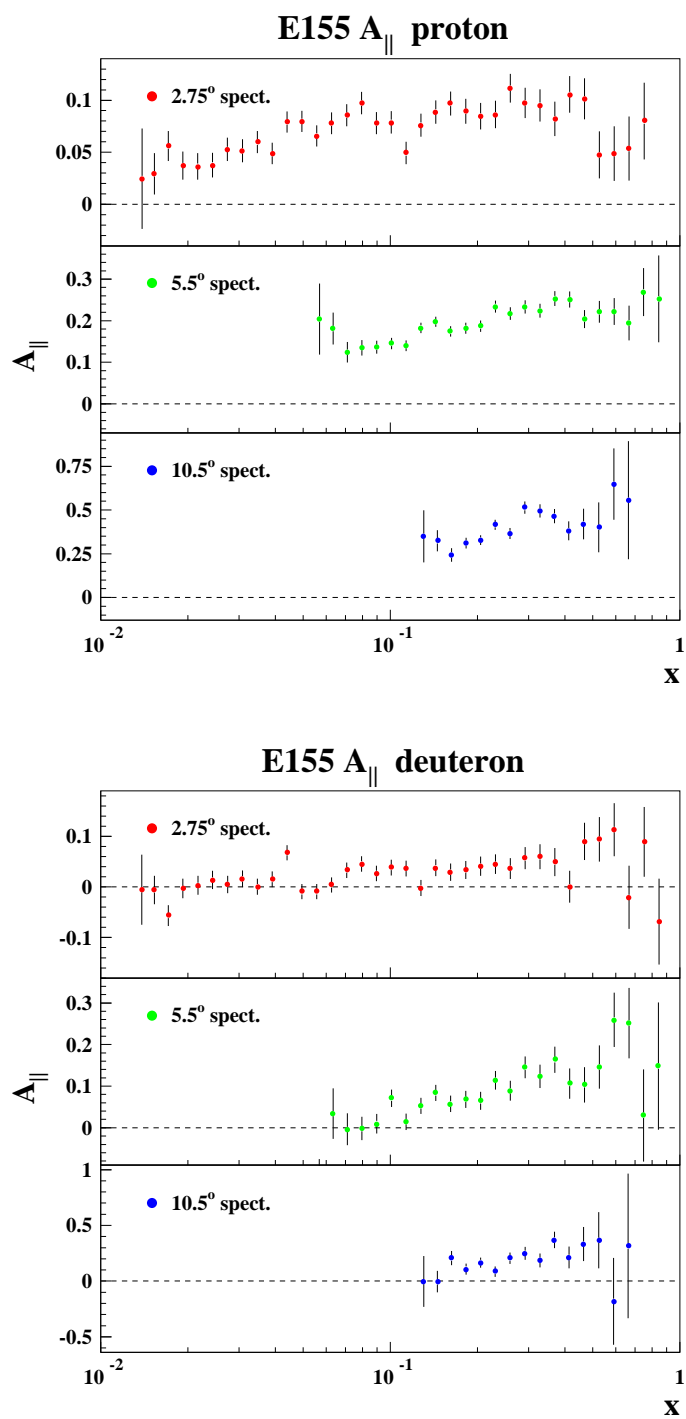
Tables of the A_{\parallel} and A_{\perp} results are given in Appendix C.

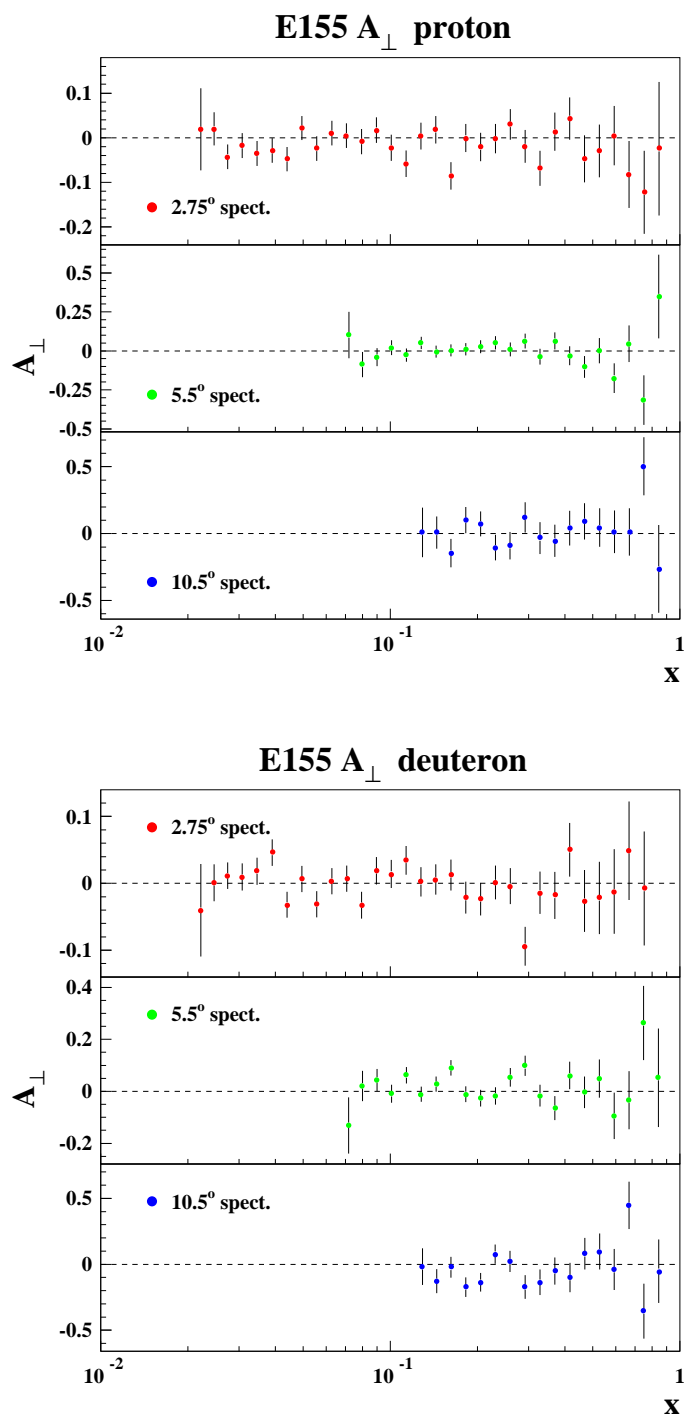
4.8 Systematic Errors

The systematic errors used in this thesis for A_{\parallel} are given as approximate scale percentages in Table 4.10. Over all x the largest errors are from the target polarization, dilution factor, and beam polarization. These are factors which directly scale the asymmetries. The significant x dependence of the radiative corrections uncertainty is neglected in this table. The radiative corrections errors listed are the contributions to the systematic error on the measured region integral values, which roughly translate to errors on the asymmetries. Further discussion on systematic errors and a breakdown of the systematic errors as functions of x for the spin structure function g_1 are given in Appendix D. The perpendicular target orientation data was a small subset of the overall E155 data, and as a consequence the measurements of A_{\perp} and g_2 are statistics limited.

	proton	deuteron
P_{beam}	2.5%	2.5%
P_{target}	6.	4.
D-in-Li extraction		2.7
dilution factor	2.5	2.9
e^+/π contamination	1.	1.
radiative corrections	1.5	4.
total	7.2%	7.4%

Table 4.10: Approximate asymmetry systematic errors as relative uncertainties.

Figure 4.12: Proton and deuteron A_{\parallel} for E155.

Figure 4.13: Proton and deuteron A_{\perp} for E155.

Chapter 5

Results

5.1 The Structure Function $g_1(x, Q^2)$

The asymmetries of the preceding chapter were combined to yield the structure function g_1 and the ratio g_1/F_1 for each bin in the measured kinematic region. Since the A_\perp data in E155 was obtained at a different beam energy, the function $g_1(x, Q^2)$ was determined from the A_\parallel data only:

$$g_1 = \frac{A_\parallel F_1}{D'} \left[\frac{E_0 + E'}{E_0 + E' \cos(\theta)} \right] + g_2 \left[\frac{2Mx}{E_0 + E' \cos(\theta)} \right]. \quad (5.1)$$

In the above equation, g_2 is taken to be a leading twist-2 theoretical prediction, g_2^{WW} [108], an assumption consistent with existing data (including the A_\perp data from E155 [109]).

This prediction for g_2 relates it to g_1 by:

$$g_2^{WW}(x, Q^2) = -g_1(x, Q^2) + \int_x^1 \frac{g_1(y, Q^2)}{y} dy. \quad (5.2)$$

The data from the three spectrometers were combined and evolved to $Q^2=5 \text{ GeV}^2$, using a process described below. Data from other experiments were similarly combined and evolved, allowing g_1 to be plotted as a function of x , as in Fig. 5.1. It is also interesting to plot xg_1 as a function of x , as in Fig. 5.2, since the log scale distorts the relative contribution of each bin to the integral $\int_0^1 g_1 dx$. The third plot in each figure includes the extracted neutron result for E155, obtained from rebinned proton and

deuteron results and Eq. 2.6. These plots compare experiments which utilized a variety of beams, targets, and detector systems. There is a remarkable consistency between the many experiments. The SMC data reach to lower x than any other experiment, but the E155 data are much more precise down to $x=0.015$.

A fit to world data, including E155, was made using the functional form:

$$g_1/F_1 = x^\alpha(a + bx + cx^2)(1 + \beta/Q^2) \quad (5.3)$$

where separate coefficients were used to fit the proton and neutron data, and the deuteron data were included using Eq. 2.6. The coefficients of the fit are given in Table 5.1. This fit was a result of the radiative corrections process—calculating the radiative corrections required input parameterizations for many quantities, including the Born asymmetries measured in this experiment. This necessarily iterative process converged after very few iterations. The model for the asymmetries was provided in this fit form and these coefficients are the result of the converged process. The fit has a total χ^2 of 493 for 493 degrees of freedom.

coefficient	proton	neutron
α	0.615	-0.082
a	0.715	-0.056
b	1.331	-0.319
c	-1.766	0.830
β	-0.165	-0.138

Table 5.1: Coefficients for proton and neutron functional fits to world data on the proton, neutron, and deuteron.

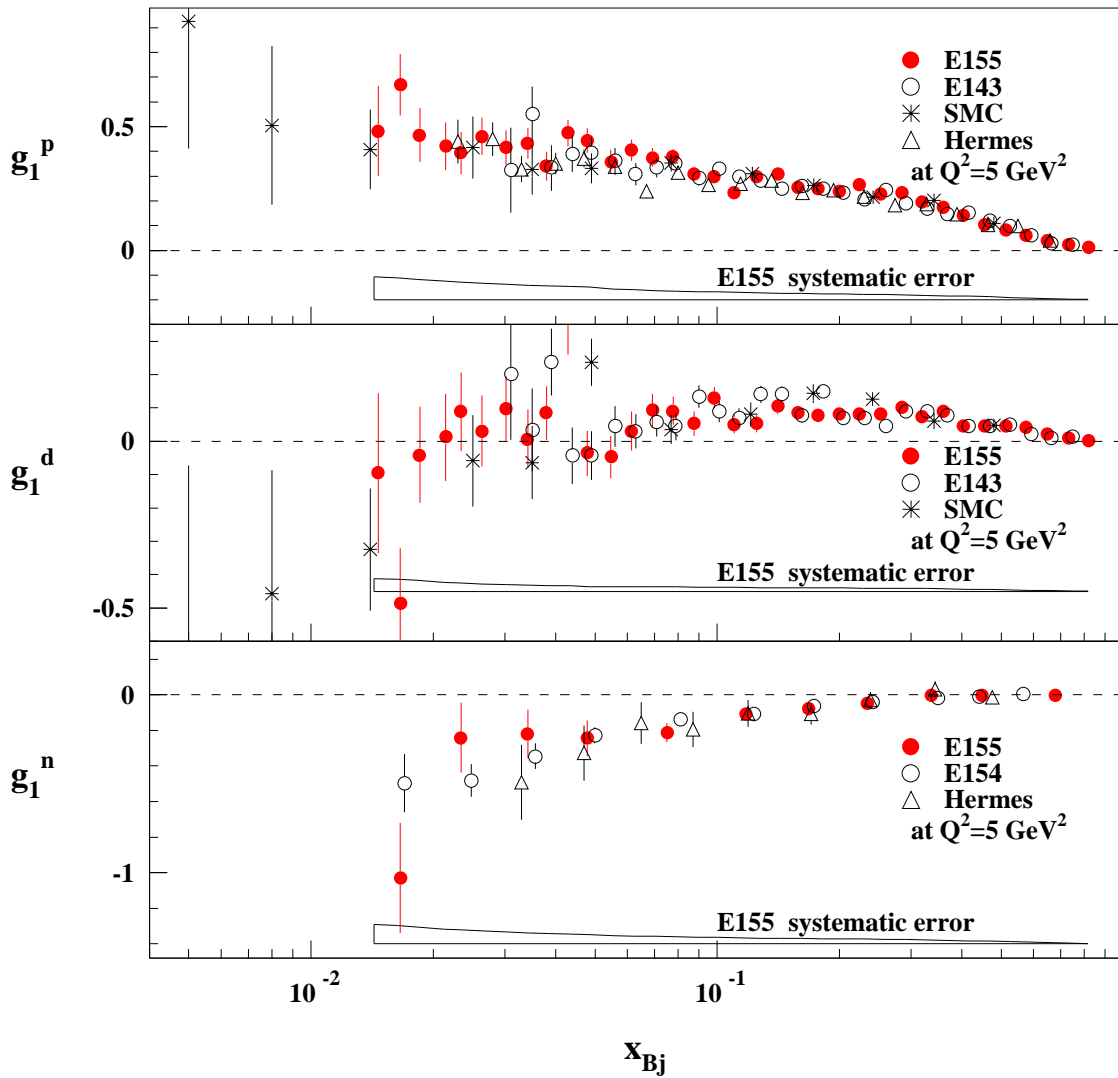


Figure 5.1: Results for g_1^p , g_1^d , g_1^n : E155 vs. other experiments. The data have all been evolved to $Q^2 = 5 \text{ GeV}^2$.

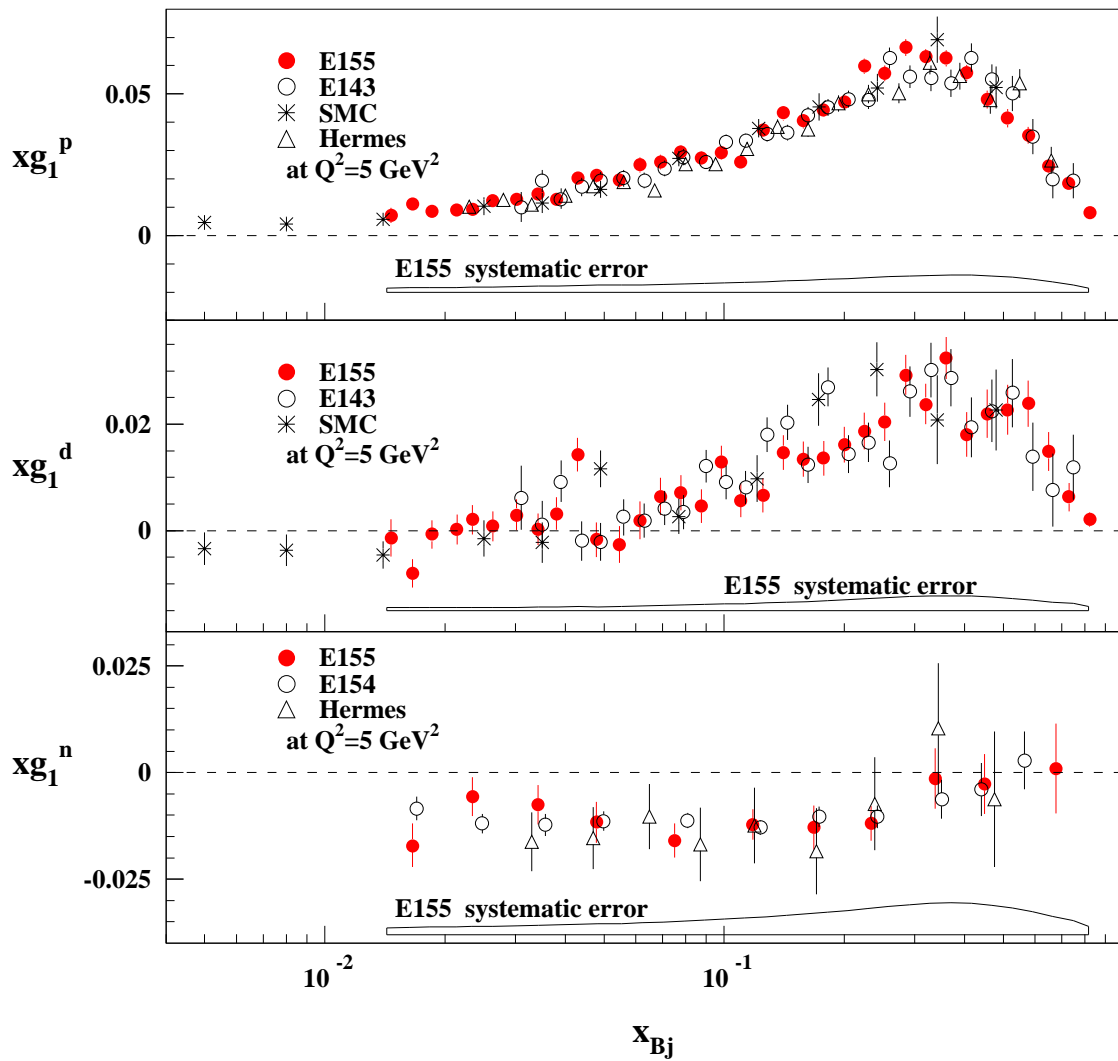


Figure 5.2: Results for xg_1^p , xg_1^d , xg_1^n : E155 vs. other experiments. The data have all been evolved to $Q^2 = 5 \text{ GeV}^2$.

Once $g_1(x, Q^2)/F_1(x, Q^2)$ was calculated, the data were rebinned into a set of coarse bins, also known as world binning, listed in Table 5.2. This rebinning was accomplished

bin	min x	max x
1	0.010	0.020
2	0.020	0.030
3	0.030	0.040
4	0.040	0.060
5	0.060	0.100
6	0.100	0.150
7	0.150	0.200
8	0.200	0.300
9	0.300	0.400
10	0.400	0.600
11	0.600	0.900

Table 5.2: Bin edges for coarse world binning.

by combining into each coarse bin the fine bins whose $\langle x \rangle$ fell within its limits. The $\langle x \rangle$, $\langle Q^2 \rangle$, and g_1/F_1 of the selected fine bins were averaged, each weighted by its statistical error on g_1/F_1 . This is correct assuming that g_1/F_1 is a constant within the coarse bin, a valid assumption given the precision of the data. The bins were recentered using differences between fit values of Eq. 5.3 for the weighted average $\langle x \rangle$ and the center of the bin. Tables 5.3 and 5.4 give the E155 results for g_1 and g_1/F_1 by spectrometer for the coarse world binning.

	$\langle x \rangle$	$\langle Q^2 \rangle$	$g_1/F_1 \pm \text{stat} \pm \text{syst}$	$g_1 \pm \text{stat} \pm \text{syst}$
2.75°	0.015	1.22	0.050 ± 0.011 ± 0.004	0.369 ± 0.084 ± 0.036
	0.025	1.59	0.061 ± 0.010 ± 0.006	0.298 ± 0.048 ± 0.030
	0.035	2.05	0.083 ± 0.010 ± 0.007	0.313 ± 0.036 ± 0.027
	0.050	2.57	0.132 ± 0.010 ± 0.009	0.371 ± 0.029 ± 0.025
	0.080	3.24	0.184 ± 0.011 ± 0.013	0.341 ± 0.021 ± 0.023
	0.125	4.03	0.201 ± 0.015 ± 0.017	0.247 ± 0.018 ± 0.021
	0.175	4.62	0.315 ± 0.028 ± 0.022	0.278 ± 0.024 ± 0.019
	0.250	5.06	0.403 ± 0.028 ± 0.029	0.236 ± 0.016 ± 0.017
	0.350	5.51	0.486 ± 0.060 ± 0.036	0.172 ± 0.021 ± 0.013
	0.500	5.77	0.585 ± 0.069 ± 0.044	0.092 ± 0.011 ± 0.007
5.5°	0.050	4.01	0.237 ± 0.104 ± 0.009	0.735 ± 0.323 ± 0.031
	0.080	5.36	0.172 ± 0.013 ± 0.013	0.346 ± 0.026 ± 0.026
	0.125	7.17	0.236 ± 0.009 ± 0.017	0.309 ± 0.012 ± 0.023
	0.175	8.90	0.279 ± 0.014 ± 0.022	0.255 ± 0.013 ± 0.021
	0.250	10.64	0.396 ± 0.013 ± 0.029	0.231 ± 0.007 ± 0.017
	0.350	12.60	0.516 ± 0.025 ± 0.037	0.171 ± 0.008 ± 0.012
	0.500	14.02	0.608 ± 0.028 ± 0.045	0.078 ± 0.004 ± 0.006
	0.750	15.70	0.701 ± 0.108 ± 0.045	0.010 ± 0.002 ± 0.001
10.5°	0.125	10.99	0.329 ± 0.060 ± 0.018	0.445 ± 0.081 ± 0.026
	0.175	13.18	0.309 ± 0.026 ± 0.022	0.286 ± 0.024 ± 0.022
	0.250	17.19	0.451 ± 0.016 ± 0.029	0.261 ± 0.009 ± 0.017
	0.350	22.73	0.567 ± 0.030 ± 0.036	0.178 ± 0.010 ± 0.012
	0.500	26.88	0.529 ± 0.050 ± 0.045	0.060 ± 0.006 ± 0.005
	0.750	34.73	0.742 ± 0.468 ± 0.045	0.008 ± 0.005 ± 0.001

Table 5.3: E155 proton results for g_1/F_1 and g_1 .

	$\langle x \rangle$	$\langle Q^2 \rangle$	$g_1/F_1 \pm \text{stat} \pm \text{syst}$	$g_1 \pm \text{stat} \pm \text{syst}$
2.75°	0.015	1.22	-0.033 ± 0.016 ± 0.001	-0.234 ± 0.115 ± 0.011
	0.025	1.59	0.011 ± 0.014 ± 0.001	0.051 ± 0.068 ± 0.006
	0.035	2.05	0.016 ± 0.014 ± 0.001	0.059 ± 0.052 ± 0.005
	0.050	2.57	0.030 ± 0.015 ± 0.002	0.082 ± 0.041 ± 0.004
	0.080	3.24	0.059 ± 0.016 ± 0.003	0.103 ± 0.028 ± 0.005
	0.125	4.03	0.079 ± 0.021 ± 0.005	0.089 ± 0.024 ± 0.006
	0.175	4.62	0.107 ± 0.041 ± 0.008	0.083 ± 0.032 ± 0.006
	0.250	5.06	0.192 ± 0.042 ± 0.012	0.096 ± 0.021 ± 0.006
	0.350	5.51	0.301 ± 0.098 ± 0.017	0.086 ± 0.028 ± 0.005
	0.500	5.77	0.389 ± 0.129 ± 0.024	0.047 ± 0.016 ± 0.003
5.5°	0.050	4.00	-0.266 ± 0.170 ± 0.002	-0.787 ± 0.504 ± 0.006
	0.080	5.37	0.006 ± 0.020 ± 0.003	0.012 ± 0.038 ± 0.006
	0.125	7.16	0.079 ± 0.014 ± 0.005	0.094 ± 0.016 ± 0.006
	0.175	8.90	0.099 ± 0.022 ± 0.008	0.080 ± 0.018 ± 0.006
	0.250	10.62	0.184 ± 0.020 ± 0.012	0.090 ± 0.010 ± 0.006
	0.350	12.59	0.305 ± 0.044 ± 0.017	0.081 ± 0.012 ± 0.005
	0.500	14.01	0.349 ± 0.057 ± 0.025	0.034 ± 0.006 ± 0.002
	0.750	15.73	0.576 ± 0.220 ± 0.029	0.006 ± 0.002 ± 0.001
10.5°	0.125	10.98	-0.020 ± 0.095 ± 0.006	-0.025 ± 0.117 ± 0.008
	0.175	13.19	0.157 ± 0.042 ± 0.008	0.127 ± 0.034 ± 0.007
	0.250	17.22	0.194 ± 0.027 ± 0.012	0.094 ± 0.013 ± 0.006
	0.350	22.65	0.309 ± 0.053 ± 0.017	0.077 ± 0.013 ± 0.005
	0.500	26.97	0.330 ± 0.092 ± 0.024	0.028 ± 0.008 ± 0.002
	0.750	34.79	0.428 ± 0.903 ± 0.028	0.003 ± 0.007 ± 0.001

Table 5.4: E155 deuteron results for g_1/F_1 and g_1 .

5.2 Q^2 dependence

The world data on g_1^p exhibit a clear Q^2 dependence, as shown in Fig. 5.3. The scaling violation is similar in character to that of Fig. 2.2. At low x , the structure function increases with Q^2 , and at high x it decreases with increasing Q^2 .

There is only a small dependence on Q^2 for the ratio g_1/F_1 . This is not surprising since the polarized and unpolarized structure functions evolve in Q^2 according to similar DGLAP equations. In Fig. 5.4 and 5.5 the mostly flat behavior of the ratio for both the proton and the deuteron is evident.

With the addition of the 10.5° spectrometer, the kinematic coverage available to ESA with the upgraded A-line is sufficient to fill the gap between the electron experiments at SLAC and DESY and the muon experiments at CERN.

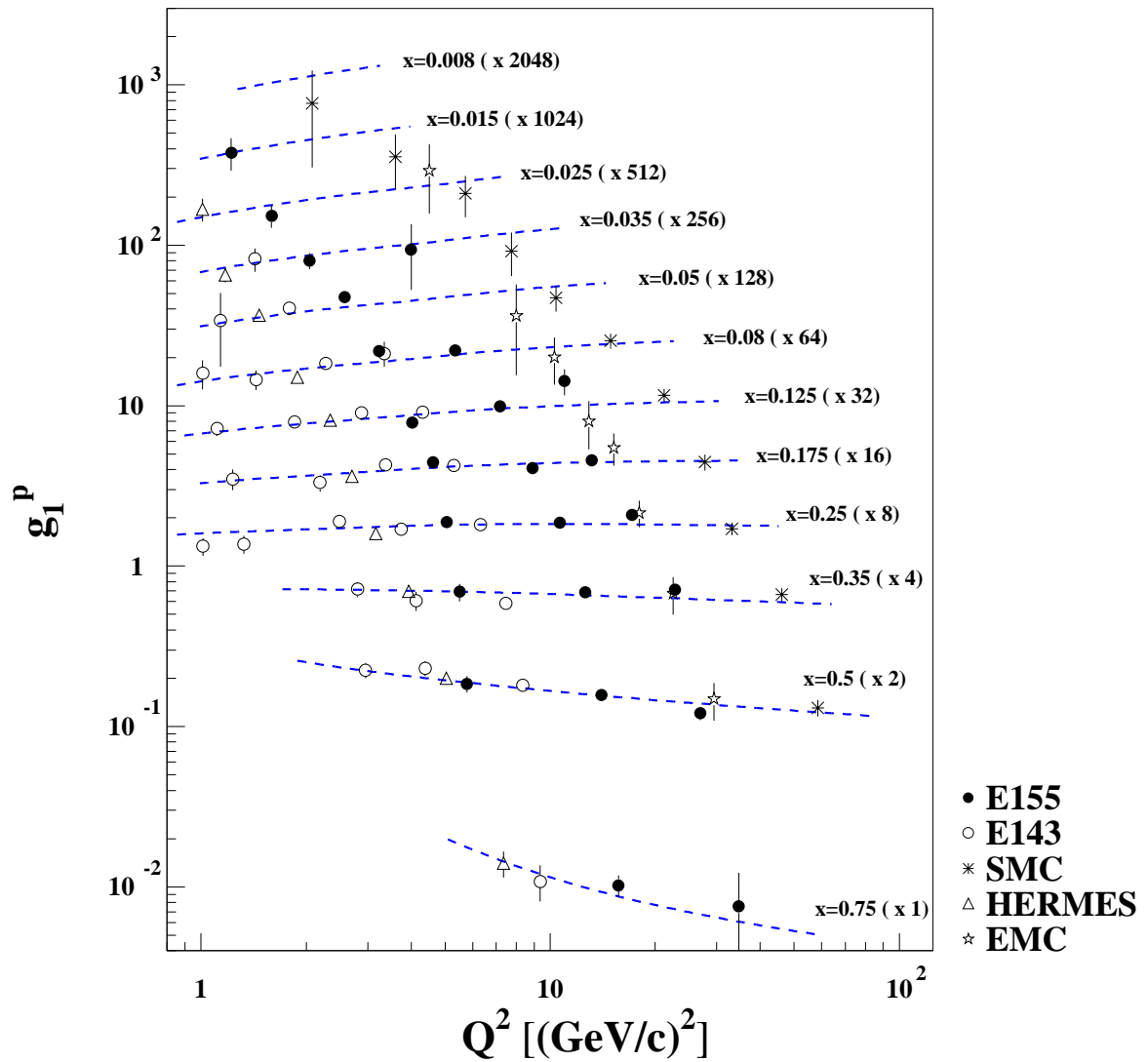


Figure 5.3: g_1^p for E155 and other experiments vs. Q^2 . The dashed curves are the proton fit from Eq. 5.3. The points and curves have been multiplied by the factors in parentheses for clarity.

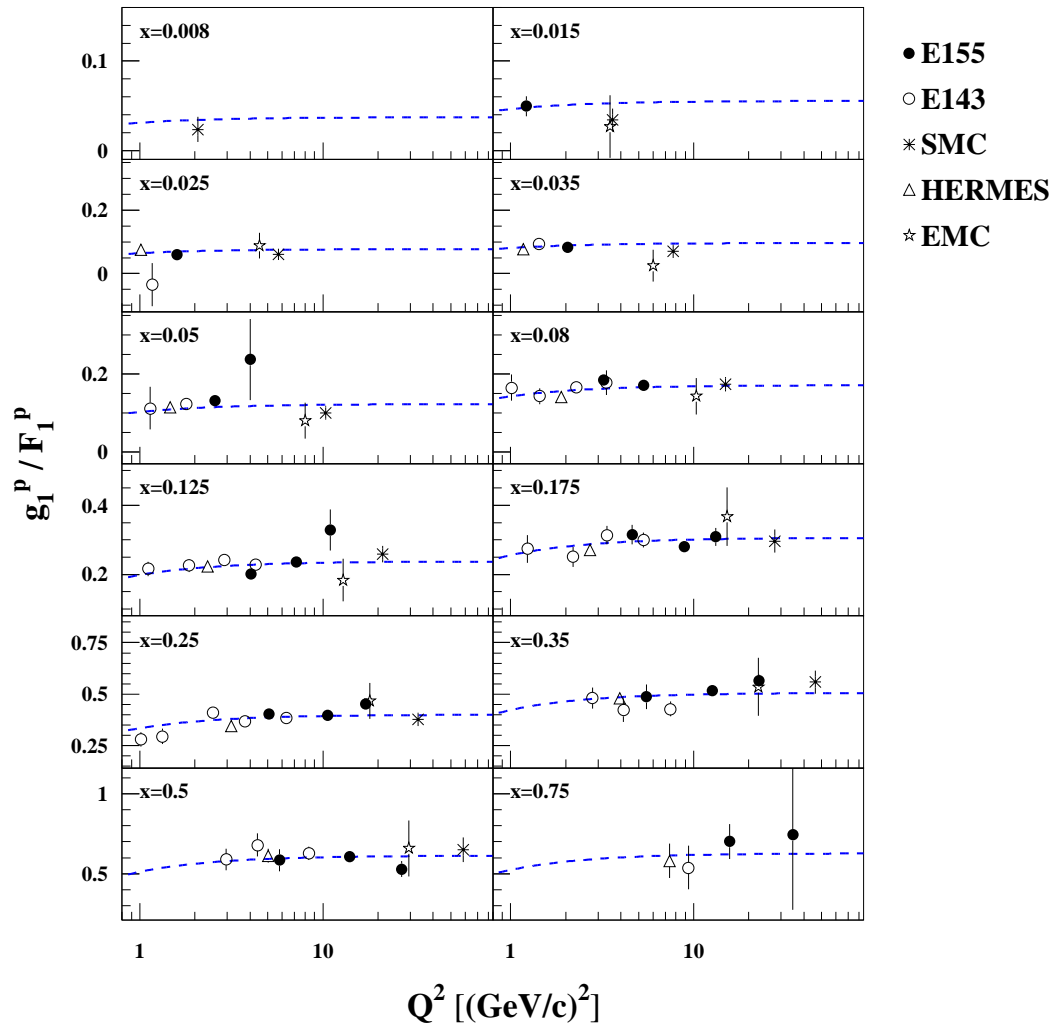


Figure 5.4: g_1^p / F_1^p for E155 vs. other experiments. The multiple points in each bin for E155 are for the separate spectrometers. The dashed curves are the proton fit from Eq. 5.3.

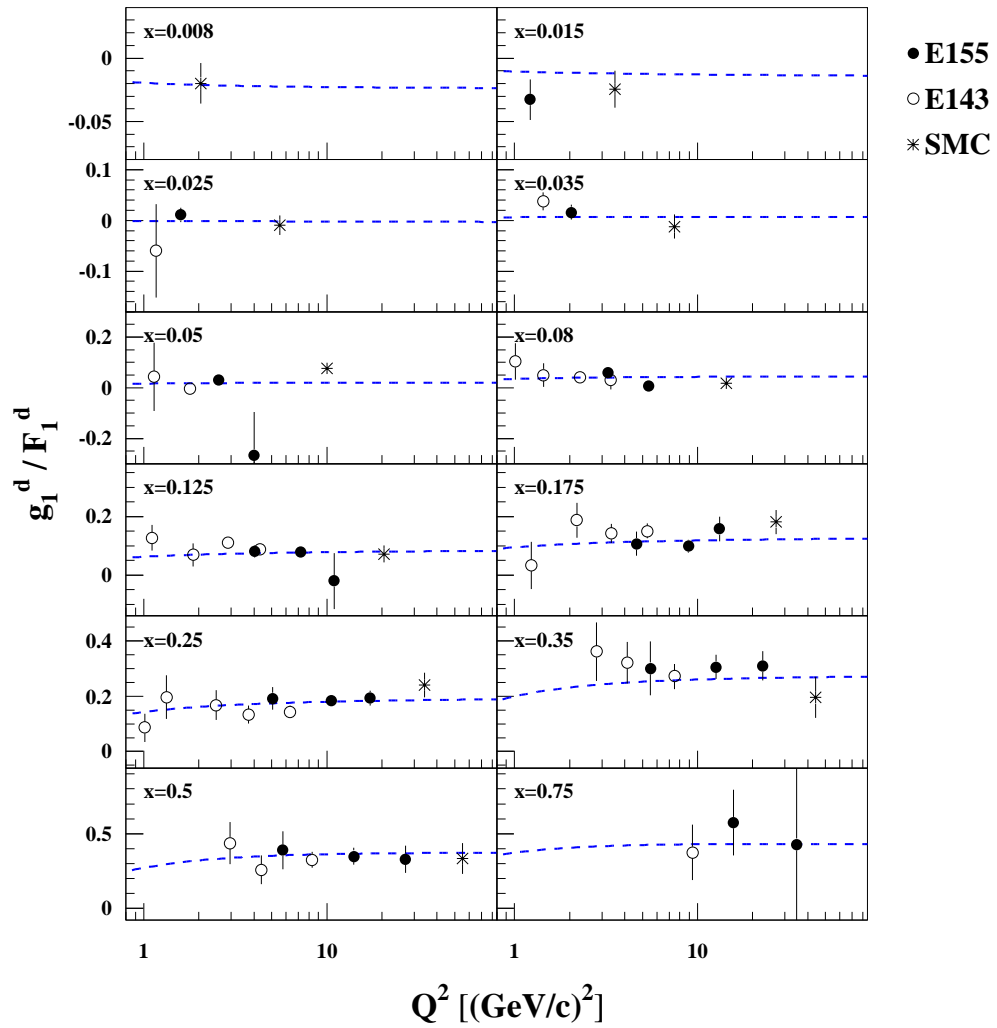


Figure 5.5: g_1^d / F_1^d for E155 vs. other experiments. The multiple points in each bin for E155 are for the separate spectrometers. The dashed curves are the deuteron fit from Eq. 5.3.

For testing sum rules, which make predictions for the structure function integrals at constant Q^2 , the data are evolved to some common Q^2 . For E155, $Q^2 = 5 \text{ GeV}^2$ is chosen as a compromise between the midpoint of the experimental range ($1 \text{ GeV}^2 < Q^2 < 40 \text{ GeV}^2$) and the low Q^2 of most of the events (the average Q^2 weighted by events is $\sim 3.5 \text{ GeV}^2$). Since there is little Q^2 dependence to the ratio g_1/F_1 , one method of evolution used by recent experiments has been to assume the ratio is a constant:

$$g_1(x, Q_c^2) = \left(\frac{g_1(x, Q^2)}{F_1(x, Q^2)} \right) F_1(x, Q_c^2) \quad (5.4)$$

where Q^2 represents the experimental value and the c subscript represents the common $Q_c^2 = 5 \text{ GeV}^2$.

Another method, which was used in this analysis, is to add (or subtract) to the measured $g_1(x, Q^2)$ according to the Q^2 dependence of the fit of Eq. 5.3:

$$\left(\frac{g_1(x, Q_c^2)}{F_1(x, Q_c^2)} \right) = \left(\frac{g_1(x, Q^2)}{F_1(x, Q^2)} \right) + \left[\left(\frac{g_1(x, Q_c^2)}{F_1(x, Q_c^2)} \right)_{fit} - \left(\frac{g_1(x, Q^2)}{F_1(x, Q^2)} \right)_{fit} \right]. \quad (5.5)$$

5.3 Measured Region Integrals

The kinematic region measured by E155 was $0.014 < x < 0.9$ and $1 < Q^2 < 40 \text{ GeV}^2$. If the three spectrometers' data are combined for each target and evolved to $Q^2 = 5 \text{ GeV}^2$, the following integrals are obtained:

$$\int_{0.014}^{0.9} g_1^p dx = 0.131 \pm 0.002 \pm 0.010 \quad (5.6)$$

$$\int_{0.014}^{0.9} g_1^d dx = 0.043 \pm 0.003 \pm 0.003 \quad (5.7)$$

$$\int_{0.014}^{0.9} g_1^n dx = -0.040 \pm 0.005 \pm 0.012 \quad (5.8)$$

including the extracted neutron result.

5.4 Extrapolation and Sum Rules

Testing the predictions of sum rules requires converting the experimental structure function results to integrals from Bjorken $x=0$ to $x=1$ at a fixed Q^2 . To obtain experimental numbers at fixed Q^2 for $\Gamma_1^p = \int_0^1 g_1^p(x, Q^2) dx$ and $\Gamma_1^d = \int_0^1 g_1^d(x, Q^2) dx$, the data must first be evolved from their measured Q^2 to the fixed Q^2 , and then extrapolations calculated for the unmeasured low x and high x kinematic regions.

Based on the E154 next-to-leading order pQCD fit [11, 110] (which included world data prior to E155) contributions at $Q^2 = 5 \text{ GeV}^2$ can be estimated for the unmeasured low x region, $[0,0.014]$:

$$\int_0^{0.014} g_1^p dx = -0.006 \pm 0.004 \pm 0.002 \pm 0.009 \quad (5.9)$$

$$\int_0^{0.014} g_1^d dx = -0.014 \pm 0.004 \pm 0.002 \pm 0.005 \quad (5.10)$$

and the contributions from $[0.9,1.0]$ are negligible. The three error terms are for statistical, systematic, and theoretical/evolution errors, respectively. A comparison of the low x E155 data to the E154 fit is shown in Fig. 5.6. The deuteron data agree well with the fit, while the proton data are larger by a factor of $1.5 \approx 0.45/0.30$. A normalization factor of up to 2.0 for the proton contribution would not take it outside the given evolution error of 0.009, so the low x contribution is taken simply as given above.

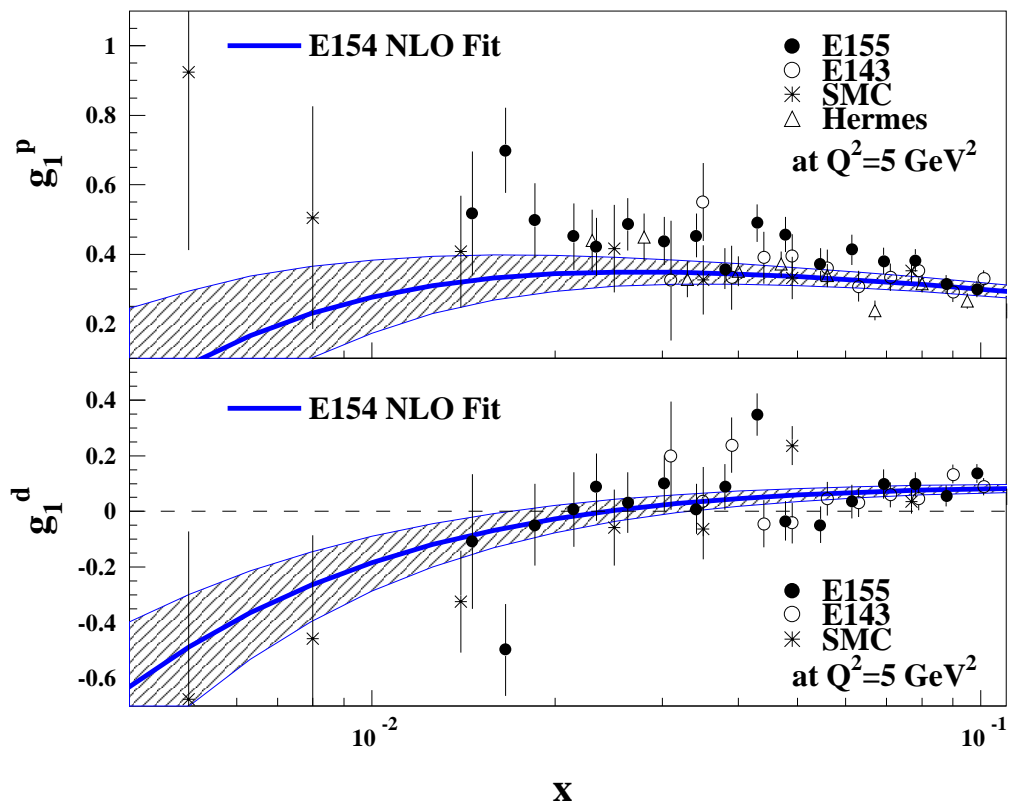


Figure 5.6: Low x E155 results compared to E154 NLO fit.

Combining the low x E154 fit contributions with the above E155 measured region results yields:

$$\Gamma_1^p = \int_0^1 g_1^p dx = 0.125 \pm 0.005 \pm 0.010 \pm 0.009, \quad (5.11)$$

$$\Gamma_1^d = \int_0^1 g_1^d dx = 0.029 \pm 0.005 \pm 0.004 \pm 0.005. \quad (5.12)$$

Since these integrals are at a constant $Q^2 = 5 \text{ GeV}^2$, they can be combined to find an E155 result for the Bjorken sum rule:

$$\Gamma_1^{p-n} = \int_0^1 [g_1^p - g_1^n] dx = \int_0^1 \left[g_1^p - \left(g_1^d \frac{2}{1 - 1.5\omega_D} - g_1^p \right) \right] dx \quad (5.13)$$

$$= 0.187 \pm 0.011 \pm 0.020 \pm 0.020 \quad (5.14)$$

which is consistent with the theoretical value of 0.182 ± 0.005 . These results can be seen in a common pictorial format in Fig. 5.7. For comparison, the final SMC results are [13]:

$$(\Gamma_1^p)_{\text{SMC}} = \int_0^1 g_1^p dx = 0.120 \pm 0.005 \pm 0.006 \pm 0.014, \quad (5.15)$$

$$(\Gamma_1^d)_{\text{SMC}} = \int_0^1 g_1^d dx = 0.019 \pm 0.006 \pm 0.003 \pm 0.013. \quad (5.16)$$

Due to the higher SMC beam energy, these values are for a higher constant average $Q^2 = 10 \text{ GeV}^2$. Both Γ_1^p and Γ_1^d decrease with increasing Q^2 , so the evolution of the SLAC data to the average Q^2 of the SMC data results in both the proton and deuteron integrals for SMC and E155 being consistent at the $1\text{-}\sigma$ level.

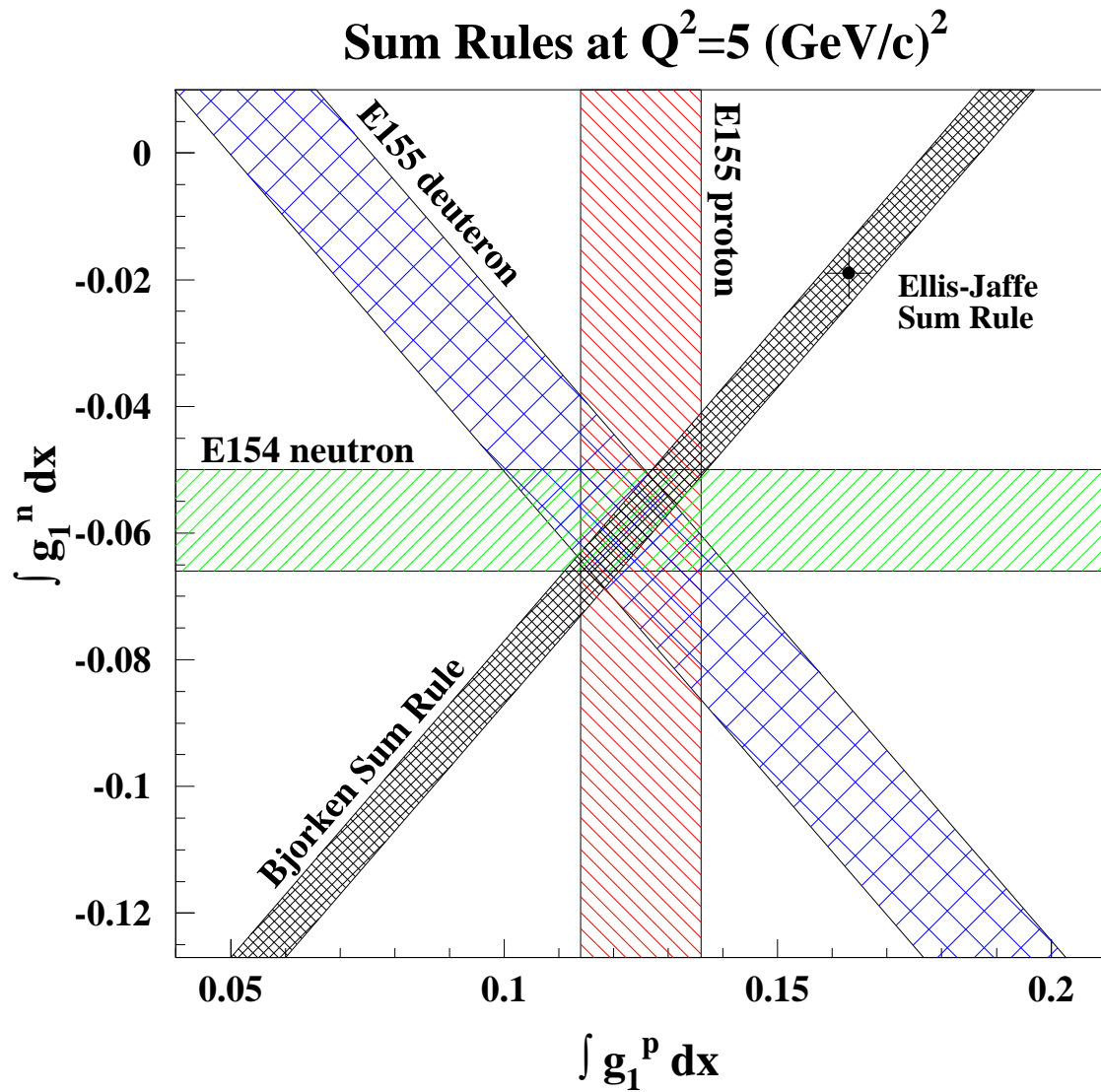


Figure 5.7: E155 Results for Γ_1^p and Γ_1^d compared to sum rules. Also shown is the E154 result for Γ_1^n . The data are at the common $Q^2 = 5 \text{ GeV}^2$, and the widths of the bands represent $\pm 1\sigma$ total errors on each value. The Bjorken sum rule is confirmed, while the Ellis-Jaffe sum rule is violated.

5.5 NLO fitting

5.5.1 Method

As a brief description, fitting the data in a next-to-leading order (NLO) perturbative quantum chromodynamics (pQCD) scheme is done as follows. This method is identical to that of E154 [11] and closely follows that of Refs. [111, 112]. The process starts with low Q^2 polarized parton distributions

$$\Delta q_i(x, Q_0^2) = A_i x^{\alpha_i} q_i(x, Q_0^2) \quad (5.17)$$

where $q_i(x, Q_0^2)$ are unpolarized parton distributions (quark, sea, gluon) provided in one of several published global analyses of unpolarized structure function data. At the low Q^2 the assumption is made that the parton distributions are valence-like, behaving like x^a as $x \rightarrow 0$. The fit chose the parameters A_i and α_i such that the polarized parton distributions were most consistent with the spin structure function data. The reason for using the unpolarized distributions as a basis for the polarized distribution functions is that they both arise from the same partons, as discussed in Section 2.1. In the naive parton model there is a positivity constraint that $|\Delta q_i| \leq q_i$ since the difference of two quantities cannot be larger than their sum. Arguments for the behavior of the polarized parton distributions as $x \rightarrow 1$ [113] are also used in selecting the fit form of Eq. 5.17.

The unpolarized parton distributions used for the results reported here are from Ref. [39]. They are given in Table 5.5. The assumption was made of a flavor symmetric sea ($\bar{u} = \bar{d} = s = \bar{s}$), allowing the nucleon structure to be described by four distributions:

valence quarks u_V and d_V ; sea quarks \bar{Q} ; and gluons G . The sea quark distributions are parameterized by $\Delta\bar{Q} = \frac{1}{2}(\Delta\bar{u} + \Delta\bar{d}) + \frac{1}{5}\Delta\bar{s}$, a combination of the distributions that represents the sea contribution to g_1 . The distribution given in Table 5.5 is $\frac{1}{2}(\bar{u} + \bar{d})$ from Ref. [39], since this reference uses $s = \bar{s} = 0$. The sea quark contributions in this fitting method are small and these choices do not affect the quality of the fits.

$u_V(x, Q_0^2)$	$=$	$0.632x^{-0.57}(1-x)^{3.09}(1+18.2x)$
$d_V(x, Q_0^2)$	$=$	$0.394x^{-0.57}(1-x)^{4.09}(1+18.2x)$
$\bar{Q}(x, Q_0^2)$	$=$	$0.62x^{-0.80}(1-x)^{8.5}(1-2.3x^{1/2}+5.7x)$
$G(x, Q_0^2)$	$=$	$20.80x^{0.60}(1-x)^{4.1}$

Table 5.5: Unpolarized parton distributions from Ref. [39], known as GRV98. They are given at the input scale $Q_0^2=0.40 \text{ GeV}^2$.

For consistency, the values for $\alpha_S(Q^2)$ used in this fitting procedure also followed the prescription of Ref. [39]. An iterative process was used to generate values from the given implicit solution to the exact running of α at NLO. Using the value $\alpha_S(M_Z^2) = 0.114$, this method results in $\alpha_S(5 \text{ GeV}^2) = 0.26$.

The polarized parton distributions are evolved to the experimental Q^2 by NLO DGLAP equations. Then,

$$g_1(x, Q^2) = \frac{1}{2} \sum_i e_i^2 [C_q \otimes \Delta q_i + C_G \otimes \Delta G] \quad (5.18)$$

where C_q and C_G are perturbative Wilson coefficients. The Wilson coefficients and the splitting functions of the DGLAP equations have been calculated for the polarized case to NLO in the $\overline{\text{MS}}$ scheme [37, 38]. These coefficient functions in leading order

are $C_q(x) = \delta(1-x)$ and $C_G(x) = 0$, which reproduces the naive parton model result $g_1 = \frac{1}{2} \sum_i e_i^2 \Delta q_i$.

The NLO DGLAP evolution process (Eqs. 2.25 and 2.26) and Eq. 5.18 both contain the convolution \otimes :

$$(f \otimes g)(x) = \int_x^1 \frac{dy}{y} f(y) g\left(\frac{x}{y}\right). \quad (5.19)$$

The DGLAP equations are integro-differential equations, and as such not easily tractable as written. In the process of using the polarized parton distributions at some input scale Q_0^2 to calculate g_1 at experimental Q^2 , use is made of Mellin transforms. A function of x , $f(x)$, where $x = [0, 1]$, can instead be written as a function of moment n :

$$f(n) \equiv \int_0^1 \frac{dx}{x} x^n f(x),$$

where $f(n)$ is the Mellin transform of $f(x)$. The Mellin transformation and the convolution integral of Eq. 5.19 are related in that the Mellin transform of the convolution of two functions is equal to the product of the individual Mellin transforms, as shown in the following:

$$\begin{aligned} (f \otimes g)(n) &= \int_0^1 \frac{dx}{x} x^n \left(\int_x^1 \frac{dy}{y} f(y) g\left(\frac{x}{y}\right) \right) \\ &= \int_0^1 \frac{dy}{y} f(y) \int_0^y \frac{dx}{x} x^n g\left(\frac{x}{y}\right) \\ &= \int_0^1 \frac{dy}{y} y^n f(y) \int_0^1 \frac{dz}{z} z^n g(z) \\ &= f(n) g(n). \end{aligned} \quad (5.20)$$

The above steps are: switching the order of integration, which requires changing the limits appropriately; then making the substitution $z = x/y$. Thus, the DGLAP equation

convolutions can be converted to simple products in Mellin n -moment space. The Mellin transforms of the splitting functions P are called anomalous dimensions and denoted by γ . These are also calculated to next-to-leading order in Refs. [37, 38]. By Mellin transformation the DGLAP equations reduce to a system of linear equations and are easily solved numerically. The inverse Mellin transform, where $n = c + z e^{i\phi}$, is:

$$f(x) = \frac{1}{\pi} \int_0^\infty dz \operatorname{Im}[e^{i\phi} x^{-n} f(n)] \quad (5.21)$$

where c is a constant chosen to select a contour of integration to the right of all singularities of $f(n)$ in the complex n -plane. This inverse transform is also calculated numerically.¹

Perturbative QCD is tested to the extent that the DGLAP evolution describes the Q^2 -dependence of the polarized parton distributions, and that a set of polarized parton distributions can consistently describe the data. As a result, the polarized parton distributions permit extraction of $\Delta\Sigma$, ΔG , Γ_1^p , Γ_1^n , and Γ_1^{p-n} .

5.5.2 Results

The following fit results are presented in the $\overline{\text{MS}}$ scheme at $Q^2 = 5 \text{ GeV}^2$. Using Eq. 5.17 and Table 5.5, the coefficients A and α given in Table 5.6 yield the polarized parton distributions which are obtained from the fit. The parameters α were all bounded to be greater than zero. The parameter α_Q was restricted to the range $[0,0.5]$ and the parameter α_G was restricted to the range $[0,2]$.

¹The CERN library routine `rgquad` was used, with integration limits of 0 and 10. The integration is done using the 24-point Gauss-Legendre quadrature formula, with $c = 2.1$ and $\phi = 1.9$.

	Value	Stat.	Syst.
A_u	1.10	+0.05 -0.09	+0.08 -0.09
A_d	-0.51	+0.05 -0.13	+0.04 -0.04
A_Q	0.005	+0.03 -0.01	+0.06 -0.01
A_G	1.51	+3.57 -0.65	+2.83 -0.64
α_u	0.64	+0.04 -0.04	+0.05 -0.06
α_d	0.02	+0.08 -0.02	+0.04 -0.02
α_Q	0.00	+0.19 -0.00	+0.25 -0.00
α_G	0.41	+0.82 -0.30	+0.61 -0.23

Table 5.6: Coefficients for polarized parton distribution fit to world data on $g_1(x, Q^2)$ for proton, neutron, and deuteron.

The resultant polarized parton distributions are shown in Fig. 5.8. The overall $\chi^2/d.o.f.$ for the eight-parameter fit was $285/290 = 0.98$. The success of the fit in describing the data can also be measured in terms of total χ^2 per number of data points for each experiment, as shown in Table 5.7. In general the fit agrees extremely well with the data, with the notable exception of the E155 proton target. (The precision of the E155 data causes it to drive the error of the proton fit. In the case of the proton data, where EMC, SMC, and E143 contribute relatively little to the overall χ^2 , the E155 data are forced to contribute relatively more. Allowing an additional fit parameter for normalization of the E155 proton data results in a scale factor of 0.95, meaning that the fit is improved when the E155 proton g_1 data are scaled to have values 5% smaller than given in Table 5.3. This normalization reduces the $\chi^2/d.o.f.$ for the fit to 0.96, and the total χ^2 for the E155 proton data from 42 to 36.)

Polarized Parton Distributions at $Q^2 = 5 \text{ (GeV/c)}^2$

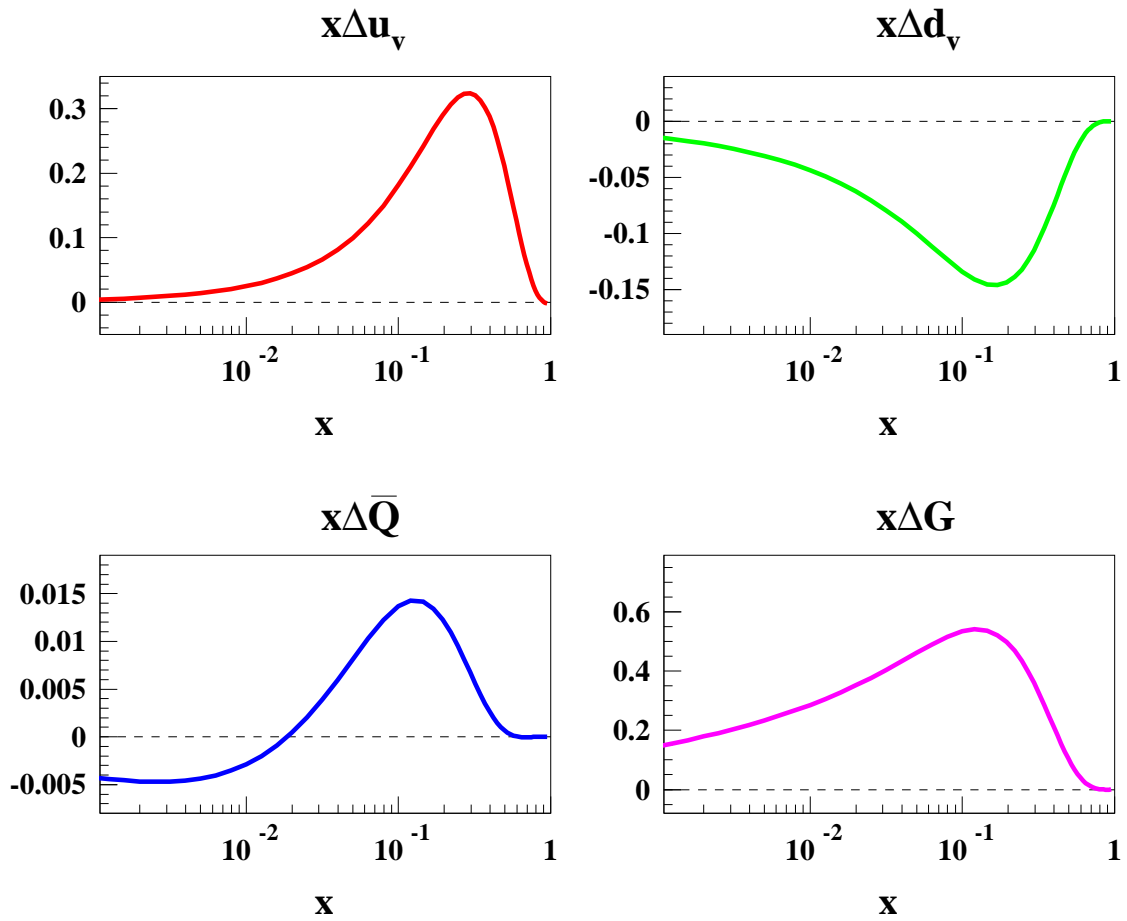


Figure 5.8: The polarized parton distributions corresponding to the fit parameters of Table 5.6.

Experiment		Points	χ^2
E154	n	17	8.3
E142	n	8	3.7
E143	p	81	64.0
	d	81	91.2
SMC	p	12	5.3
	d	12	15.2
HERMES	p	20	28.4
	n	9	2.7
EMC	p	10	6.1
E155	p	24	42.0
	d	24	18.4
Total		298	285.3

Table 5.7: Contribution of each experiment to total χ^2 of the fit.

Given polarized parton distributions, many of the quantities of interest may be determined. For proton and deuteron integrals, the fit obtains:

$$\Gamma_1^p = 0.120_{-0.005}^{+0.006} {}_{-0.007}^{+0.007}, \quad (5.22)$$

$$\Gamma_1^d = 0.028_{-0.005}^{+0.006} {}_{-0.006}^{+0.006}. \quad (5.23)$$

For the Bjorken sum rule, the fit result is:

$$\Gamma_1^{p-n} = 0.180_{-0.004}^{+0.004} {}_{-0.007}^{+0.007}, \quad (5.24)$$

which again can be compared to the theoretical prediction of 0.182 ± 0.005 . Thus in this formalism the Bjorken sum rule is verified to better than 3%.

Lastly, for the quark helicity content and gluon spin contribution, the fit results are:

$$\Delta\Sigma = 0.24^{+0.06\ +0.05}_{-0.05\ -0.06} \quad \text{and} \quad \Delta G = 2.5^{+0.6\ +1.0}_{-0.7\ -1.0}. \quad (5.25)$$

For each quantity, the first pair of uncertainty values is statistical and the second systematic. (Similarly sized errors arise due to theoretical considerations such as input parton distributions and the choice of $\alpha_S(M_Z^2)$, but they are neglected here.) The uncertainties were calculated by performing a large number of fits, typically 800, where for each fit the data points have been scattered for their statistical or systematic uncertainty according to a Gaussian distribution. The statistical errors in the fits were found by scattering each data point independently. The systematic errors were found by scattering all points from each experiment in unison, since the systematic uncertainties in each experiment were mostly correlated scale factors such as target polarization, beam polarization, and dilution factor. The errors on the fit quantities were determined from the RMS of the distributions of the results for each quantity, with the separate plus and minus errors being determined from the part of the distribution greater and less than the central value, respectively. The distributions of the values for 800 fits with data points scattered by statistical uncertainty are shown in Fig. 5.9.

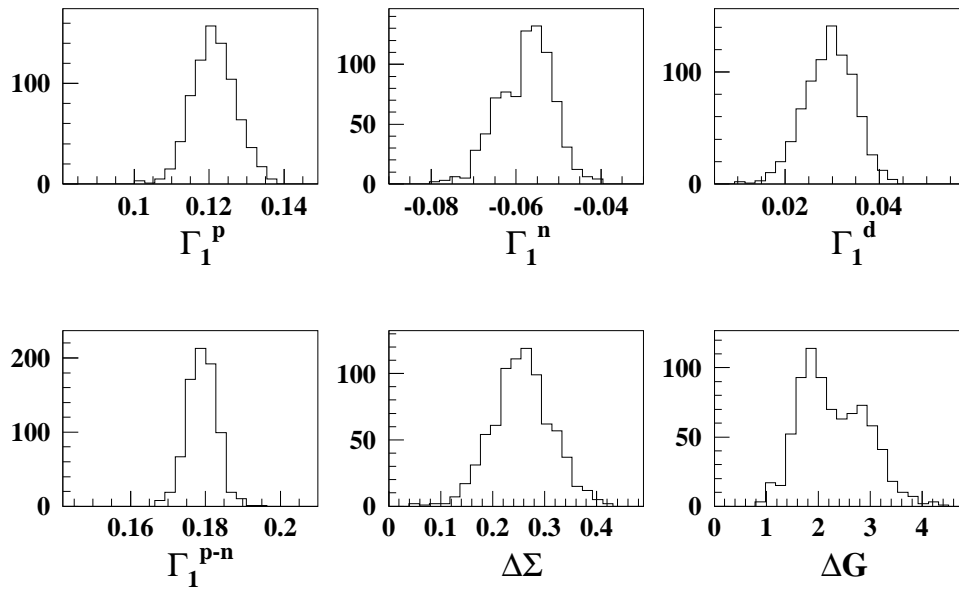


Figure 5.9: Distribution of fit results for 800 fits with input data points scattered by statistical uncertainties. The RMS width of each distribution was used to determine the uncertainty on the central value for the given quantity.

5.6 Conclusion

E155 has precise data on the spin structure functions $g_1^p(x, Q^2)$ and $g_1^d(x, Q^2)$ over a wide kinematic range. The world data set is remarkably self-consistent, and it now provides enough coverage and statistical power to begin rendering sensible interpretations of the spin structure of the nucleon in terms of polarized parton distributions.

E155 independently verifies the Bjorken sum rule at the $1\text{-}\sigma$ level. The world data set, including E155, is also consistent with this fundamental prediction.

The E155 NLO fit result for ΔG has large uncertainty but it seems to indicate a positive contribution. More experimental data directly sensitive to the gluon distribution

need to be obtained before any conclusions can be drawn about the gluon contribution to nucleon spin. The experiment COMPASS at CERN and the currently deferred E156 at SLAC both propose to study ΔG using the asymmetry in open charm photoproduction. HERMES is a continuing experiment and has the power of particle identification in semi-inclusive scattering to provide another level of detail in the study of nucleon spin structure.

The world data constrain well the small quark contribution to the helicity of the nucleon. Further precision for determining polarized parton distributions and $\Delta\Sigma$ will require data at lower x . Though there are some theoretical guidelines, without data the behavior of the polarized structure functions at low x exists only as speculation. Reaching lower x than E155 will require a larger beam energy than 50 GeV, and achieving precision will require an intense, highly polarized lepton beam and a target or beam of polarized nucleons that can produce a sufficiently high event rate. This measurement will have to come from experiments with polarized beams either at an existing storage ring accelerator, possibly HERA at DESY, or at a yet-to-be-built facility, such as a fixed target program at the Next Linear Collider (NLC).

Appendix A

Tracking Code

The tracking code accomplished the task of sorting through the ~ 15 shower counter clusters, ~ 10 Cerenkov pulses in each tank, and several hundred hodoscope hits in each spectrometer in every spill. The code used the shower counter clusters as its starting point. Each cluster was first matched with any Cerenkov pulses that were in time coincidence (corrected for time of flight). Then the hodoscope fingers in time with the cluster were searched for overlaps, and hodoscope clusters were formed in each set of planes. All possible combinations of front plane clusters and rear plane clusters (for the 2.75° and 5.5° spectrometers) were looped over, in a search for any that had an acceptable χ^2 given the time and space resolutions of the detector systems. If any combinations were acceptable, the track combination with the best χ^2 was kept for each shower cluster and copied into a data structure of tracks in the spill.

This strategy was coded in the routines `trk_drv.f` and `trk_fit.f` in the analysis software. A flowchart of the essential logic of these routines is shown in Fig. A.1.

The tracking in the simpler 10.5° spectrometer was accomplished in the same code framework, with three notable differences. First, the looping over possible combinations of front and rear hodoscope cluster combinations had one dummy loop (triggered by the value of the variable `trg_npkg`). Second, since the 10.5° hodoscope only provided

y coordinate information, the tracking algorithm was given a fake point (at $x=0$ and $z=5$ m in spectrometer coordinates, invoked by the logical variable `trc_TenFakeX`) which was to good approximation the image of the target as seen looking back through the optics of the spectrometer. Third, the momentum and angle look-up tables were indexed differently as compared to the other two spectrometers. In the all three spectrometers the shower counter y location and y slope of the track were used as indices to the look-up tables to find the momentum of the track and the scattering angle ϕ at the target. In the small angle spectrometers, the x location and x slope were used to find the scattering angle θ at the target. In the 10.5° spectrometer, the shower counter x location and the momentum of the track were used to find the scattering angle θ at the target.

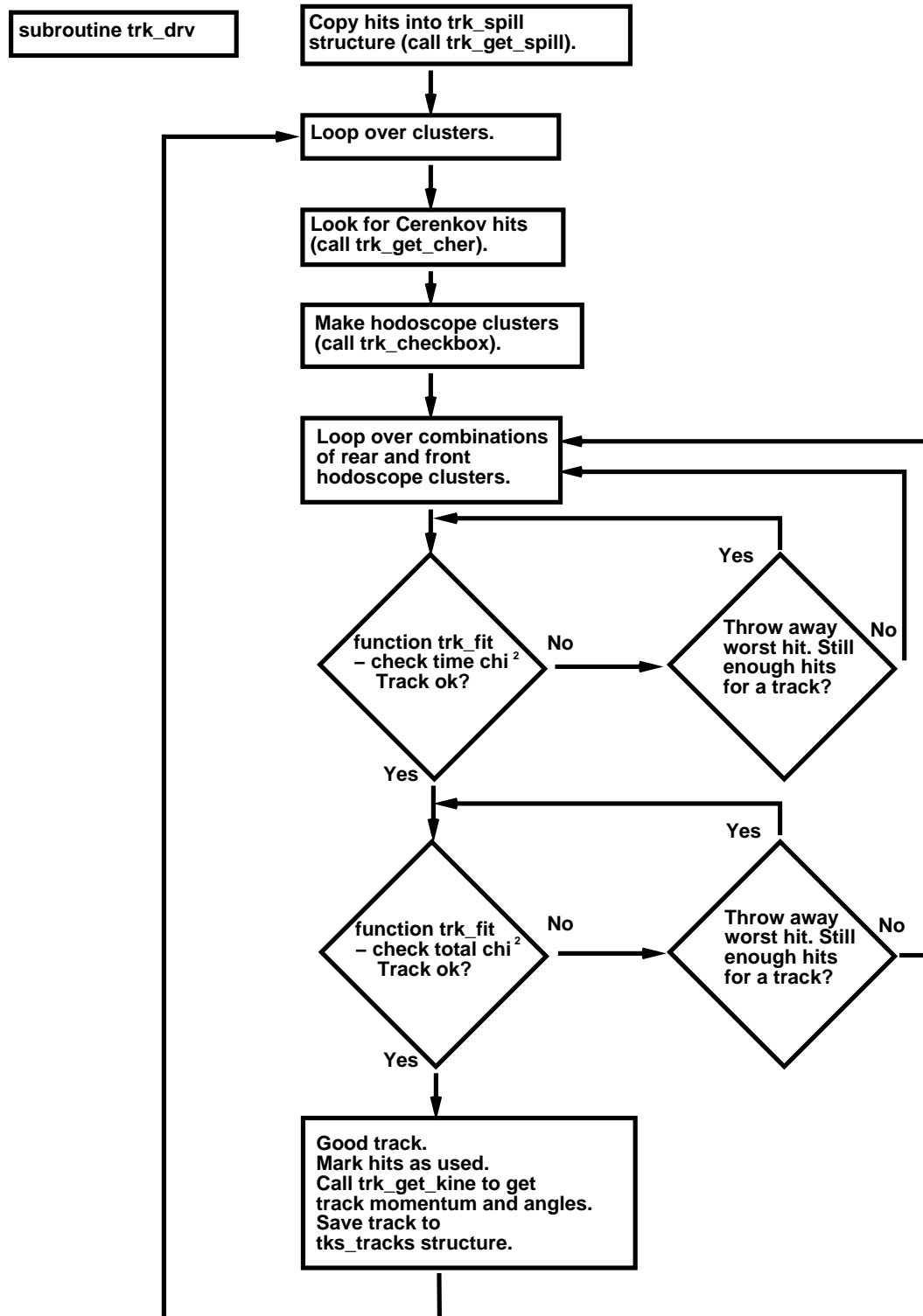


Figure A.1: Flowchart depicting the logic of the routine `trk_drv.f`.

Appendix B

Magnetic Measurements of Møller Magnet B0

The field of Møller magnet B0 was measured in 1995 and in 1996. The results of the field map and field integral were used in determining the analyzing power of the Møller detectors.

The fields were mapped in a fine grid using a Hall probe, and the path integrals for the Møller trajectories were calculated from the Hall probe map as well as measured using several long flip-coils. The Hall probe integrals were 0.7% larger than the flip-coil results. The Hall probe map scaled by 0.993 was used in a Monte Carlo routine to calculate the analyzing power of the Møller detectors for E154, and the flip-coil numbers were used for E155.

In Table B.1, the integral field strength of B0 is listed as a function of current. The values were measured with the so-called ‘Long long’ flip-coil (resting in its frame) on top of the septum, where it was located approximately on the trajectory of a typical Møller scattered electron. In E154 the magnet was run at 900 A, while for E155 the magnet was typically run at 1000 A or higher. The data are also displayed in Fig. B.1.

Current (A)	$\int B dl$ (T·m)
301	1.112
499	1.839
602	2.221
699	2.580
801	2.950
900	3.298

Table B.1: Integrated $B dl$ vs. magnet current, measured with the ‘Long long’ flip-coil.

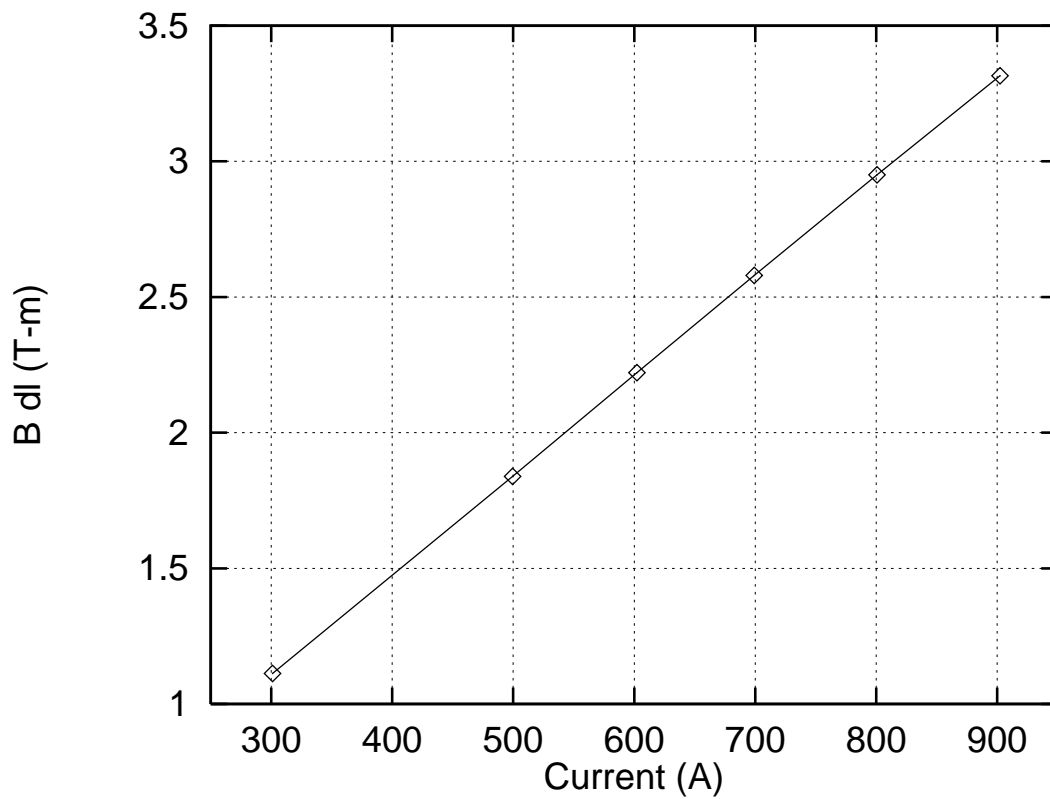


Figure B.1: $\int B dl$ vs. current curve. Measured with the ‘Long long’ flip-coil resting on top of the center of the septum.

Appendix C

Tables of Asymmetry Results

Following are tables of results on A_{\parallel} and A_{\perp} for the proton and deuteron. The values include radiative corrections. The A_{\perp} tables do not include systematic errors since the data are statistics limited. The primary systematic errors are scale factors, as given in Table 4.10. The A_{\parallel} data were taken with beam energy $E_0=48.35$ GeV, while the A_{\perp} data were taken with $E_0=38.77$ GeV.

$$\theta \approx 2.75^\circ$$

Proton			Deuteron		
$\langle x \rangle$	$\langle Q^2 \rangle$	$A_{\parallel} \pm stat \pm syst$	$\langle x \rangle$	$\langle Q^2 \rangle$	$A_{\parallel} \pm stat \pm syst$
0.014	1.00	0.025 ± 0.048 ± 0.004	0.014	1.00	-0.005 ± 0.069 ± 0.003
0.015	1.09	0.029 ± 0.020 ± 0.004	0.015	1.09	-0.006 ± 0.028 ± 0.001
0.017	1.20	0.056 ± 0.014 ± 0.004	0.017	1.20	-0.057 ± 0.020 ± 0.001
0.019	1.32	0.037 ± 0.014 ± 0.004	0.019	1.32	-0.003 ± 0.019 ± 0.001
0.022	1.45	0.037 ± 0.013 ± 0.004	0.022	1.45	0.003 ± 0.019 ± 0.001
0.024	1.59	0.038 ± 0.012 ± 0.004	0.024	1.59	0.014 ± 0.018 ± 0.001
0.027	1.73	0.053 ± 0.011 ± 0.004	0.027	1.73	0.005 ± 0.017 ± 0.001
0.031	1.88	0.051 ± 0.011 ± 0.004	0.031	1.88	0.016 ± 0.017 ± 0.001
0.035	2.04	0.060 ± 0.011 ± 0.004	0.035	2.04	0.000 ± 0.016 ± 0.001
0.039	2.21	0.049 ± 0.010 ± 0.005	0.039	2.21	0.015 ± 0.016 ± 0.001
0.044	2.39	0.079 ± 0.010 ± 0.005	0.044	2.39	0.068 ± 0.015 ± 0.001
0.049	2.59	0.080 ± 0.010 ± 0.005	0.049	2.58	-0.009 ± 0.015 ± 0.001
0.056	2.77	0.066 ± 0.010 ± 0.005	0.056	2.77	-0.009 ± 0.015 ± 0.001
0.063	2.97	0.078 ± 0.010 ± 0.005	0.063	2.97	0.004 ± 0.015 ± 0.001
0.071	3.17	0.086 ± 0.011 ± 0.005	0.071	3.17	0.033 ± 0.015 ± 0.001
0.079	3.37	0.097 ± 0.011 ± 0.005	0.079	3.36	0.045 ± 0.015 ± 0.001
0.089	3.57	0.078 ± 0.011 ± 0.006	0.089	3.57	0.027 ± 0.015 ± 0.001
0.101	3.77	0.079 ± 0.011 ± 0.006	0.101	3.77	0.038 ± 0.016 ± 0.001
0.113	3.97	0.049 ± 0.011 ± 0.006	0.113	3.97	0.036 ± 0.016 ± 0.001
0.127	4.17	0.076 ± 0.011 ± 0.006	0.128	4.17	-0.002 ± 0.016 ± 0.002
0.144	4.36	0.089 ± 0.011 ± 0.006	0.144	4.36	0.038 ± 0.016 ± 0.002
0.162	4.54	0.097 ± 0.012 ± 0.006	0.162	4.55	0.029 ± 0.017 ± 0.002
0.182	4.72	0.089 ± 0.012 ± 0.006	0.182	4.72	0.033 ± 0.018 ± 0.002
0.205	4.88	0.085 ± 0.013 ± 0.006	0.205	4.89	0.041 ± 0.019 ± 0.002
0.230	5.04	0.086 ± 0.013 ± 0.006	0.230	5.04	0.045 ± 0.020 ± 0.002
0.259	5.18	0.112 ± 0.014 ± 0.006	0.259	5.19	0.037 ± 0.021 ± 0.002
0.292	5.33	0.097 ± 0.015 ± 0.006	0.292	5.33	0.057 ± 0.022 ± 0.002
0.328	5.46	0.095 ± 0.015 ± 0.006	0.328	5.47	0.060 ± 0.025 ± 0.003
0.370	5.57	0.082 ± 0.016 ± 0.006	0.370	5.58	0.049 ± 0.028 ± 0.003
0.416	5.68	0.106 ± 0.018 ± 0.006	0.416	5.68	0.000 ± 0.031 ± 0.003
0.468	5.78	0.101 ± 0.020 ± 0.006	0.468	5.78	0.090 ± 0.037 ± 0.003
0.527	5.87	0.048 ± 0.023 ± 0.006	0.527	5.87	0.094 ± 0.044 ± 0.003
0.593	5.94	0.049 ± 0.026 ± 0.006	0.593	5.95	0.113 ± 0.053 ± 0.003
0.668	6.00	0.053 ± 0.031 ± 0.005	0.668	6.00	-0.020 ± 0.062 ± 0.003
0.751	6.06	0.080 ± 0.037 ± 0.005	0.751	6.07	0.089 ± 0.069 ± 0.003
0.846	6.12	0.211 ± 0.061 ± 0.004	0.846	6.12	-0.069 ± 0.085 ± 0.003

Table C.1: E155 results for A_{\parallel} , 2.75° spectrometer.

$\theta \approx 5.5^\circ$

Proton			Deuteron		
$\langle x \rangle$	$\langle Q^2 \rangle$	$A_{\parallel} \pm stat \pm syst$	$\langle x \rangle$	$\langle Q^2 \rangle$	$A_{\parallel} \pm stat \pm syst$
0.057	4.01	$0.204 \pm 0.086 \pm 0.008$	0.057	4.00	$-0.215 \pm 0.140 \pm 0.002$
0.063	4.39	$0.181 \pm 0.039 \pm 0.009$	0.063	4.39	$0.034 \pm 0.061 \pm 0.002$
0.071	4.83	$0.124 \pm 0.025 \pm 0.009$	0.071	4.83	$-0.004 \pm 0.038 \pm 0.002$
0.080	5.30	$0.135 \pm 0.019 \pm 0.010$	0.080	5.30	$-0.002 \pm 0.028 \pm 0.002$
0.090	5.80	$0.136 \pm 0.015 \pm 0.010$	0.090	5.80	$0.010 \pm 0.023 \pm 0.003$
0.101	6.32	$0.145 \pm 0.014 \pm 0.011$	0.101	6.32	$0.071 \pm 0.021 \pm 0.003$
0.113	6.87	$0.140 \pm 0.013 \pm 0.011$	0.113	6.87	$0.014 \pm 0.020 \pm 0.003$
0.128	7.43	$0.183 \pm 0.013 \pm 0.012$	0.128	7.43	$0.053 \pm 0.019 \pm 0.003$
0.144	8.02	$0.198 \pm 0.012 \pm 0.013$	0.144	8.02	$0.084 \pm 0.019 \pm 0.004$
0.162	8.62	$0.174 \pm 0.013 \pm 0.013$	0.162	8.62	$0.057 \pm 0.020 \pm 0.004$
0.182	9.23	$0.182 \pm 0.013 \pm 0.014$	0.182	9.23	$0.068 \pm 0.021 \pm 0.004$
0.205	9.85	$0.187 \pm 0.014 \pm 0.014$	0.205	9.85	$0.065 \pm 0.021 \pm 0.005$
0.230	10.48	$0.234 \pm 0.014 \pm 0.015$	0.230	10.48	$0.114 \pm 0.023 \pm 0.005$
0.259	11.11	$0.217 \pm 0.015 \pm 0.015$	0.259	11.11	$0.089 \pm 0.024 \pm 0.006$
0.292	11.73	$0.233 \pm 0.016 \pm 0.016$	0.292	11.73	$0.145 \pm 0.026 \pm 0.006$
0.328	12.33	$0.224 \pm 0.017 \pm 0.016$	0.328	12.34	$0.123 \pm 0.028 \pm 0.007$
0.370	12.94	$0.253 \pm 0.018 \pm 0.016$	0.370	12.94	$0.163 \pm 0.032 \pm 0.007$
0.416	13.52	$0.251 \pm 0.019 \pm 0.016$	0.416	13.53	$0.106 \pm 0.036 \pm 0.007$
0.468	14.08	$0.204 \pm 0.022 \pm 0.016$	0.468	14.09	$0.103 \pm 0.043 \pm 0.007$
0.526	14.60	$0.221 \pm 0.026 \pm 0.015$	0.526	14.63	$0.146 \pm 0.052 \pm 0.008$
0.592	15.11	$0.222 \pm 0.032 \pm 0.015$	0.592	15.12	$0.259 \pm 0.065 \pm 0.008$
0.666	15.58	$0.195 \pm 0.042 \pm 0.014$	0.666	15.59	$0.252 \pm 0.085 \pm 0.007$
0.749	15.99	$0.269 \pm 0.058 \pm 0.012$	0.749	16.00	$0.030 \pm 0.111 \pm 0.007$
0.843	16.34	$0.253 \pm 0.104 \pm 0.009$	0.843	16.35	$0.148 \pm 0.153 \pm 0.006$

Table C.2: E155 results for A_{\parallel} , 5.5° spectrometer.

$\theta \approx 10.5^\circ$

Proton			Deuteron		
$\langle x \rangle$	$\langle Q^2 \rangle$	$A_{\parallel} \pm stat \pm syst$	$\langle x \rangle$	$\langle Q^2 \rangle$	$A_{\parallel} \pm stat \pm syst$
0.130	10.04	$0.350 \pm 0.149 \pm 0.017$	0.130	10.04	$-0.004 \pm 0.228 \pm 0.005$
0.145	11.14	$0.324 \pm 0.060 \pm 0.018$	0.145	11.14	$-0.006 \pm 0.096 \pm 0.006$
0.162	12.35	$0.243 \pm 0.039 \pm 0.019$	0.163	12.37	$0.207 \pm 0.063 \pm 0.006$
0.182	13.70	$0.311 \pm 0.031 \pm 0.021$	0.182	13.70	$0.107 \pm 0.049 \pm 0.007$
0.205	15.14	$0.328 \pm 0.028 \pm 0.022$	0.205	15.15	$0.166 \pm 0.046 \pm 0.008$
0.230	16.65	$0.416 \pm 0.029 \pm 0.024$	0.230	16.67	$0.086 \pm 0.047 \pm 0.009$
0.259	18.27	$0.366 \pm 0.032 \pm 0.026$	0.259	18.28	$0.206 \pm 0.051 \pm 0.010$
0.291	20.02	$0.514 \pm 0.035 \pm 0.027$	0.292	20.04	$0.249 \pm 0.057 \pm 0.011$
0.328	21.86	$0.495 \pm 0.038 \pm 0.029$	0.328	21.86	$0.186 \pm 0.062 \pm 0.012$
0.369	23.80	$0.465 \pm 0.041 \pm 0.031$	0.369	23.78	$0.370 \pm 0.073 \pm 0.013$
0.413	25.85	$0.382 \pm 0.054 \pm 0.032$	0.414	25.90	$0.211 \pm 0.098 \pm 0.015$
0.465	27.94	$0.420 \pm 0.088 \pm 0.033$	0.465	28.04	$0.332 \pm 0.153 \pm 0.016$
0.524	30.11	$0.401 \pm 0.142 \pm 0.034$	0.524	30.19	$0.366 \pm 0.253 \pm 0.017$
0.590	32.28	$0.648 \pm 0.204 \pm 0.033$	0.590	32.36	$-0.183 \pm 0.389 \pm 0.017$
0.663	34.73	$0.556 \pm 0.338 \pm 0.032$	0.661	34.79	$0.315 \pm 0.649 \pm 0.017$

Table C.3: E155 results for A_{\parallel} , 10.5° spectrometer.

$\theta \approx 2.75^\circ$

Proton			Deuteron		
$\langle x \rangle$	$\langle Q^2 \rangle$	$A_\perp \pm stat$	$\langle x \rangle$	$\langle Q^2 \rangle$	$A_\perp \pm stat$
0.022	1.15	0.019 \pm 0.092	0.022	1.15	-0.040 \pm 0.069
0.025	1.25	0.020 \pm 0.037	0.025	1.25	0.001 \pm 0.028
0.027	1.35	-0.043 \pm 0.027	0.027	1.35	0.011 \pm 0.020
0.031	1.42	-0.017 \pm 0.028	0.031	1.42	0.010 \pm 0.020
0.035	1.48	-0.035 \pm 0.028	0.035	1.48	0.018 \pm 0.020
0.039	1.56	-0.029 \pm 0.028	0.039	1.56	0.046 \pm 0.020
0.044	1.65	-0.048 \pm 0.027	0.044	1.65	-0.032 \pm 0.020
0.049	1.76	0.022 \pm 0.027	0.049	1.76	0.006 \pm 0.019
0.056	1.86	-0.024 \pm 0.028	0.056	1.86	-0.031 \pm 0.020
0.063	1.95	0.011 \pm 0.028	0.063	1.95	0.003 \pm 0.020
0.071	2.05	0.005 \pm 0.028	0.071	2.05	0.007 \pm 0.020
0.079	2.16	-0.008 \pm 0.028	0.079	2.16	-0.033 \pm 0.020
0.089	2.26	0.017 \pm 0.029	0.089	2.26	0.019 \pm 0.021
0.101	2.35	-0.023 \pm 0.029	0.101	2.35	0.014 \pm 0.021
0.113	2.45	-0.058 \pm 0.030	0.113	2.45	0.034 \pm 0.021
0.128	2.55	0.004 \pm 0.030	0.128	2.55	0.002 \pm 0.022
0.144	2.64	0.018 \pm 0.031	0.144	2.64	0.006 \pm 0.023
0.162	2.72	-0.085 \pm 0.031	0.162	2.72	0.013 \pm 0.023
0.182	2.80	-0.001 \pm 0.031	0.182	2.80	-0.021 \pm 0.024
0.205	2.88	-0.021 \pm 0.032	0.205	2.88	-0.024 \pm 0.024
0.230	2.96	-0.002 \pm 0.033	0.230	2.96	0.001 \pm 0.025
0.259	3.03	0.030 \pm 0.034	0.259	3.03	-0.004 \pm 0.027
0.292	3.09	-0.019 \pm 0.037	0.292	3.09	-0.094 \pm 0.029
0.328	3.15	-0.069 \pm 0.040	0.328	3.15	-0.014 \pm 0.032
0.370	3.20	0.014 \pm 0.043	0.370	3.21	-0.018 \pm 0.035
0.416	3.26	0.043 \pm 0.047	0.416	3.26	0.050 \pm 0.040
0.468	3.29	-0.047 \pm 0.053	0.468	3.29	-0.027 \pm 0.046
0.527	3.33	-0.029 \pm 0.059	0.527	3.33	-0.022 \pm 0.054
0.593	3.36	0.005 \pm 0.066	0.593	3.35	-0.012 \pm 0.063
0.667	3.38	-0.082 \pm 0.075	0.668	3.38	0.049 \pm 0.074
0.752	3.40	-0.122 \pm 0.093	0.751	3.40	-0.008 \pm 0.085
0.846	3.43	-0.024 \pm 0.150	0.846	3.42	-0.349 \pm 0.105

Table C.4: E155 results for A_\perp , 2.75° spectrometer.

$\theta \approx 5.5^\circ$

Proton			Deuteron		
$\langle x \rangle$	$\langle Q^2 \rangle$	$A_\perp \pm stat$	$\langle x \rangle$	$\langle Q^2 \rangle$	$A_\perp \pm stat$
0.072	3.71	0.102 ± 0.149	0.072	3.71	-0.131 ± 0.108
0.080	4.03	-0.088 ± 0.080	0.080	4.03	0.021 ± 0.058
0.090	4.39	-0.041 ± 0.058	0.090	4.39	0.044 ± 0.042
0.101	4.76	0.020 ± 0.048	0.101	4.76	-0.009 ± 0.035
0.113	5.14	-0.028 ± 0.043	0.113	5.13	0.062 ± 0.032
0.128	5.52	0.050 ± 0.040	0.128	5.52	-0.011 ± 0.030
0.144	5.91	-0.006 ± 0.039	0.144	5.91	0.028 ± 0.029
0.162	6.31	0.002 ± 0.039	0.162	6.31	0.090 ± 0.029
0.182	6.69	0.011 ± 0.039	0.182	6.69	-0.011 ± 0.030
0.205	7.07	0.026 ± 0.041	0.205	7.07	-0.026 ± 0.032
0.230	7.45	0.051 ± 0.042	0.230	7.45	-0.018 ± 0.034
0.259	7.83	0.009 ± 0.045	0.259	7.83	0.054 ± 0.036
0.292	8.19	0.063 ± 0.047	0.292	8.19	0.098 ± 0.039
0.328	8.53	-0.037 ± 0.051	0.329	8.53	-0.016 ± 0.042
0.370	8.89	0.064 ± 0.055	0.370	8.88	-0.065 ± 0.047
0.416	9.23	-0.032 ± 0.061	0.416	9.23	0.061 ± 0.053
0.468	9.54	-0.104 ± 0.070	0.468	9.54	-0.004 ± 0.061
0.526	9.82	0.001 ± 0.080	0.527	9.82	0.049 ± 0.074
0.593	10.08	-0.174 ± 0.095	0.592	10.08	-0.095 ± 0.089
0.666	10.35	0.045 ± 0.117	0.666	10.36	-0.034 ± 0.112
0.750	10.59	-0.316 ± 0.158	0.749	10.57	0.263 ± 0.143
0.843	10.79	0.348 ± 0.268	0.843	10.79	0.052 ± 0.189

Table C.5: E155 results for A_\perp , 5.5° spectrometer.

$\theta \approx 10.5^\circ$

Proton			Deuteron		
$\langle x \rangle$	$\langle Q^2 \rangle$	$A_\perp \pm stat$	$\langle x \rangle$	$\langle Q^2 \rangle$	$A_\perp \pm stat$
0.129	7.58	0.009 ± 0.186	0.129	7.58	-0.018 ± 0.139
0.144	8.38	0.007 ± 0.120	0.144	8.38	-0.128 ± 0.090
0.162	9.27	-0.145 ± 0.106	0.162	9.27	-0.023 ± 0.079
0.182	10.32	0.100 ± 0.098	0.182	10.33	-0.173 ± 0.075
0.205	11.44	0.072 ± 0.093	0.205	11.46	-0.136 ± 0.070
0.230	12.62	-0.105 ± 0.095	0.230	12.63	0.077 ± 0.074
0.259	13.78	-0.090 ± 0.103	0.259	13.77	0.022 ± 0.080
0.292	14.97	0.121 ± 0.114	0.292	14.94	-0.172 ± 0.090
0.328	16.14	-0.033 ± 0.119	0.329	16.09	-0.136 ± 0.097
0.370	17.23	-0.054 ± 0.121	0.370	17.23	-0.051 ± 0.102
0.416	18.43	0.041 ± 0.130	0.417	18.42	-0.100 ± 0.111
0.468	19.44	0.092 ± 0.135	0.469	19.47	0.080 ± 0.119
0.528	20.44	0.044 ± 0.144	0.527	20.49	0.098 ± 0.136
0.593	21.49	0.014 ± 0.158	0.593	21.59	-0.040 ± 0.156
0.668	22.64	0.012 ± 0.177	0.667	22.73	0.448 ± 0.179
0.750	23.72	0.503 ± 0.217	0.750	23.77	-0.356 ± 0.209
0.845	24.84	-0.264 ± 0.327	0.845	24.94	-0.053 ± 0.241

Table C.6: E155 results for A_\perp , 10.5° spectrometer.

Appendix D

Systematic Error Breakdown

The systematic errors for the spin structure function results come from many sources. The dominant sources come from the target system: polarization, dilution factor, and nuclear corrections. The other most significant sources of systematic error are radiative corrections and beam polarization. These are all treated (some as x -dependent quantities) as scale errors on A_{\parallel} .

Fits to the unpolarized functions F_2 [22] and R [21] are used in transforming the experimentally measured quantity A_{\parallel} to g_1/F_1 and g_1 . The uncertainties in these fits are treated as systematic uncertainties on g_1/F_1 and g_1 . The following relations were used in calculating their contributions (neglecting terms with A_{\perp}):

$$\frac{\partial(g_1/F_1)}{\partial R} = \frac{\epsilon y}{(1 - \epsilon)(2 - y)} A_{\parallel}, \quad (\text{D.1})$$

$$\frac{\partial g_1}{\partial R} = \frac{F_1}{D'} \left(\frac{\epsilon - 1}{(1 + R)(1 + \epsilon R)} \right) A_{\parallel}, \quad (\text{D.2})$$

$$\frac{\partial g_1}{\partial F_2} = \frac{1}{D'} \left(\frac{1 + \gamma^2}{2x(1 + R)} \right) A_{\parallel}. \quad (\text{D.3})$$

The contribution of each factor for g_1 is given in Table D.1 for the proton and in Table D.2 for the deuteron. The polynomial E155 fit to world data (Eq. 5.3 and Table 5.1) was used to generate the systematic error contributions, to ensure that the systematic errors varied smoothly with x .

Systematic Errors Proton 2.75° spectrometer

bin	$\langle x \rangle$	$\langle Q^2 \rangle$	g_1	σ_{stat}	σ_{syst}	P_b	P_t	f	e^+/π	C_1	C_2	F_2	R	RC
1	0.015	1.22	0.3687	0.0838	0.0359	0.0089	0.0214	0.0089	0.0036	0.0018	0.0000	0.0081	0.0120	0.0211
2	0.025	1.59	0.2980	0.0476	0.0301	0.0085	0.0204	0.0085	0.0034	0.0017	0.0000	0.0069	0.0052	0.0159
3	0.035	2.05	0.3131	0.0363	0.0274	0.0084	0.0202	0.0084	0.0034	0.0017	0.0000	0.0067	0.0038	0.0114
4	0.050	2.57	0.3714	0.0288	0.0250	0.0081	0.0195	0.0081	0.0032	0.0016	0.0000	0.0064	0.0025	0.0074
5	0.080	3.24	0.3406	0.0205	0.0226	0.0075	0.0181	0.0075	0.0030	0.0015	0.0000	0.0060	0.0013	0.0046
6	0.125	4.03	0.2469	0.0179	0.0208	0.0070	0.0168	0.0070	0.0028	0.0014	0.0000	0.0059	0.0005	0.0030
7	0.175	4.62	0.2775	0.0244	0.0193	0.0065	0.0156	0.0065	0.0026	0.0013	0.0000	0.0058	0.0003	0.0021
8	0.250	5.06	0.2362	0.0163	0.0169	0.0057	0.0136	0.0057	0.0023	0.0011	0.0000	0.0052	0.0001	0.0015
9	0.350	5.51	0.1722	0.0211	0.0129	0.0043	0.0104	0.0043	0.0017	0.0009	0.0000	0.0039	0.0001	0.0013
10	0.500	5.77	0.0921	0.0108	0.0070	0.0023	0.0056	0.0023	0.0009	0.0005	0.0000	0.0020	0.0000	0.0008

Systematic Errors Proton 5.5° spectrometer

bin	$\langle x \rangle$	$\langle Q^2 \rangle$	g_1	σ_{stat}	σ_{syst}	P_b	P_t	f	e^+/π	C_1	C_2	F_2	R	RC
4	0.050	4.01	0.7349	0.3228	0.0311	0.0092	0.0220	0.0092	0.0037	0.0018	0.0000	0.0077	0.0091	0.0124
5	0.080	5.36	0.3465	0.0265	0.0263	0.0084	0.0201	0.0084	0.0034	0.0017	0.0000	0.0068	0.0053	0.0078
6	0.125	7.17	0.3086	0.0117	0.0229	0.0076	0.0182	0.0076	0.0030	0.0015	0.0000	0.0063	0.0023	0.0046
7	0.175	8.90	0.2555	0.0127	0.0205	0.0069	0.0165	0.0069	0.0027	0.0014	0.0000	0.0060	0.0016	0.0026
8	0.250	10.64	0.2313	0.0074	0.0171	0.0058	0.0138	0.0058	0.0023	0.0012	0.0000	0.0052	0.0009	0.0013
9	0.350	12.60	0.1708	0.0082	0.0123	0.0041	0.0099	0.0041	0.0017	0.0008	0.0000	0.0037	0.0004	0.0010
10	0.500	14.02	0.0784	0.0037	0.0058	0.0020	0.0047	0.0020	0.0008	0.0004	0.0000	0.0017	0.0001	0.0007
11	0.750	15.70	0.0102	0.0016	0.0007	0.0002	0.0005	0.0002	0.0001	0.0000	0.0000	0.0002	0.0000	0.0001

Systematic Errors Proton 10.5° spectrometer

bin	$\langle x \rangle$	$\langle Q^2 \rangle$	g_1	σ_{stat}	σ_{syst}	P_b	P_t	f	e^+/π	C_1	C_2	F_2	R	RC
6	0.125	10.99	0.4449	0.0810	0.0258	0.0079	0.0190	0.0079	0.0032	0.0016	0.0000	0.0065	0.0069	0.0086
7	0.175	13.18	0.2865	0.0239	0.0218	0.0070	0.0168	0.0070	0.0028	0.0014	0.0000	0.0060	0.0043	0.0057
8	0.250	17.19	0.2610	0.0095	0.0174	0.0057	0.0137	0.0057	0.0023	0.0011	0.0000	0.0051	0.0028	0.0029
9	0.350	22.73	0.1785	0.0096	0.0119	0.0040	0.0095	0.0040	0.0016	0.0008	0.0000	0.0035	0.0017	0.0015
10	0.500	26.88	0.0604	0.0057	0.0052	0.0017	0.0042	0.0017	0.0007	0.0003	0.0000	0.0015	0.0005	0.0008
11	0.750	34.73	0.0075	0.0047	0.0005	0.0002	0.0004	0.0002	0.0001	0.0000	0.0000	0.0002	0.0000	0.0001

Table D.1: Proton systematic error contributions. The column headings represent: P_b , beam polarization; P_t , target polarization; f , dilution factor; C_1 and C_2 , nuclear corrections; F_2 and R , unpolarized structure functions; and RC , radiative corrections.

Systematic Errors Deuteron 2.75° spectrometer

<i>bin</i>	$\langle x \rangle$	$\langle Q^2 \rangle$	<i>g_t</i>	σ_{stat}	σ_{sys}	P_b	P_t	<i>f</i>	e^+/π	C_1	C_2	F_2	<i>R</i>	<i>RC</i>
1	0.015	1.22	-0.2345	0.1145	0.0111	0.0019	0.0031	0.0023	0.0008	0.0021	0.0010	0.0018	0.0026	0.0094
2	0.025	1.59	0.0506	0.0681	0.0061	0.0002	0.0002	0.0002	0.0001	0.0002	0.0010	0.0001	0.0001	0.0060
3	0.035	2.05	0.0590	0.0520	0.0045	0.0006	0.0010	0.0007	0.0003	0.0007	0.0010	0.0005	0.0003	0.0041
4	0.050	2.57	0.0816	0.0406	0.0043	0.0013	0.0020	0.0015	0.0005	0.0014	0.0010	0.0009	0.0004	0.0027
5	0.080	3.24	0.1034	0.0278	0.0051	0.0018	0.0028	0.0021	0.0007	0.0019	0.0009	0.0012	0.0003	0.0021
6	0.125	4.03	0.0893	0.0238	0.0056	0.0021	0.0033	0.0024	0.0008	0.0023	0.0008	0.0014	0.0002	0.0012
7	0.175	4.62	0.0833	0.0320	0.0059	0.0022	0.0036	0.0026	0.0009	0.0024	0.0008	0.0015	0.0001	0.0010
8	0.250	5.06	0.0956	0.0207	0.0057	0.0022	0.0035	0.0025	0.0009	0.0023	0.0007	0.0015	0.0001	0.0009
9	0.350	5.51	0.0860	0.0280	0.0048	0.0018	0.0029	0.0021	0.0007	0.0020	0.0005	0.0014	0.0000	0.0008
10	0.500	5.77	0.0468	0.0155	0.0028	0.0011	0.0017	0.0012	0.0004	0.0012	0.0003	0.0008	0.0000	0.0005

Systematic Errors Deuteron 5.5° spectrometer

<i>bin</i>	$\langle x \rangle$	$\langle Q^2 \rangle$	<i>g_t</i>	σ_{stat}	σ_{sys}	P_b	P_t	<i>f</i>	e^+/π	C_1	C_2	F_2	<i>R</i>	<i>RC</i>
4	0.050	4.00	-0.7871	0.5036	0.0063	0.0014	0.0023	0.0016	0.0006	0.0015	0.0011	0.0012	0.0014	0.0048
5	0.080	5.37	0.0116	0.0379	0.0065	0.0020	0.0032	0.0023	0.0008	0.0021	0.0010	0.0015	0.0013	0.0035
6	0.125	7.16	0.0940	0.0163	0.0063	0.0023	0.0037	0.0027	0.0009	0.0025	0.0009	0.0016	0.0007	0.0019
7	0.175	8.90	0.0798	0.0175	0.0063	0.0024	0.0038	0.0027	0.0009	0.0026	0.0008	0.0016	0.0005	0.0012
8	0.250	10.62	0.0903	0.0099	0.0059	0.0022	0.0035	0.0026	0.0009	0.0024	0.0007	0.0016	0.0003	0.0008
9	0.350	12.59	0.0808	0.0115	0.0046	0.0017	0.0028	0.0020	0.0007	0.0019	0.0005	0.0013	0.0002	0.0006
10	0.500	14.01	0.0340	0.0055	0.0024	0.0009	0.0014	0.0010	0.0004	0.0010	0.0002	0.0006	0.0001	0.0004
11	0.750	15.73	0.0061	0.0023	0.0003	0.0001	0.0002	0.0001	0.0000	0.0001	0.0000	0.0001	0.0000	0.0001

Systematic Errors Deuteron 10.5° spectrometer

<i>bin</i>	$\langle x \rangle$	$\langle Q^2 \rangle$	<i>g_t</i>	σ_{stat}	σ_{sys}	P_b	P_t	<i>f</i>	e^+/π	C_1	C_2	F_2	<i>R</i>	<i>RC</i>
6	0.125	10.98	-0.0249	0.1173	0.0076	0.0024	0.0038	0.0028	0.0010	0.0026	0.0010	0.0017	0.0021	0.0037
7	0.175	13.19	0.1275	0.0340	0.0070	0.0024	0.0039	0.0028	0.0010	0.0026	0.0008	0.0016	0.0015	0.0026
8	0.250	17.22	0.0937	0.0130	0.0061	0.0022	0.0035	0.0026	0.0009	0.0024	0.0007	0.0016	0.0011	0.0017
9	0.350	22.65	0.0774	0.0133	0.0045	0.0017	0.0027	0.0019	0.0007	0.0018	0.0005	0.0013	0.0007	0.0010
10	0.500	26.97	0.0283	0.0079	0.0021	0.0008	0.0013	0.0009	0.0003	0.0009	0.0002	0.0006	0.0002	0.0004
11	0.750	34.79	0.0032	0.0067	0.0002	0.0001	0.0001	0.0001	0.0000	0.0001	0.0000	0.0001	0.0000	0.0000

Table D.2: Deuteron systematic error contributions. The column headings represent: P_b , beam polarization; P_t , target polarization; *f*, dilution factor; C_1 and C_2 , nuclear corrections; F_2 and *R*, unpolarized structure functions; and *RC*, radiative corrections.

Appendix E

The E155 Collaboration

P.L. Anthony,¹⁶ R.G. Arnold,¹ T. Averett,^{5,*} H.R. Band,²¹ M.C. Berisso,¹² H. Borel,⁷
P.E. Bosted,¹ S.L. Bültmann,¹⁹ M. Buenerd,^{16,†} T. Chupp,¹³ S. Churchwell,^{12,‡} G.R. Court,¹⁰
D. Crabb,¹⁹ D. Day,¹⁹ P. Decowski,¹⁵ P. DePietro,¹ R. Erbacher,^{16,17} R. Erickson,¹⁶
A. Feltham,¹⁹ H. Fonvieille,³ E. Frlez,¹⁹ R. Gearhart,¹⁶ V. Ghazikhanian,⁶ J. Gomez,¹⁸
K.A. Griffioen,²⁰ C. Harris,¹⁹ M.A. Houlden,¹⁰ E.W. Hughes,⁵ C.E. Hyde-Wright,¹⁴
G. Igo,⁶ S. Incerti,³ J. Jensen,⁵ J.R. Johnson,²¹ P.M. King,²⁰ Yu.G. Kolomensky,^{5,12}
S.E. Kuhn,¹⁴ R. Lindgren,¹⁹ R.M. Lombard-Nelsen,⁷ J. Marroncle,⁷ J. McCarthy,¹⁹
P. McKee,¹⁹ W. Meyer,⁴ G. Mitchell,²¹ J. Mitchell,¹⁸ M. Olson,^{9,§} S. Penttila,¹¹ G. Peterson,¹²
G.G. Petratos,⁹ R. Pitthan,¹⁶ D. Pocanic,¹⁹ R. Prepost,²¹ C. Prescott,¹⁶ L.M. Qin,¹⁴
B.A. Raue,⁸ D. Reyna,¹ L.S. Rochester,¹⁶ S. Rock,¹ O.A. Rondon-Aramayo,¹⁹ F. Sabatie,⁷
I. Sick,² T. Smith,^{13,◇} L. Sorrell,¹ F. Staley,⁷ S. St.Lorant,¹⁶ L.M. Stuart,^{16,||} Z. Szalata,¹
Y. Terrien,⁷ A. Tobias,¹⁹ L. Todor,¹⁴ T. Toole,¹ S. Trentalange,⁶ D. Walz,¹⁶ R.C. Welsh,¹³
F.R. Wesselmann,¹⁴ T.R. Wright,²¹ C.C. Young,¹⁶ M. Zeier,² H. Zhu,¹⁹ B. Zihlmann¹⁹

¹American University, Washington, D.C. 20016

²Institut für Physik der Universität Basel, CH-4056 Basel, Switzerland

³University Blaise Pascal, LPC IN2P3/CNRS F-63170 Aubiere Cedex, France

⁴Ruhr-Universität Bochum, Universitätstr. 150, Bochum, Germany

⁵California Institute of Technology, Pasadena, California 91125

⁶University of California, Los Angeles, California 90095

⁷DAPNIA-Service de Physique Nuclaire, CEA-Saclay, F-91191 Gif/Yvette Cedex, France

⁸Florida International University, Miami, Florida 33199

⁹Kent State University, Kent, Ohio 44242

¹⁰University of Liverpool, Liverpool L69 3BX, United Kingdom

¹¹Los Alamos National Laboratory, Los Alamos, New Mexico 87545

¹²University of Massachusetts, Amherst, Massachusetts 01003

¹³University of Michigan, Ann Arbor, Michigan 48109

¹⁴Old Dominion University, Norfolk, Virginia 23529

¹⁵Smith College, Northampton, Massachusetts 01063

¹⁶Stanford Linear Accelerator Center, Stanford, California 94309

¹⁷Stanford University, Stanford, California 94305

¹⁸Thomas Jefferson National Accelerator Facility, Newport News, Virginia 23606

¹⁹University of Virginia, Charlottesville, Virginia 22901

²⁰The College of William and Mary, Williamsburg, Virginia 23187

²¹University of Wisconsin, Madison, Wisconsin 53706

* Present address: College of William and Mary, Williamsburg, Virginia 23187

† Permanent Address: Institut des Sciences Nucléaires, IN2P3/CNRS, 38026 Grenoble Cedex, France

‡ Present Address: Duke University, TUNL, Durham, North Carolina 27708

◇ Present Address: Los Alamos National Laboratory, Los Alamos, New Mexico 87545

§ Present Address: St. Norbert College, De Pere, Wisconsin 54115

‖ Present Address: Lawrence Livermore National Laboratory, Livermore, California 94551

Bibliography

- [1] E. D. Bloom *et al.*, Phys. Rev. Lett. **23**, 930 (1969).
- [2] M. Breidenbach *et al.*, Phys. Rev. Lett. **23**, 935 (1969).
- [3] H. W. Kendall and W. K. H. Panofsky, Sci. Am. **224**, 60 (1971).
- [4] J. Friedman and H. Kendall, Ann. Rev. Nucl. Sci. **22**, 203 (1972).
- [5] J. D. Bjorken, Phys. Rev. **179**, 1547 (1969).
- [6] R. P. Feynman, Phys. Rev. Lett. **23**, 1415 (1969).
- [7] E142, P. L. Anthony *et al.*, Phys. Rev. **D54**, 6620 (1996).
- [8] E143, K. Abe *et al.*, Phys. Rev. **D58**, 112003 (1998).
- [9] E154, K. Abe *et al.*, Phys. Rev. Lett. **79**, 26 (1997).
- [10] E154, K. Abe *et al.*, Phys. Lett. **B404**, 377 (1997).
- [11] E154, K. Abe *et al.*, Phys. Lett. **B405**, 180 (1997).
- [12] The European Muon Collaboration, J. Ashman *et al.*, Phys. Rev. **B206**, 364 (1988); Nucl. Phys. **B328**, 1 (1990).
- [13] The Spin Muon Collaboration, B. Adeva *et al.*, Phys. Rev. **D58**, 112001 (1998).
- [14] The Spin Muon Collaboration, B. Adeva *et al.*, Phys. Rev. **D58**, 112002 (1998).

- [15] HERMES Collaboration, K. Ackerstaff *et al.*, Phys. Lett. **B404**, 383 (1997).
- [16] HERMES Collaboration, A. Airapetian *et al.*, Phys. Lett. **B442**, 484 (1998).
- [17] F. Halzen and A. D. Martin, *Quarks and Leptons*, John Wiley & Sons (1984).
- [18] R. G. Roberts, *The Structure of the Proton*, Cambridge University Press (1990).
- [19] L.W. Whitlow, SLAC-Report-357 (1990).
- [20] L.W. Whitlow *et al.*, Phys. Lett. **B250**, 193 (1990).
- [21] E143, K. Abe *et al.*, SLAC-PUB-7927 (1998).
- [22] NMC, M. Arneodo *et al.*, Phys. Lett. **B364**, 107 (1995).
- [23] J. M. Bauer, SLAC-Report-492 (1996); Ph. D. thesis, University of Massachusetts Amherst, September 1996, pp. 23-26.
- [24] V. W. Hughes and J. Kuti, Ann. Rev. Nucl. Part. Sci. **33**, 611 (1983).
- [25] The Spin Muon Collaboration, D. Adams *et al.*, Phys. Rev. **D56**, 5330 (1997).
- [26] P. Bosted, E143 Technical Note 19, 1993 (unpublished).
- [27] D. Bailin, *Weak Interactions*, 2nd Ed., Adam Hilger Ltd (1982), pp. 172-175.
- [28] E. D. Commins and P. H. Bucksbaum, *Weak Interactions of Leptons and Quarks*, Cambridge University Press (1983), pp. 215-221.
- [29] M. Bourquin *et al.*, Z. Phys. **C21**, 27 (1983).

- [30] Particle Data Group, C. Caso *et al.*, Eur. Phys. J. **C3**, 1 (1998).
- [31] R. D. Erbacher, E155 Technical Note 69, September 1998 (unpublished).
- [32] L.W. Whitlow *et al.*, Phys. Lett. **B282**, 475 (1992).
- [33] BCDMS, A. C. Benvenuti *et al.*, Phys. Lett. **B233**, 485 (1989); Phys. Lett. **B237**, 592 (1990).
- [34] V. N. Gribov and L. N. Lipatov, Sov. J. Nucl. Phys. **15**, 438 (1972); Sov. J. Nucl. Phys. **15**, 675 (1972).
- [35] Y. L. Dokshitzer Sov. Phys. JETP **46**, 461 (1977).
- [36] G. Altarelli and G. Parisi, Nucl. Phys. **B126**, 298 (1977).
- [37] R. Mertig and W. L. van Neerven, Z. Phys. **C70**, 637 (1996).
- [38] W. Vogelsang, Phys. Rev. **D54**, 2023 (1996).
- [39] M. Glück, E. Reya, and A. Vogt, Eur. Phys. J. **C5**, 461 (1998).
- [40] M. E. Peskin and D. V. Schroeder, *An Introduction to Quantum Field Theory*, Addison-Wesley Publishing Company (1995), p. 631.
- [41] J. Ellis and M. Karliner, Phys. Lett. **B341**, 397 (1995).
- [42] J. D. Bjorken, Phys. Rev. **148**, 1467 (1966).
- [43] S. A. Larin and J. A. M. Vermaseren, Phys. Lett. **B259**, 345 (1991).

- [44] J. Ellis and R. L. Jaffe, Phys. Rev. **D9**, 1444 (1974); **D10** 1669 (1974).
- [45] S. A. Larin, Phys. Lett. **B334**, 192 (1994).
- [46] R. Prepost and T. Maruyama, Ann. Rev. Nucl. Part. Sci. **45**, 41 (1995).
- [47] R. Alley *et al.*, Nucl. Instr. Meth. **A365**, 1 (1995).
- [48] R. Erickson *et al.*, SLAC-PUB-5891 (1992).
- [49] R. Erickson *et al.*, SLAC-PUB-6898 (1995).
- [50] C. Young, E143 Technical Note 96, 1995 (unpublished).
- [51] J. A. Dunne, Ph. D. thesis, The American University, 1995, pp. 77-79 (unpublished).
- [52] C. Møller, Ann. Phys. **14**, 532 (1932).
- [53] A. M. Bincer, Phys. Rev. **107**, 1434 (1957).
- [54] G. G. Scott, H. W. Sturmer, Phys. Rev. **184**, 490 (1969).
- [55] H. R. Band *et al.*, Nucl. Instr. Meth. **A400**, 24 (1997).
- [56] G. Mitchell, E154 Technical Note 39, 1996 (unpublished).
- [57] D. G. Crabb, D. B. Day, Nucl. Instr. Meth. **A356**, 9 (1995).
- [58] D. G. Crabb, W. Meyer, Ann. Rev. Nucl. Part. Sci. **47**, 67 (1997).

- [59] S. Bültmann *et al.*, Nucl. Instr. Meth. **A425**, 23 (1999).
- [60] T. Averett, Ph. D. thesis, University of Virginia, August 1995, pp. 70-74.
- [61] G. Court *et al.*, Nucl. Instr. Meth. **A324**, 433 (1993).
- [62] Yu. Kolomensky, Ph. D. thesis, University of Massachusetts Amherst, February 1997, pp. 130-152.
- [63] P. Bosted, E155 Technical Note 10, October 1996 (unpublished).
- [64] S. Incerti and Y. Terrien, E154 Technical Note 22, 1995 (unpublished).
- [65] H. Borel *et al.*, IEEE Trans. Nucl. Sci. **42**, 529 (1995).
- [66] V. Breton *et al.*, Nucl. Instr. Meth. **A362**, 478 (1995).
- [67] G. T. Bartha *et al.*, Nucl. Instr. Meth. **A275**, 59 (1989).
- [68] P. King, E155 Technical Note 74, February 1999 (unpublished).
- [69] G. G. Petratos, Ph. D. thesis, The American University, 1988 (unpublished).
- [70] J. V. Jelley, *Cerenkov Radiation and its Applications*, Pergamon Press (1997), pp. 1-7.
- [71] J. Groves and J. Olmsted, E155 Technical Note 23, September 1996 (unpublished).
- [72] M. Buenerd, E155 Technical Note 4, March 1996 (unpublished).
- [73] P. Bosted, E155 Technical Note 2, March 1996 (unpublished).

- [74] M. Buenerd, E155 Technical Note 3, March 1996 (unpublished).
- [75] J. A. Dunne, Prethesis Project, The American University, 1994 (unpublished).
- [76] Yu. Kolomensky, Ph. D. thesis, University of Massachusetts Amherst, February 1997, pp. 78-85.
- [77] P. DePietro and A. Romano, E155 Technical Note 16, August 1996 (unpublished).
- [78] P. Bosted, E155 Technical Note 52, March 1998 (unpublished).
- [79] L. Sorrell, E155 Technical Note 56, May 1998 (unpublished).
- [80] P. L. Anthony and Z. M. Szalata, SLAC-PUB-7201 (1996).
- [81] P. Bosted, E155 Technical Note 68, September 1998 (unpublished).
- [82] T. Toole, E155 Technical Note 76, January 1999 (unpublished).
- [83] L. G. Levchuk, Nucl. Instr. Meth. **A345**, 496 (1994).
- [84] A. Feltham, E155 Collaboration Meeting Proceedings, July 1997 (unpublished).
- [85] A. Feltham, E155 Analysis Meeting, September 1997 (unpublished).
- [86] A. Tobias, E155 Technical Note 36, July 1997 (unpublished).
- [87] P. Bosted, E155 Technical Note 58, May 1998 (unpublished).
- [88] P. McKee, E155 Technical Note 65, July 1998 (unpublished).

- [89] P. Bosted, E155 Technical Note 66, August 1998 (unpublished).
- [90] A. Tobias, E155 Technical Note 78, February 1999 (unpublished).
- [91] E139, J. Gomez *et al.*, Phys. Rev. **D49**, 4348 (1994).
- [92] T. Averett, E155 Technical Note 27, 1997 (unpublished).
- [93] O. A. Rondon, E155 Technical Note 70, 1998 (unpublished).
- [94] O. A. Rondon, E155 Collaboration Meeting Proceedings, Feb. 1998 (unpublished).
- [95] P. Bosted, E154 Technical Note 29, 1995 (unpublished).
- [96] C. Y. Prescott *et al.*, Phys. Lett. **B84**, 524 (1979).
- [97] Yu. Kolomensky, Ph. D. thesis, University of Massachusetts Amherst, February 1997, pp. 152-155.
- [98] P. Zyla, E154 Collaboration Meeting Proceedings, May 1996, pp. 57-89 (unpublished); E154 Technical Note, July 1997 (unpublished).
- [99] D. Reyna, Ph. D. thesis, The American University, 1998, pp. 113-122 (unpublished).
- [100] E155, P. L. Anthony *et al.*, SLAC-PUB-8049 (1999).
- [101] S. Incerti and V. Breton, E154 Technical Note 36, June 1996 (unpublished).
- [102] F. Sabatié, E154 Technical Note 45, October 1996 (unpublished).

- [103] P. Bosted, E155 Collaboration Meeting Proceedings, June 1998 (unpublished).
- [104] L. W. Mo and Y. S. Tsai, *Rev. Mod. Phys.* **41**, 205 (1969).
- [105] Y. S. Tsai, *Rev. Mod. Phys.* **46**, 815 (1974).
- [106] T. V. Kukhto and N. M. Shumeiko, *Nucl. Phys.* **B219**, 412 (1983).
- [107] S. Kuhn and F. Wesselmann, E155 Technical Note 59, July 1998 (unpublished).
- [108] S. Wandzura and F. Wilczek, *Phys. Lett.* **B72**, 195 (1977).
- [109] E155, P. L. Anthony *et al.*, SLAC-PUB-7983 (1999).
- [110] G. Mitchell, E155 Technical Note 75, January 1999 (unpublished).
- [111] M. Glück *et al.*, *Phys. Rev.* **D53**, 4775 (1996).
- [112] R. Ball *et al.*, *Phys. Lett.* **B378**, 255 (1996).
- [113] S. J. Brodsky *et al.*, *Nucl. Phys.* **B441**, 197 (1995).